

Focusing on the liquid role in the vapour liquid solid growth mechanism

Présentée le 13 janvier 2021

à la Faculté des sciences et techniques de l'ingénieur
Laboratoire des matériaux semiconducteurs
Programme doctoral en science et génie des matériaux

pour l'obtention du grade de Docteur ès Sciences

par

Lea GHISALBERTI

Acceptée sur proposition du jury

Prof. K. Scrivener, présidente du jury
Prof. A. Fontcuberta i Morral, Prof. W. C. Carter, directeurs de thèse
Prof. F. Glas, rapporteur
Prof. V. Dubrovskii, rapporteur
Prof. F. Stellaci, rapporteur

As atoms travelling on a surface looking for their equilibrium position, humans are driven by the same kinetic force: the search for their right place in the world. For all that matters, avoid traps and just look for the crystal lattice that will help your waves resonate.

— L.G.

To all the people who contributed to make this journey possible. Starting from my parents and sister, who supported and guided with care my choices. Then to my supervisors, who both helped me evolve not only professionally but even more importantly as a conscious person. And to all friends and colleagues who helped not only with their presence and experimental efforts, but also in providing an anchor to the beauty of the real world. Thanks to all of you...

Acknowledgements

The author is incredibly grateful first of all to my supervisor and co-supervisor, who both had enough patience for following me in these years. A special thanks also to my colleagues who provided me the experiments on which I based my modelling: Heidi, Wonjong, Christian, Simon, Mahdi and Lucas. Beyond them, a warm thank also to all the other colleagues who helped and supported me in this attempt to become a scientist. Many thanks also for the fundings received from SNSF, NCCR QSIT, as well as H2020 program.

Lausanne, November 23, 2020

L.G.

Abstract

In this work we dive into key questions regarding the wetting of a nanoscale droplet which provides fundamental understanding of Vapor-Liquid-Solid growth mode of nanowires. This understanding is important to perform reproducible NW fabrication and allow their industrial implementation. Our method relies on the continuous interplay between experimental efforts and theoretical modeling in order to combine computational prediction power with reality. In particular the main aspects analysed are the stability of the catalyst-NW system and the dynamics of nucleation at the nanoscale. These phenomena are of fundamental importance not only for the synthesis of nanostructures but also in other areas such as colloidal chemistry and bioengineering. We proceed by focusing on three main aspects of NW preparation: first stages of NW's growth, catalyst-NW system stability and nucleation dynamics. At first we focus on the preparation of arrays of semiconductor nanowires with the target to optimize the vertical yield thanks to the engineering of the wetting behavior of the catalytic droplets at the initial stages of growth. Secondly we investigate the wetting behavior of droplets constrained on top of nanowires and/or cylindrical pillars. In such conditions, droplet volume and constraint geometry are the key factors for determining the most stable configuration of the droplet and thus the direction of further steps of growth. In the last chapters, we analyze more exotic nanowires and thus the wetting behavior of droplets is observed on new geometrical constraints. Beyond droplet's morphological investigation, we consider the consequences of the presence of the liquid phase on the nucleation dynamics, in particular at the triple-phase line, under the assumption of crystal anisotropy of the nucleating phase and the presence of stretching capillary forces.

Key words: nanowires, VLS, modelling, wetting, nucleation, III-V semiconductor, II-V semiconductor

Riassunto

In questo lavoro ci immergiamo nelle domande chiave riguardanti il fenomeno del bagnamento di una nano-goccia, che ci aiuta nella comprensione della modalità di crescita VLS (vapore-liquido-solido) dei nanofili. Questa analisi è importante per assicurare riproducibilità sperimentale e per consentire l'implementazione di nanostrutture in campo industriale. Tratteremo questa tematica sulla base della continua interazione tra sforzi sperimentali e modelli teorici al fine di combinare il potere di previsione computazionale con la realtà. Procederemo concentrandoci su tre aspetti principali della preparazione dei nanofili: i primi stadi di crescita cristallina, la stabilità del sistema catalizzatore-nanofilo e le dinamiche di nucleazione. In un primo momento ci concentriamo sulla preparazione di reticolati di nanofili con l'obiettivo di ottimizzare la loro crescita verticale grazie all'ingegnerizzazione del comportamento del catalizzatore nelle fasi iniziali di crescita. In secondo luogo si studia il comportamento del catalizzatore vincolato al di sopra dei nanofili e / o a pilastri. In tali condizioni, il volume del catalizzatore e la geometria del vincolo geometrico sono i fattori chiave per determinare la configurazione più stabile del catalizzatore e quindi definire la direzione delle successive fasi di crescita. Negli ultimi capitoli, analizzeremo dei nanofili dalla forma più esotica, cercando di chiarire il comportamento del catalizzatore in un sistema più complesso. Al di là dell'indagine morfologica del catalizzatore andremo a considerare le conseguenze della presenza della fase liquida sulla dinamica di nucleazione. In particolare ci interessa cosa succede alla linea di equilibrio fra le 3 fasi del sistema, nel caso in cui si consideri anisotropia cristallina della fase nucleante e la presenza di forze capillari deformanti. Questi fenomeni sono di fondamentale importanza non solo per la sintesi di nanostrutture ma anche in altri settori come la chimica colloidale e la bioingegneria.

Parole Chiave: nanofili, VLS, bagnamento, nucleazione, semiconduttori III-V, semiconduttori II-V

Contents

Acknowledgements	i
Abstract (English/Français/Deutsch)	iii
List of figures	ix
List of tables	1
1 Introduction	1
1.1 Nanotechnology and Epitaxial Growth	1
1.2 What are Nanowires good for?	3
1.3 Vapor Liquid Solid growth mode	6
1.4 About Wetting Phenomena: from theory to nanowires	9
1.5 Outline	11
2 Methodology	13
2.1 The theory on Surface Evolver	14
2.2 Practicalities of Surface Evolver	16
3 Liquid Assisted Selective Area Epitaxy	19
3.1 State of the Art	19
3.2 Wetting behaviour into cylindrical cavities	20
3.3 Computational results wetting into cavities	22
3.4 Initial stages of NW's growth	24
3.5 Arsenic diffusion and shadowing effect	25
3.6 Smoothing the sidewalls	26
4 Liquid stability on top of cylindrical pillars for growth direction control	31
4.1 Droplet stability on top of single-material-pillars	31
4.2 The configuration of the droplet in a situation out of equilibrium	42
4.3 Liquid stability on top of multi-material pillars	43
4.4 Asymmetry in the droplet's wetting	51
	vii

5	Wetting on top of non-cylindrical columns	55
5.1	Geometric influence on the droplet wetting stability and apparent angle dispersion	56
5.2	The role of liquid surface energy in the growth of NWs with a varying cross-section: the case of zig zag NWs	60
6	Nucleation in the vapor-liquid-solid growth mode modeled with Surface Evolver	71
6.1	System definition and computation of the free energy values	72
6.2	Modelling nucleation with Surface Evolver	74
6.3	Energy barrier dependency on the liquid wetting angle	77
7	Conclusions and Outlooks	81
	Bibliography	95

List of Figures

2.1	On the top we show a part of the datafile associated to the mound problem, most precisely the section where the elements of the initial mesh for the simulations are provided. On the bottom, the relative visualization of the vertices and edges as defined in the datafile.[Surface Evolver Manual]	18
3.1	Representation of the 5 main regimes of the droplet initial configuration in the round well.	21
3.2	Sketch of the development of the liquid shape at the edge of the cylindrical cavity as a function of the droplet volume	22
3.3	Computation of the droplet's normalized surface energy as a function of the droplet's volume for different configurations inside a cylindrical cavity. The normalization of the surface energy involves both the droplet's volume and the difference in interfacial energy between the solid-liquid and the solid-vapor system. The droplet's volume is normalized by the cavity's volume On the right side we show the images of the configuration considered.[112]	22
3.4	Comparison between NW's growth obtained after short (left) and long (right) time of Gallium pre-deposition. We deduce from our previous results that the initial configurations of the droplet are the edge and the complete one respectively.[112]	23
3.5	AFM images of the initial stages of growth of GaAs crystals, obtained after 2 minutes nanowire's growth. The two samples differ for the cavity's diameter, which is respectively 45nm (a) and 90nm (b). The scale bar are 100nm and 200nm.[112]	24
3.6	(a) Sketch of the droplet configuration in the cavity with the directionality of As fluxes characterizing the MBE system. Computed 3D plot of the As concentration profile and its cut through the droplet center for cavities with aspect ratio (d/h) 2 (b) and 6 (c) [112]	26
3.7	Sketches of the asymmetrically filling droplet configuration inside a cylindrical cavity and corresponded sliced contour plot of the calculated Arsenic concentration profile for different aspect ratio: a) d/h=2, b) d/h=4, c) d/h=6.[112]	27

3.8	(a) Color-coded AFM images of a single nanohole, top view on the left and 70°-tilted view on the right. Scale bar 100 nm. b) Cross section view of the 3D-Gaussian representing the hole geometry. The interface between Si and SiO ₂ is placed at $z = -0.66$ [113]	28
3.9	Variation of the apparent angle of sessile droplets confined in a Gaussian-shape two-material hole morphology as a function of the volume of the droplet. The normalization V_0 is arbitrary. Values are obtained from the shapes evolved by the software Surface Evolver. [113]	29
4.1	a) Sketch of the droplet's edge configuration on top of an ideal cylinder b) Calculated mean curvature of the facets (white dots) composing the mesh of the droplet represented in inset a) as a function of their position along the x-axes. .	42
4.2	Computed surface energies of the system as a function of the droplet volume for droplet's configuration on the side and on the top. The energy value are normalized by the droplet volume and the difference in the interfacial energies. The characteristic wetting angle for the droplet on the side is 116° (wetting Ga-SiO ₂) while on the top it is 51° (wetting Ga-Si) The radius of the core is 0.5, covered by a 0.1 thickness layer of oxide.	44
4.3	(a) Sketches of the pillars analysed and the resulting equilibrium shape of the sessile droplet on top, taken with the same volume of 0.7 in all insets (b) Surface Evolver simulations on the variation of droplet's apparent angle as a function of the droplet's volume. The pillar system is built as a double cylinder characterized by 2 parameters: inner radius and external radius, defining the Silicon core and the external lateral SiO ₂ coverage respectively. The difference in materials between the 2 regions is computed by using different wetting angles: 51° and 116° for wetting on Si and SiO ₂ respectively. Note how the modification of the internal radius, while maintaining fixed the external radius, causes a modification in the rate with which the apparent angle modifies with the droplet's volume. The fixed external radius ensure that the "Second Pinning" threshold and development remains the same in all cases analyzed.	45
4.4	(a) Sketches of the pillars analysed and the resulting equilibrium shape of the sessile droplet on top, taken with the same volume of 5 in all insets (b) Surface Evolver simulations on the variation of droplet's apperent angle as a function of the droplet's volume. The pillar system is built as a double cylinder characterized by 2 parameters: inner radius and external radius, defining the Silicon core and the external lateral SiO ₂ coverage respectively. The difference in materials between the 2 regions is computed by using different wetting angles: 51° and 116° for wetting on Si and SiO ₂ respectively. Note how the modification of the external radius, while maintaining fixed the inner radius, causes a shifting in the «second pinning» volume threshold.	47

4.5	(a) Sketches of the pillars analysed and the resulting equilibrium shape of the sessile droplet on top, taken with the same volume in all insets (b) Surface Evolver simulations on the variation of droplet's apperent angle as a function of the droplet's volume. The pillar system is built as a double cylinder characterized by 2 parameters: inner radius and external radius, defining the Silicon core and the external lateral SiO ₂ coverage respectively. The difference in materials between the 2 regions is computed by using different wetting angles: 51° and 116° for wetting on Si and SiO ₂ respectively. Note how the modification of the internal radius, casue he modification in the rate with which the apparent angle modifies with the droplet's volume. Modifying the outer radius as well, by keeping the ratio between the two equal to 0.8, causes the shifting in the «second pinning» volume threshold and a modification in the slope as well.	49
4.6	Summary of the main regimes and configurations analyzed in this section . . .	49
4.7	(a) Table showing the relation between Si pillars' diameter and the Ga droplets' contact angle, along with SEM images representing certain diameters. (b, c, and d) SEM pictures of GaAs nanospades on Si pillars and their growth range in the table. (e) Relation between the yield of nanospades (NSPDs) and pillar diameter for a 20 nm (nominal) oxide mask. Copyrighth from ACS[114], further permissions related to the material excerpted should be directed to the ACS.	50
4.8	SEM images of Gallium droplets wetting the top facet of Silicon cylindrical pillars having oxidized sidewalls.	51
4.9	Surface Evolver computation of the (a) variation of the system surface energy as a function of the droplet's volume normalized by the surface area of the pillar and the difference between the surface tension of the liquid-solid and solid-vapor interface. (b) Computation of the apparent angle of the droplets wetting the oxidized pillars symmetrically and asymmetrically. For the asymmetric configuration we report the mean apparent angle.	53
5.1	Computed development of the normalized surface energy of the system composed by a sessile droplet wetting planes characterized by 4 different geometries: triangular, squared, hexagonal and circular (as depicted in the insets)	56
5.2	Sketches of the systems analysed, apparent angle dependency along the perimeter of the droplet for 3 referential volumes (small, medium and large) and top view of the computed equilibrium morphology for different symmetry of the spatial confinement: circular (a), hexagonal (b), squared (c) and triangular (d).	58
5.3	Computation of the dispersion in the apparent angle of the droplet for wetting happening on the 3 low symmetry spatial confinement considered: hexagonal, squared and triangular. 3 referential volumes have been considered in order to take note of the pinning effect.	60
6.1	Phase diagram (a) and the free energy curves (b) computed through Calphad of the system analyzed.	73

6.2	Sketches of the 3 configurations in which the nucleation of the new solid phase can take place.	74
6.3	Computation of the nucleation curves for the GaAs phase transtion through VLS growth mode with the liquid wetting angle 51° and nucleus wetting angle 60° as a function of the radius of the nucleus for the 3 location considered: floating in the droplet, heteronucleation far away from the TPL and heteronucleation at the TPL.	75
6.4	Equilibrium shape of the nucleating phase taking place at the TPL for wetting angle equal to 51° : (a) top view and (b) side-view	76
6.5	Surface Evolver morphologies minimizing the surface energy of the systems composed by substrate, nucleus, liquid and vapor for nucleus wetting angle of 60° and liquid wetting angle respectively of (a) 30° , (b) 51° , (c) 70° , (d) 90° , (e) 100° and (f) 110°	77
6.6	Computation of the nucleation curves for the GaAs phase transtion through VLS growth mode at the TPL with nucleus wetting angle 60° and liquid wetting angle of (a) 30° , (b) 51° , (c) 70° , (d) 90° , (e) 100° and (f) 110°	78
6.7	Comparison between data points representing the development of the TPL energy barrier (measured from the curves shown in ig. 6.5, as a function of the wetting angle and the fitting equation reported in eq.(5.6)	79

1 Introduction

In our modern society, the desire for novelty and improvement governs the main direction taken by research and technological development. Due to the astonishing transformations that happened in western countries thanks to the introduction of microelectronics into everyday life, now, major care and fundings are spent into feeding the continuous hunger for new and better devices, having more efficiency, more power, less cost and occupying less space. In particular, thanks to the reduced size, materials can present characteristics completely different from the ones that would correspond to the bulk system of the same material. This phenomenon is linked mostly to the higher relevance that the surface plays in a confined system and to quantum confinement. This research project is part of a larger context where the goal is to bring further this miniaturization tendency by understanding in depth the key parameters controlling the synthesis of these crystal nanostructures, specifically semiconductor nanowires, to contribute obtaining gadgets with new and/or better performances. Our approach focused mostly on getting a deeper and more fundamental understanding of the physical processes. Through collaborations with experimental colleagues, we were provided samples and direct measurements, necessary data for getting reliable and new insight into the growth dynamics at the nanoscale.

1.1 Nanotechnology and Epitaxial Growth

First, I would like to introduce the concept of nanotechnology. There is often a sort of mysticism lifting in the tonality and in the eyes of a rather non-scientific audience. Technology is the art of modifying nature by taking advantage of specific scientific knowledge. This modification of nature can happen at incredibly different scales. With the prefix *nano* we identify the molecular level, the dimension at which atoms can arrange and interact with each other, creating the fundamental structures composing any material and micro-organism. The advent of nanotechnology started with the manipulation of atoms with Scanning Tunneling Microscopy (STM), achievement awarded also with the Nobel Prize in 1986. Thanks to the opportunity to reach such invisible domains, the discovery of completely new properties and states of matter became possible.[1, 2]

The main idea of nanotechnology was born thanks to the visionary physicist Richard Feynman, which opened the eyes of humanity on the truth about our world with the famous citation "There is Plenty of Room at the Bottom". Later, thanks to the STM the necessary means to visualize and manipulate for the first time atoms became available.[1, 2, 3] The opportunity to observe nature at its most fundamental level helped the scientific world not only to offer a new view of reality but most importantly it showed the existence of a new field of production and manufacturing. This became concretely promising thanks to the development of high-resolution fabrication techniques, that enabled to control far to nanoscale precision the geometry, the composition, and the structure of electronic devices.[4, 5, 6] One famous achievement, which increased the political and commercial attention to this sector, is the realization of the first MOSFET with a 10nm gate oxide thickness by IBM in 1987.[7] From that moment on the academy, industry and even governments devoted funding to investigate the wide range of functional opportunities contained at the nanoscale level.[8] While nanotechnology mostly gained his fame and interest thanks to the evident application in electronics, the number of fields that got influenced by its fundamentally new approach are enormous. Beyond its implementation in display technology and lighting,[9, 10] particularly interesting is what happened in energy harvesting where nanomaterials gave new hope for creating devices having higher efficiency than the traditional ones.[11, 12, 13] In medical applications, the use of nanoscale materials, such as biocompatible nanoparticles and functionalized molecular crystal, allowed the introduction of innovative drug delivery systems, tissue engineering, and even biosensors which all boosted our ability to prevent, diagnose and treat illnesses in living organism.[14, 15, 16] Due to the incredible impact provided by nanotechnology in so many different fields, speculations are spreading on even more spectacular implementation into molecular control, nanorobotics, programmable matter, and productive nanosystem.[17, 18, 19]

The current research in the field of nanotechnology mostly implements two specific approaches for the production of devices and new materials: these two methods are identified with the idiomatic expressions of "top-down" and "bottom-up". Behind these definitions, there is the way in which the relationship and modification of nature take place. The top-down approach represents a mostly destructive way of altering the bulk material into a reduced and functionalized version of the initial setup. It usually takes advantage of etching processes. The major achievements in the microelectronics industry have been obtained mostly following this approach;[20, 21, 22] this consequently helped the development of always more refined way of processing and cutting down materials reaching a nanometric resolution, helping the further establishment of the technique. Nevertheless, beyond its prevalence and reliability, it is important to remember the drawbacks as well, that often involve a roughening of the remaining surface and a consequent worsening of the stability and performance of the device. Interfaces and surfaces play a key role in determining the quality of functional properties: the high probability to form trap states and defects makes the top approach not particularly reliable for further scaling down.

The "bottom-up" approach is founded on the principle of creating the material starting from

its building blocks, that is to say from the precursor atoms necessary for obtaining the desired final material. What is mostly beautiful about this method is that, within the environment allowed for this reaction to take place, the selected precursors can rearrange themselves spontaneously.[23, 24, 25] In this way, thanks to the self-arrangement of the atoms, the obtained materials, and devices may show better stability and in general interfaces present fewer damages. The main side effect of the bottom-up approach is the limited range of growth conditions available in the different experimental setups. Indeed different materials, as well as different phases of the same material, request a specific combination of pressure, temperature, and material supply to maintain their arrangements. According to the predictions of thermodynamics, the system will always tend towards the state holding the lowest value of total energy, associated to a specific combination of different phases. Just these phases can be considered as the preferential ones. In order to increase the number of obtainable materials and phases, the epitaxy growth equipment market developed a wide range of different and increasingly refined production chambers, creating a market that nowadays is worth around US\$990 million.[26, 27]

A solution for increasing the degrees of freedom in the preparation of materials at the nanoscale involved the synergistic combination of bottom-up and top-down techniques applied to epitaxial growth.[28, 29, 30] In agreement with the bottom-up approach, the deposition of the precursor materials is performed on the selected reactive surface, the substrate, followed by the self-rearrangement of the atoms into the configuration that mostly suit the growth environment. Even if such an approach was born initially as surface coating technology, by adding the contribution of the top-down method, it was possible to spread this same technique to 2D, 1D and 0D materials as well, for the preparation of nanowells, nanowires and quantum dots. The shift between different structures is managed through the substrate preparation, where the removal and/or the deposition of different materials-mask with certain patterns, enable the formation of preferential locations where the deposition and the following reactions are confined to take place. This method is referred to as selective area epitaxy.[31, 32, 33]

1.2 What are Nanowires good for?

A nanowire is a crystal that mostly develops along one preferential dimension thus presenting a constrained lateral size. The term nano implies that the constraining in the diameter stays within the range of hundreds of nanometer while the longitudinal length can develop almost without limit. It is important to note that nanowires are intrinsically very different from likewise famous nanotubes. These latter are nano-size cylinders of atoms, well described by the idea of a rolled atomic layer. Nanowires, on the other end, are filled with a specific crystallographic rearrangement of the atoms.[34, 35] In general, without considering the composing material yet, it is important to notice that nanowire's unique geometry already represents an advantage with respect to traditional bulk systems. The high surface to volume ratio, ensured by the long filamentary geometry, allows the combination of crystalline materials with a large reactive available surface area. Indeed the first obvious implementation

of such nanostructures was connected with the functionalization of their lateral surface.[36] This is particularly relevant for sensing applications where a larger reactive area means higher resolution in the detection process. Many different applications took advantage of this new level of functionalization of the surface for chemical sensing, in particular medicine, and more in general biology.[37, 38] The possibility to coat the nanowire with antibody's binding specific proteins allows not only to create selective traps but also to create real-time detectors, taking advantage of the change in the nanowire's electrical conductance due to the modification of its surface termination. Another important contribution that the geometry plays in making these nanostructures so interesting can be appreciated by analyzing the light absorption properties of standing nanowires.[39] The implementation of single nanowire into solar cell devices showed an unexpected larger absorption cross-section compared to bulk solar cells. Further analysis allowed to clarify that single nanowires have absorption cross-section that is more than 50 times the geometrical cross-section. The main reason behind this incredible result is the fact that there is a strong long-range disruption of the light path along the nanowire which makes the effective absorbing NW's surface much larger than the one expected.[40, 41, 42, 43] Another important field in which nanowires represent ideal platforms is the memory and data storage industry.[44] The possibility to tailor phase-changing materials into nanostructured form appeared to be the solution to the search for universal memory storage already a decade ago. Phase-change materials are materials that can be reversibly switched between amorphous and crystalline states, providing a natural 2-states system for binary encoding of information. A material frequently analyzed for non-volatile memory applications is $\text{Ge}_2\text{Sb}_2\text{Te}_5$. The main issue with such materials is that traditional top-down processing towards re-scaling tend to damage their properties and hindered the nanostructurization. Luckily the development of self-assembly based preparation technique enables the design and preparation of sub-lithographic sized nanostructures with unique geometries as well.[45]

The most promising application field and, at the same time the most remunerative one, is the field of electronics. Over the past two decades, nanowires proved to be among the best type of nanoscale building blocks for the bottom-up assembly of functional electronic and optoelectronic devices. In nanocircuits, nanowires can play a key role both as device elements and as interconnections between different elements. The main factor that makes them so versatile is in the development achieved in their preparation which allows high-quality synthetic nanowires to be obtained through the bottom-up approach. [46, 47, 48] Particularly relevant are semiconductor nanowires (e.g., group IV, III–V, and II–VI semiconductors and their alloys) which proved their excellent electronic properties with respect to the bulk-single crystal material, such as improved carrier mobility in n-type Si, p-type GaAs, InSb and InAs/InP core-shell nanowires.[49, 50, 51, 52] Beyond the properties of the single nanowire, another important aspect in electronics is the possibility to obtain high-quality nanowire directly assembled into arrays. In this way, both the synthesis of the NW and their arrangement into arrays are performed simultaneously and efficiently. The combination of tunable properties in the building-blocks and their design into predefined architectures ensure the development of highly performing devices such as field-effect transistors (FETs), memory,

and integrated nanowire logic gates; also in nanophotonics, this allowed the production of nanoscale light-emitting diodes, lasers, waveguides, and photovoltaics.[53] Nanowires are nowadays considered among the most promising elements composing "more than Moore's devices".[54] In semiconductor technology, the expectations of the market for a continuous down-scaling in the size of integrated circuits without reducing their performance, classically hit a solid wall once quantum phenomena, such as the tunneling effect, started to appear due to the reduced size. Silicon was the absolute protagonist of the development of the major IC technology until the scaling down of the traditional planar geometry reached its maximum-minimum at the transistor dimension of 10nm.[55] Beyond this level, the adoption of new geometrical design and new materials clearly appeared to be the solution to maintain the market of production open and productive. The best example of nanowire's implementation is the development of the "gate-all-around-transistors" where arrays of nanowires are embedded into a thin layer of conductive material, whose thickness represents the gate-size. Thanks to this new architecture, sub-15nm gate-all-around field-effect transistors on silicon nanowires have been obtained and are expected to be a good candidate for even further scaling down.[56] Going further in the scaling down process, once dimensions reach the quantum limits, it is not enough anymore to play with new geometries and architectures but it is necessary to change "bulk material" as a starting point. While for Si, the appearance of quantum phenomena starts at 7 nm size, there are semiconductor materials that show still classical behavior also below 5 nm size, such as molybdenum disulfide and carbon nanotubes. Already in 2016 a transistor with a 1-nm physical gate was prepared using MoS₂, showing quantum confinement around 500 nm size, and a single-walled carbon nanotube gate electrode. [57, 58]

The discovery of quantum confinement expanded the tunability of both electronic and optical properties of metals and semiconductor materials. By playing with the size and the shape of nanoparticles is possible to modify their band-gap and, specifically, the energy levels distribution. The threshold size for the onset of quantum confinement corresponds to the size of the wavelength associated to the electrons taking part to the process, also called the Fermi wavelength. The type of atoms and their arrangement determine the value of the Fermi wavelength. For metals, it is below 1nm while for semiconductor materials it can be of several tens of nanometers. The newest trends in microelectronics are combining traditional platforms and quantum phenomena to expand the range of application and performance.[59] Concerning unconventional electronics, quantum computing is becoming more concrete. IBM is already giving free access to their quantum computers for testing simulations and for verifying the calculating power of their devices. In quantum computers, the basic building block is a quantum bit or qubit. The information stored in this unit can take different forms such as charge, photon, spin, or polarization. Among the different systems analyzed, semiconducting nanowires recently demonstrated to be a promising solid-state platform for quantum computing. Qubits created in nanowires could yield very fast and topologically protected electrical spin manipulation, allowing them to have fast logic gate operation. Spin qubits in particular need an environment where coherent single spin rotations can happen and where the controllable two-spin coupling is available. Another important parameter is

the coherence time, which is to say the timescale at which spin orientation is lost because of perturbation from the environment. This coherence time must be many times larger than the logic-gate operational time, but perturbations from the environment are often difficult to avoid. The real prominence of nanowires in quantum computing derives indeed from the possibility to overcome the challenge represented by decoherence by taking advantage of topology. Topological qubits can be prepared non-locally in such a way that the quantum state is delocalized between 2 different points in the world. This delocalization ensures immunity to local perturbation. The possibility to build topological qubits became real once the first signatures of Majorana fermion quasi-particles were observed in nanowire-based-devices. The experimental setup is quite straightforward: a 1D electronic system with spin-orbit interaction and superconductivity in a magnetic field. The most successful devices built until now are InSb nanowires contacted by electrodes, a superconducting NbTiN, and a Ti/Au contact for detection. Also from a point of view of scalability, nanowires represent promising platforms allowing for multiple local contacts and electrostatic gates to be applied on top, beneath, around, and next to the wire. These achievements, again, were made possible mostly thanks to the incredible advancements in the preparation techniques available ensuring a huge degree of freedom in composition, stacking, and geometry.[60, 61, 62]

1.3 Vapor Liquid Solid growth mode

The quality and performance of nanoscale devices are intrinsically connected with the preparation procedure with which their main building blocks are produced. Here we will focus on the Vapor-Liquid-Solid (VLS) growth mode.[63, 64, 65] The VLS approach is part of the above-mentioned "bottom-up" growth technique even if it can easily be translated into a mixed technique by coupling it with top-down preparation of the substrate. The name VLS describes the phases taking part in the process of crystal growth. Even if the growing crystal is the solid (S) part, the protagonist role of this phase transition is played by the liquid phase (L) which behaves as a bridge between the crystal and its precursors dispersed in the vapor phase (V). This bridging liquid phase is often referred to as the catalyst of the reaction. An effective catalyst for a transformation mostly requires to remain inert while offering a preferential environment where the reactants can be collected and let react. From a practical point of view, this catalytic effect is traditionally well performed by liquid metallic nanoparticles.[66, 67] According to the growth conditions in the reaction chamber and the size as well, the metallic nanoparticle may appear in the solid form while continuing to play its role as a catalyst. In this case, the growth mode comes under the name of (VSS) where indeed the bridging phase is solid.

With respect to traditional bulk epitaxial technologies, happening directly from vapor phase to solid phase, the catalyst-assisted regime is faster and spatially localized thanks to the intermediating role played by the nanoparticle. Let's consider for example a liquid catalyst and let's analyze its role as an intermediary in the epitaxial process. At the liquid-vapor interface, both evaporation and condensation processes take place constantly and simultaneously, it

is thus possible to define a certain steady equilibrium between the two processes.[68, 69, 70, 71] At the solid-liquid interface, there is another dynamic equilibrium between two further competing processes: the crystallization and the dissolution of the solid. The two dynamic equilibria will compete for the material inside the droplet as well, thus creating a further equilibrium defining the overall process of growth. A practical example of perfect balance in the total dynamic equilibrium among all the processes involved can be observed when a nanowire maintains constant diameter along all its length under constant materials supply. Since the size of the nanowire is linked to the catalytic nanoparticle, a nanowire with the same radius along its length can be associated with a fixed droplet volume during the entire synthesis.[72, 73] The condition of constant liquid volume is reached with the incoming flux of materials in the liquid (through vapor condensation and solid dissolution) equalizing the outgoing flux (though crystal growth and liquid evaporation). In the opposite case, when the two fluxes are not equal, is possible to appreciate the so-called "tapering effect" in which the nanowire's shape is characterized by a change in radius during the growth, resulting in a pointy structure and often ending with the total consumption of the liquid. It is quite clear now how much the nanowire's growth is controlled by the characteristic of the liquid, in particular by the number of crystal precursors composing it. More precisely the composition of the droplet plays a key role in determining the growth rate and the crystal phase since it affects the equilibrium between the vapor and the liquid phase (where the precursors are first dispersed) and the equilibrium between the liquid and the solid phase.[74, 75, 76, 77]

From the perspective of classical thermodynamics, it is possible to describe crystal growth, the combination of all the aforementioned processes, by considering the energy associated with the different phases of the system. The main rule is that the transformation takes place just if there is a gain in energy for the system considered as a whole. Let's consider the nucleation of a crystal from a liquid phase: the process will ensure gain in energy thanks to the better organization of the atoms into a solid-crystal structure but at the same time will cause a loss in energy due to the formation of a boundary, a lost in the unity of the system, practically represented by the interface between the old and the new phase. According to thermodynamics, it is possible to predict if a transformation can increase the stability of the system by comparing the total energy of the initial state and the total energy of the final state. The two contributions to the total energy of a system are called respectively the "volumetric energy" and the "surface energy". The main parameter to calculate the volumetric contribution to the total energy for each phase i is the chemical potential μ_i , which defines the variation of the Gibbs free energy of the system (G) at any variation of the amount of the i -phase moles (n_i), as expressed in eq. (1.1)

$$\mu_i = \frac{\delta(G)}{\delta(n)_i} \quad (1.1)$$

Considering a phase transition from an initial phase *initial* to a final phase *final* happening at

a certain temperature and pressure, we can define the formation energy as the difference in the chemical potentials of the two phases involved in the process, as described by eq. (1.2).

$$E_{\text{form}} = (\mu_{\text{final}} - \mu_{\text{initial}}) \quad (1.2)$$

The variation in the volumetric energy of the system caused by the phase transition can be given by the product between the formation energy and the volume of matter that undertook the transformation. Regarding the surface energy contribution, the main parameter to be remembered is the interfacial energy, traditionally considered as the energy loss linked to the absence of further atoms belonging to the same phase. Under this assumption, the surface contribution to the total energy of the system (E_{surf}) can be easily calculated by adding all the interfacial energies of the system (γ_i) multiplied for the area of the interfaces they are related to (A_i) as described in eq (1.3).

$$E_{\text{surf}} = \sum_{i=1}^N \gamma_i * A_i \quad (1.3)$$

Even if this analytical approach proved to be reliable in the prediction of macroscopic phase transformations, once arrived at the nanoscale some inconsistencies may start to appear.[78, 79] One major problem of classical nucleation theory is the approximation of the system with an idealized version of the system itself. Crystals are assumed to be composed by perfectly distributed atoms while interfaces are considered mostly from a 2D perspective. At the nanoscale, the real nature of the system needs to be considered, defects included. In particular every interface is a new phase in itself, a confined region of atoms having a unique arrangement, intermediate and gradually shifting from one phase to the other. From this perspective, it is clear that in order to properly study the underlying mechanisms taking part in any phase transition, a blind implementation of classical theory can be often unreliable if not misleading.

Also in the realm of nanowire growth, in particular through VLS approach, the majority of models describing the dynamics of phase transition still adopt the same classical macroscopic point of view. In particular, the contribution of the liquid phase is often extremely simplified by considering just its effect on the overall stability of the system. In this case, the main parameters taken into account are, as before, mostly the macroscopic ones, such as volume, shape, composition, and wetting angle. Beyond this first degree of approximation, another imprecision is related to the application of the Young's relation, reported in eq (1.4), to the case of droplet confined on the top of a NW. The Young's relation can relate the shape of a droplet with the interfacial energies of the system just in the case of unconstrained wetting, that is to say when the substrate is infinite or large enough to not cause interference with the

spontaneous wetting behaviour of the droplet.

$$\gamma_{SV} = \gamma_{SL} + \gamma_{LV} \cos(\theta) \quad (1.4)$$

As it often happens during the VLS growth mode, the size of the droplet and the size of the solid underneath are comparable and may create the so-called "pinning" effect.[80] This effect provokes a deviation from the expected equilibrium shape of the liquid due to an external geometrical constraint. Because of the constraining, the first thing that changes is the angle characterizing the spherical cap associated with the shape of the liquid. This angle, modified by the constraint is not really a contact angle, like the one in eq (1.4), but an apparent wetting angle. The correlation between wetting angle and interfacial energies described in (1.4) cannot be applied in the case of constrained droplets, and thus can not be applied to the majority of the systems describing VLS growth mode. More details regarding the wetting behavior of sessile droplets under different geometrical constraints will be presented in the next chapters.

Beyond the open questions still surrounding the VLS growth mode, it is clear that there is a strong connection between the characteristics of the liquid droplets and the consequent characteristics of the growing nanowire. In particular, it has been shown that the droplet contact angle with the solid NW determines the crystal phase, growth direction, orientation, and polarity of the NW itself. In this thesis work, we will focus on clarifying even more the catalyst's wetting behavior and its role in defining crystal growth.[67, 81, 82, 83, 84, 85, 86, 87, 88, 89, 90]

1.4 About Wetting Phenomena: from theory to nanowires

Since the main topic of this research project is the phenomenon of wetting, we focus now on the fundamental concepts and terminologies of wetting. The degree by which a liquid wets a solid depends on the atomistic structure of the bulk phases involved and on the characteristics of the interface itself. The term interface identifies the separation between two different phases. From an atomistic point of view it is associated with a non-uniform region, whose composition ranges between the composition of the two phases in contact. To simplify the modelling, the interface is usually replaced by a mathematical plane, holding properties related to the specific system. The interfacial energy, or surface energy in case of solid-vapor system, is the most used parameter. When dealing with just isotropic interfacial energies, the Young-equation (1.4) is a good solution describing the condition of equilibrium for the contact among 3 phases, usually solid, liquid and vapor.

The VLS growth mode of nanowires represent a particular case of stationary equilibrium among different phases, apparently as many as the one associated with the traditional image of the Young equation. Even though the initial conditions of VLS growth involve 3 phases

(i.e. vapor, liquid and solid), the growing system is indeed composed by 4 phases, where the growing crystal building up the future nanowire should be considered as an additional solid phase. Nevertheless, a "growing" system is, by definition, far away from equilibrium. In the past some attempts to describe and model this stationary regime have been proposed but they often rely on the application of the Young equation for interconnecting wetting angle and surface energetic. [91] The main assumption for applying the Young equation is the presence of an underformable substrate in equilibrium with an unconstrained liquid phase and the vapor. A growing nanowire though, is not only out of thermodynamic equilibrium, but it is also constraining the liquid on top of it due to the reduced size of its diameter.

The complexities of the VLS growth mode have been better depicted thanks to three-dimensional molecular dynamics (MD) simulations which helped visualizing from an atomistic point of view the consequences of liquid-solid interaction during high temperature nanowire's growth. [92] For droplet's wetting the top of hexagonal cross-sectioned NW, one of the main result is already the faceted nature of the solid-liquid interface. This interface features four 111 faceted orientations separated by interfaces that appear atomically rough in nature. The contact line (TPL) dips below one facet, and climbs above the neighboring facet, following the orientation of the external facets composing the tip of the wire. The effect is associated with the anisotropy of the interfacial energies characterizing the solid crystal system. The role of the wetting angle was also analysed, mostly in its dependency on the liquid volume. In particular, it was proved that as droplet contact angles approach the Young's values with increasing liquid volume, a spontaneous tilting of the droplet to the side of the nanowire was observed. The nature of the tilting process is mostly linked to the enlargement of one of the tilted facets composing the solid-liquid interface. As time progresses, the droplet does not lock into a new equilibrium wetting configuration but rather continues to advance along the nanowire surface. During this process, the shape of the solid-liquid interface evolves as well, becoming more spherical. This behavior is also in contrast with many models maintaining fixed solid shapes as reference for simulating the NW-droplet system.

Due to this dynamical nature of NWs, we should introduce a more microscopic consideration of the wetting equilibrium. For example, in the case of wetting on deformable substrate, where surface energies are isotropic, the condition of equilibrium is described by the Neumann relationship:

$$\frac{\gamma_{LIV}}{\sin\beta} = \frac{\gamma_{LIL2}}{\sin\alpha} = \frac{\gamma_{L2V}}{\sin\phi} \quad (1.5)$$

In eq (1.5), α is the angle between γ_{LIV} and γ_{L2V} , β is the angle between γ_{LIL2} and γ_{L2V} and ϕ is the angle between γ_{LIL2} and γ_{LIV} .

The reliability of the Neumann equation was proved by experimental observation through X-ray microscopy of asymmetric wetting ridges on soft solids. [93] In the last years, one

of the most questionable issues in wetting is the force balance that includes the vertical component of liquid surface tension. When analysing soft solids, it is possible to observe the vertical component leading to a microscopic elongation of the contact line, forming a peak. In particular they were able to link the macroscopic and microscopic contact angles to Young and Neuman laws, respectively. The main message of this result is that by deeper investigation what is valid at the macroscopic scale is often untrue in the microscopic domain.

From a macroscopic point of view, whenever interfaces involve crystalline solids or liquid crystals, the interfacial energies cannot be isotropic and the computation of the equilibrium of the system gets more complicated. For isolated solid for example, the equilibrium shape differs strongly from the one associated to a liquid particle, due to the anisotropy of its surface energy. An effective model for predicting the equilibrium crystal shape (ECS) of isolated solid particle is the Wulff construction which involve the polar plot of the orientation dependence of surface energy, also known as the γ -plot.[94] The ECS is convex and conveniently centered on a point referred to as the Wulff point. This construction can show the formation of facets or curved surfaces, respectively in case of a crystallographic preferential orientation and in case of atomically rough orientations. When a liquid is in contact with a substrate, the implementation of the anisotropy of the interfacial energy of the solid should be addressed in order to properly understand the equilibrium condition of the system.

1.5 Outline

In this thesis work, we will present three main insights gained thanks to the synergy between theory and experiments, between simulations and real data analysis. The software Surface Evolver[95] used for modelling the wetting contribution, is presented in the methodology part. The first main insight concern the preparation of arrays of semiconductor nanowires through VLS and selective area epitaxy and the possibility to optimize the vertical yield thanks to the engineering of the wetting behavior of the catalytic droplets at the initial stages of growth. The same phenomenon is first analyzed for arrays produced from cylindrical cavities obtained through traditional lithographic techniques and secondly for arrays produced without lithography and presenting smooth cavities. The second topic analyzed is the wetting behavior of droplets constrained on top of nanowires and/or cylindrical pillars. In such conditions, droplet volume and constraint geometry are the key factors for determining the most stable configuration of the droplet and thus the direction of further layers of growth. In the following chapter, we will focus on more exotic nanowires and thus the wetting behavior of droplets is observed on new geometrical constraints in order to explain alternating growth mechanism. In the last chapter we will present also some considerations about the nucleation event at the triple-phase line, under the assumption of crystal anisotropy and unbalanced capillary forces.

2 Methodology

Modelling the outcome of an experiment before its actual realization can save time, resources and consequently enhance scientific progress. Computational-based problem solving approaches are diffusing as reliable tools for the design and advance of experimental science. In the field of nanotechnology, computational support becomes even more useful due to the highly specialized and demanding experimental conditions at which the most interesting phenomena take place. Limited size and reduced time-scale characterizing crystal growth are often out of reach and simulations can represent a reliable alternative to *in-vivo* observations. The combination of experimental efforts and computational modelling can ensure the proper development of theories allowing better understanding and control of nanoscale processes. In this project we show how improving the interlinks between experiments and theory is essential to gain in simplicity and thus in consequent understanding of fundamental science. The experiments have been performed by colleagues belonging to the LMSC group in EPFL, who provided a lot of inspiring innovative structures and versatile preparation procedure representing the real starting point of all the modelling and theories provided in this thesis. Regarding the modelling part, both thermodynamic principles and kinetics considerations are interlinked to ensure a wider range of accuracy, mainly regarding the analysis of the initial stages of crystal growth. The main theories developed here, even though based on experimental observation of specific physical systems, are of general nature and thus can be translated to solve wider questions involving phase transitions and stability rules in different fields and applications. In particular, a tool that resulted to be particularly versatile and useful is the software Surface Evolver, which provides a reference frame for the analysis of liquid-solid interaction and its consequences on the equilibrium of the system. Liquid stability is not only key for understanding the VLS growth of NWs but it is relevant also for medical applications and in the development of bioinspired materials. We thus devote the chapter of the methodology for explaining how Surface Evolver works.[95]

2.1 The theory on Surface Evolver

The software Surface Evolver was developed in C code language by Kenneth A. Brakke in the 90s.[95] The main characteristic is in its interactivity which ensures the study of the shape of liquid surfaces under the effects of different energies and constraints. It is possible to implement gravitational energy, surface contact energy and surface energy integrals. Constraints can be defined by the user both locally and globally and they can include linear or superficial boundaries or the arbitrary selection of a fixed volume or pressure. Any given surface is represented as a collection of connected triangles enabling the system to create and adopt arbitrary and complex topologies. The most straightforward use of Surface Evolver is to minimize the energy associated with a certain surface. The total energy is computed starting from the coordinates of the vertices of the triangulation composing the surface using different methodologies: gradient descendent, conjugate gradient or Hessian matrix. The first two are first order methods, providing the calculation of the first derivatives of energy and constrained quantities. Often these methods are slow to converge to the minimum configuration and it may difficult to know whether the system is blocked into a saddle point. The Hessian matrix is thus available to fast this process by providing the second order derivatives of the energies with respect to the vertex coordinates[96] In our analysis we implemented a fixed gap energy, equal to one, to define the curved constraint *convex*, in order to keep the edges from short-cutting curved constraint surfaces. Because of this constraint the investigation of the eigenvalues of the Hessian matrix in order to verify the minimal energy condition is not possible. We thus worked mostly through the gradient descent method.

The gradient descendent method can be represented as an attempt to get down from the top of a mountain by taking the path with the highest steepness. Since the mountain-landscape is not constant, a repetition of the measurement of the local steepness will be necessary to verify the correct direction. In the hypothesis that the measurement of the steepness takes long, the fastest way downwards will imply the selection of the optimal frequency in the measurement. We consider now instead of a mountain-landscape a multivariable function $F(\mathbf{x})$, composed by all the energetical contributions defining the system. In the hypothesis that $F(\mathbf{x})$ is locally differentiable in the point \mathbf{a} , the descendent method predics that $F(\mathbf{x})$ decreases fastest if one goes from \mathbf{a} in the direction of the negative gradient of $F(\mathbf{x})$ calculated in \mathbf{a} , that is to say $-\nabla F(\mathbf{a})$. Considering the successive step n , along the direction of the gradient calculated in the \mathbf{a} , we can summarize the descendent method with the statement that if (2.1) is true,

$$a_{n+1} = a_n - \gamma \nabla F(a_n) \quad (2.1)$$

for γ real and small enough number, then $F(\mathbf{a}_n) \geq F(\mathbf{a}_{n+1})$. The main idea is the movement against the gradient, toward the local minimum. Considering different successive steps and starting from a guess of the minimal position \mathbf{x}_0 of F , it is possible to have a monotonic sequence: $F(\mathbf{x}_0) \geq F(\mathbf{x}_1) \geq F(\mathbf{x}_2) \geq F(\mathbf{x}_n)$. This sequence is predicted to converge into (\mathbf{x}_n) ,

coordinates of the desired local minimum. In our case the use of the global constraint convex for F ensures all local minima are also global minima, so in this case gradient descent can converge to the global solution. By setting a convergence criteria based on the difference in energy between consecutive iterations is possible to set the end of the simulation. We also perform a final switch to the quadratic model, in which edges are represented as quadratic curves and facets as quadratic patches, in order to increase the accuracy. The best guess of the final energy value associated to the equilibrium condition is obtained, after fine refinement of the mesh, thanks to an extrapolation procedure. According to our knowledge the extrapolation gives the best result as long as the ratio between the area of the largest facet and the total area of the surface of the liquid results lower than 10^{-3} . Moreover, a clear sign of being close to the equilibrium solution is the nearly null variation in the total energy after each iteration.

From its release as a free programme, Surface Evolver has been used mostly for solving problems of capillary surfaces.[97, 98] In particular a very interesting application is still the research aimed at optimizing the superhydrophobicity of surfaces. Wetting and spreading of a drop on any heterogeneous surface is related to the pinning of its triple line. The pinning makes the motion discontinuous and thus impossible to be solved analytically. Thanks to Surface Evolver it is possible to analyse the stability of microdroplets configuration and thus enabling the prediction of its stillness as a function of the volume/pressure or geometrical characteristics of the system. In general the majority of defectfull or composite surface can be engineered to modify the wetting dynamics on top of it. Many works mostly address the changes in the shape and energy of a drop as a function of volume and number of circular defects contacted at the solid-liquid interface. As a consequence it is possible to predict, by comparing the effective stability of the different configurations, the respective receding and advancing thresholds.[99, 100, 101] In the field of biology, Surface Evolver is capable of modeling lipid membrane vesicle system accurately. An example is the possibility to model the different vesicle configurations of the non-cylindrically symmetric case, impossible to solve without numerical methods. As a further confirmation, during the iteration and the minimization processes the shapes behaved as they would in the natural world. By identifying the range of stability of such shapes, they computed the elastic constant of the membrane and verify the agreement with theoretical predictions.[102] Also the solidification from liquid metals can be analyzed by using the Surface Evolver. The crystallization generally starts at many nuclei with random orientation and the atoms at the grain boundaries are the one in a higher energy states than the interior atoms. During the annealing, thermal motions can be activated and the boundaries migrate at a rate proportional to their curvature, assuming absence of defects/impurities. Through iteration it is possible to model the dynamics of the evolution and get to the most probable grain distribution.[95] As a final example of Surface Evolver application, we cite the analysis of non-Newtonian flow of liquids and of the plastic flow of solids. The elastic-plastic response of dry soap foams subjected to quasistatic, simple shearing flow is analyzed. In specific they computed the foam structures that minimize total surface area at each value of strain.[103]

The complete Surface Evolver package, including source code, manual, and sample datafiles,

is available for free from geom.umn.edu.

2.2 Practicalities of Surface Evolver

Surface Evolver is a finite element based software and the quality of the mesh is a fundamental aspect for ensuring reliable results. The mesh represents the surface, the external boundary of a certain domain. In this software the main geometric elements involved in forming the mesh are vertices, edges, faces, and bodies. Vertices are associated with points in the 3-dimensional Euclidean space. The edges, connecting pairs of vertices, are characterized by straight line segments. Faces are delimited by 3 edges, creating flat triangles. In order to define a body, it is necessary to list the faces bounding it. The combination of all the elements of the system gives birth to a macroscopic entity, the "surface", on which Evolver operates according to constraints, boundaries, and forces, that is to say the auxiliary data provided to define the dynamic of the system. There are no limitations on how many edges may share a vertex nor on how many faces may share an edge. This freedom allows to represent also the condition of triple junctions of surfaces characteristic of soap film. There are no restrictions on the orientation of neighboring edges and faces: that's why unoriented surfaces can be treated as well. The whole system, represented by the entity "surface" is bound to have a total energy, calculated by summing up the surface tensions associated to the different bodies or even to the different faces and edges. This total energy is the energy which the software Evolver minimizes during each iteration. No particular units of measurement are used. The program only deals with numerical values and to relate the results to the real world, it's just necessary to unify the obtained values within one consistent system. Before starting the simulations, it is necessary to specify the initial conditions of the surface. For doing that, the characteristics of all the necessary elements are listed into a text file (the "datafile"). An example of the layout of the initial mesh is provided in Fig. 2.1, where we show the part of the datafile containing the elements of the mesh on the top and the relative shape given by the combination of all the elements.

The terms VERTICES, EDGES, FACES, and BODIES signal the start of the respective sections. As you can note in this example, faces belonging to the initial mesh are not necessarily triangles. During the iteration of the shape, non-triangular faces will be automatically triangulated by adding a vertex at its center and creating edges connecting this new point with each of the original vertices. Faces don't have to be planar and they can thus connect vertices which are also very dispersed. Even though the total surface itself does not need to be oriented, each face is supposed to have a specific orientation. The face oriented normal is defined by the "right hand rule", according to the direction in which the edges composing the face are defined (in section EDGES) and interconnected (in section FACES). In defining a body, the boundary faces must have outward normals. The properties and attributes of an element are given on the same line after its definition.

The example reported in Fig. 2.1 is the case associated to a mound of liquid wetting a substrate.

The contact angle between the liquid surface and the tabletop is adjustable, to simulate the different degrees to which the liquid wets the table. The liquid is computed with an initial mesh associated to a cube with one face on the tabletop (the $z = 0$ plane). In order to define the contact, the face laying on the substrate is omitted and removed from the listed elements composing the liquid body. While the face is removed, we associate to the edges around face 6 an energy integrand that results in the same energy we would get if we did include face 6. If we let the interface energy density for face 6 be T , then we want a vectorfield \mathbf{w} such that:

$$\iint_{face6} T dS = \oint_{face6} \mathbf{w} dl \quad (2.2)$$

By Green's Theorem, it is necessary to find a certain \mathbf{w} whose curl is equal to the value of T . In practice the line integral defined in the datafile sums up strips of surface. The contact angle in the software is parametrized as the angle in degrees between the table and the surface on the interior of the drop. This angle can be adjusted by assigning a value to the variable angle both in the datafile and while running the simulations.

```

vertices
1  0.0  0.0  0.0  constraint 1  /* 4 vertices on plane */
2  1.0  0.0  0.0  constraint 1
3  1.0  1.0  0.0  constraint 1
4  0.0  1.0  0.0  constraint 1
5  0.0  0.0  1.0
6  1.0  0.0  1.0
7  1.0  1.0  1.0
8  0.0  1.0  1.0
//9  2.0  2.0  0.0  fixed  /* for table top */
//10  2.0 -1.0  0.0  fixed
//11 -1.0 -1.0  0.0  fixed
//12 -1.0  2.0  0.0  fixed

edges /* given by endpoints and attribute */
1  1 2  constraint 1 /* 4 edges on plane */
2  2 3  constraint 1
3  3 4  constraint 1
4  4 1  constraint 1
5  5 6
6  6 7
7  7 8
8  8 5
9  1 5
10 2 6
11 3 7
12 4 8
//13 9 10 no_refine fixed /* for table top */
//14 10 11 no_refine fixed
//15 11 12 no_refine fixed
//16 12 9 no_refine fixed

faces /* given by oriented edge loop */
1  1 10 -5 -9
2  2 11 -6 -10
3  3 12 -7 -11
4  4 9 -8 -12
5  5 6 7 8
//7 13 14 15 16 no_refine density 0 fixed /* table top for display */

bodies /* one body, defined by its oriented faces */
1  1 2 3 4 5  volume 1  density 1

read

```

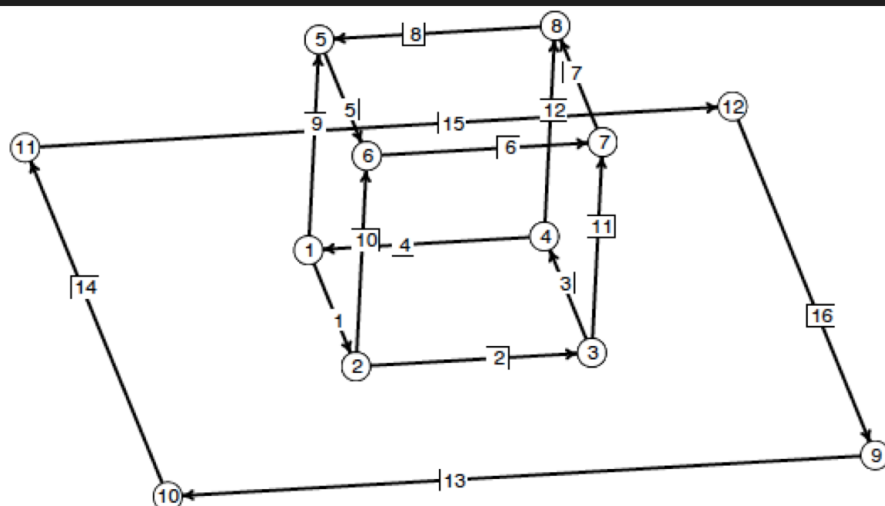


Figure 2.1 – On the top we show a part of the datafile associated to the mound problem, most precisely the section where the elements of the initial mesh for the simulations are provided. On the bottom, the relative visualization of the vertices and edges as defined in the datafile. [Surface Evolver Manual]

3 Liquid Assisted Selective Area Epitaxy

3.1 State of the Art

The possibility to prepare an ordered array of nanowires (NWs) allows more effective integration of nanostructures into macroscopic devices. Ordered arrays became possible thanks to the development of high-resolution lithographic techniques, ensuring the fabrication of preferential locations where the crystal growth can take place.[30, 104, 105, 106] The fabrication process involves selective etching of part of the substrate according to predefined mask. Thanks to the mask it is possible to control many characteristics of the patterning, like the size, the shape, the holes-interdistance and the depth of the regions where the growth will take place. Such features are relevant not only in determining optical or electronic properties of the final device, but even more importantly in the realm of bottom-up approach, they can influence the dynamic of growth and thus the possibility to obtain good yield and uniformity.[32, 107] Beyond the geometrical constraint inherited by the mask selection, there are different other parameters that play a key role in the growth process, such as the growth temperature and the material fluxes. On the atomistic level, the growth temperature control absorption and desorption rates and diffusive processes. The diffusive processes, together with adsorption and desorption rate, are essential in determining the effectiveness of selectivity of the mask and also the rate at which the already formed nanowires can proceed the growth. From a macroscopic point of view, the sum of all these microscopic processes sum up into the selection of a specific crystal phase composing the bulk of the material and a certain faceting composing the boundaries of the crystal.[63]

Once the most stable crystal phase has been identified, another step in the epitaxial growth process is the selection of the growth direction. Any crystal system is characterized by an ordered and repetitive lattice whose frame is given by the translation along all 3 dimensions of the same unit cell. The unit cell is the smallest repeating group of atoms having the full symmetry of the crystal structure. According to the symmetry of the crystal, different directions and planes can be related to each other by mathematical transformation making them equivalent also from an energetic point of view. This equivalence among namely different planes and directions is what unifies a crystallographic family. In crystals holding high space symmetry

structures there is not a principal axis with higher rotational symmetry: the axis designation is therefore arbitrary and has N invariant solutions, with N the number of directions belonging to the same family. Cubic and orthorhombic crystal systems, usually composing the structure of III-V semiconductors, possess high symmetry space groups thus creating the uncertainty in the selection of an unique preferential direction.[108, 109]

One of the main requirements for improving the performances of nanowire's array based devices is the conformity of the orientation of the different nanowires: a vertical alignment with respect to the substrate is traditionally preferred for photovoltaics and electronics applications. Nevertheless, also preferentially tilting nanowires are becoming relevant for applications in quantum computing, where the crossing between multiple nanowires becomes a resource, but we will not consider this case in this chapter.[110, 111] For nanowires composed by semiconductors the energetic invariance among multiple growth directions makes difficult to realize high yield homogeneous alignment over the whole sample. In this chapter we will focus on the contribution of the liquid phase in increasing the yield of vertically oriented nanowires. Firstly, we present the preferential configurations of the liquid droplet inside a cylindrical geometrical constraint (representing the hole in the pattern) and how their wetting properties are related to the outcome of epitaxial growth. Secondly, we predict the dynamics of diffusion inside the confined liquid particle and we analyze the effect of the shadowing caused by the sidewalls in creating an As concentration gradient influencing the nucleation dynamics. Lastly, we analyze the wetting behaviour of liquid into cavities having smooth sidewalls and we observe the consequences on the successive nanowire's growth.

3.2 Wetting behaviour into cylindrical cavities

Our computational study analyzes the morphology of liquid droplets into flat-bottomed round wells as a function of their volume and of their disposition into the cavity. The shape of the cavity resemble the experimental setup taken as a reference and we fixed the ratio between the width and the height of the hole, also called the aspect ratio (d/h), to the value of 2. Wettability analysis needs contact angle measurements as primary data, indicating the degree of wetting during the interaction between a solid and a liquid. The contact angle is defined as the angle formed by the intersection of the liquid-vapor interface and the liquid-solid interface. The interface where solid, liquid, and vapor co-exist is referred to as the "three phase contact line" or also "triple line". The measured contact angles with the floor and the walls of the cylindrical cavity are 51° and 116° , respectively, obtained by ex-situ SEM analysis. The difference in the wetting angle is due to the fact that the floor and the wall of the cavity are made of different material: Silicon (the substrate) and Silicon Dioxide (the mask for the selective area epitaxy). The geometrical configurations in which the liquid can be found in the well can be divided into 5 main regimes that are shown in Fig. 3.1.

The first and simplest situation depicted in the inset a) concerns a liquid which is not in contact with the walls of the well and thus the drop is an half space convex region bounded by a single plane with a constant contact angle. This kind of shape is the simplest one and can

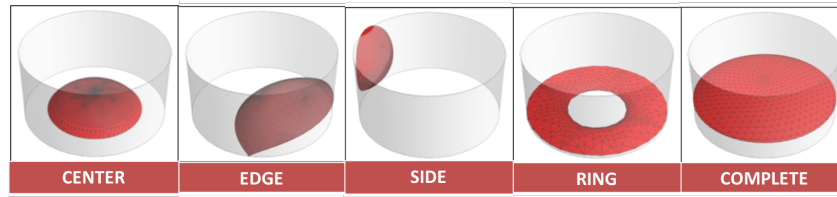


Figure 3.1 – Representation of the 5 main regimes of the droplet initial configuration in the round well.

be associated to a spherical cap. The second configuration represented in inset b) shows an isolated blob which intersect the floor/wall junction, which is energetically favorable when the droplet has small volume or system is characterized by a sum of floor and wall contact angles major then 90° ; in this case the drop can be subjected to two different surface energies according to the nature of the floor and the walls respectively. The third case illustrated in part c) describes the formation of an isolated droplet that attaches on the non-planar walls of the cylindrical well. In inset d) we show the configuration in which the droplet just wets the side of the hole, creating a ring-like shape. Finally, in panel e), we represent a liquid which fully covers the bottom part and the TPL is distributed just on the lateral walls. Also in this condition, like in the first case, the minimal energy shape of the droplet is given by a spherical cap.

The equilibrium shape of the liquid surface in the different configurations is computed with Surface Evolver, introduced in chapter 2. The liquid-vapor interface is set with interfacial energy settled by default at 1, while the energetics of the liquid-solid interface is defined through fixed energy integrals, dependent on the contact angles with both the floor and the wall of the well. Along the intersection between floor and walls, the use of vertex scalar integrands is implemented in order to merge the floor and walls contribution. The scalar integrand is reported in eq. (3.1) and it was applied to the two external vertices composing the liquid on the wall-bottom interface, respectively with a plus and a minus sign.

$$FLOORT * (rad^2 * atan2(y, x) - x * y)/2 \quad (3.1)$$

These integrals are applied to the 2 vertices delimiting liquid

The iterations towards the complex interfacial static equilibrium is performed at fixed droplet volume and contact angles. Everytime a new volume is analysed, the simulations were started by the volume proper of the initial shape and then increased step by step after iteration towards equilibrium at each stage. An example of developmental shape is shown in Fig. 3.2

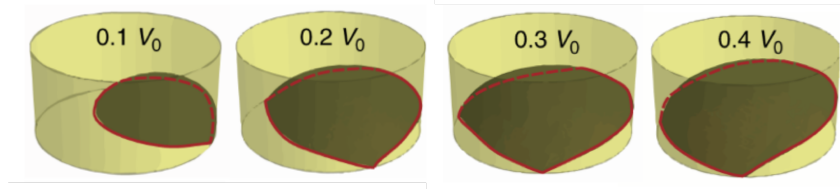


Figure 3.2 – Sketch of the development of the liquid shape at the edge of the cylindrical cavity as a function of the droplet volume

3.3 Computational results wetting into cavities

In this section we summarize the results of our simulations. We show the computation of the surface energy of the equilibrium shape of the liquid droplet as a function of the droplet volume for the 5 different configurations shown in Fig. 3.3.

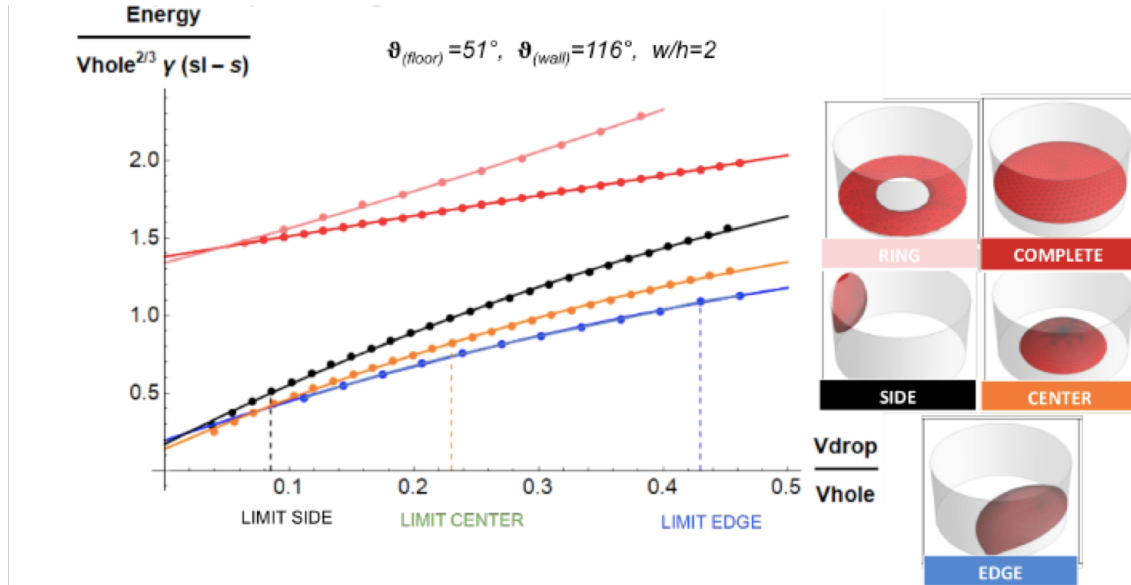


Figure 3.3 – Computation of the droplet's normalized surface energy as a function of the droplet's volume for different configurations inside a cylindrical cavity. The normalization of the surface energy involves both the droplet's volume and the difference in interfacial energy between the solid-liquid and the solid-vapor system. The droplet's volume is normalized by the cavity's volume. On the right side we show the images of the configuration considered.[112]

Any system at equilibrium adopts the configuration associated with the lowest energy state. From the results shown in Fig. 3.1, the preferential configuration of the liquid droplet is the one associated with the lowest energy curve. For small droplet's volumes, the most stable shape is the one pinned at the edge of the cavity, partially wetting the bottom and the sidewalls of the cavity. Due to the limited size of the cavity, the range of allowed droplet's volume for each shape is limited as well. For each configuration the threshold volume depends on the aspect ratio of the cavity and on the contact angles characterizing the system. For normalized

droplet's volume larger than 0.45, the only configuration remaining allowed is the complete configuration which will remain the preferential one until spreading outside of the cavity. From these results we can conclude that, once the aspect ratio of the cavity and the wetting angles of the system are defined, it is possible to predict the development of the preferential wetting configuration of liquid's droplet as a function of the volume of the droplet. From an experimental point of view it means that the droplet's volume can be used as a parameter to trigger different configurations in the system.

In the case of the VLS growth of NWs performed in our laboratory, this information is particularly relevant also in relation to the recipe that has been optimized in the last years. This recipe contains a pre-deposition step of just Gallium on the substrate prior to the real preparation of the NWs. Such additional step allows Gallium atoms to diffuse towards the preferential regions and coalesce into droplets. By finely tuning the time of the Gallium deposition, it is possible to change the average size of the metal drops thanks to the consequences of the Oswald ripening phenomenon. The successive NW growth process resulted to be influenced by the modification of time of this step. In Fig. 3.4 we show the comparison between two arrays prepared with the same growth conditions and pattern characteristics, but having different Gallium deposition time, specifically 10 minutes (left) and 15 minutes (right). [112]

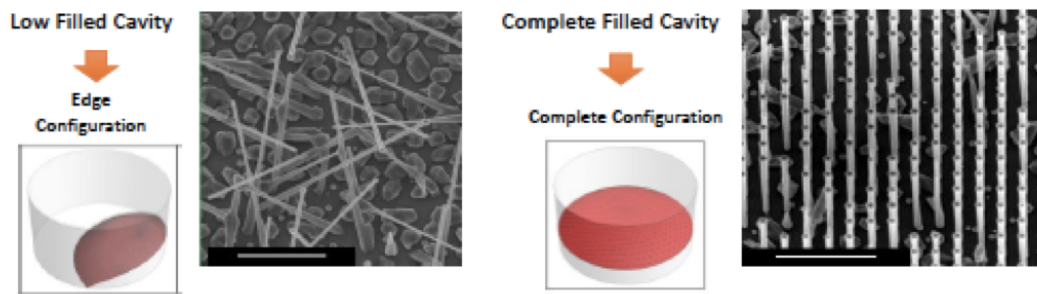


Figure 3.4 – Comparison between NW's growth obtained after short (left) and long (right) time of Gallium pre-deposition. We deduce from our previous results that the initial configurations of the droplet are the edge and the complete one respectively. [112]

From the SEM images in Fig. 3.4 we can appreciate the increase in the vertical yield thanks to the modification of the length of the Gallium deposition time. We find that for small Gallium deposition time, the amount of material available is not enough for filling the whole cavity. From our experimental measurements, we conclude that in these conditions, the droplets forming adopt the edge configuration. For larger deposition times, the volume of the droplets is large enough to fill completely the cavity: this situation corresponds to the complete configuration of the simulations which also ensure higher vertical yield. We believe that a complete filling of the hole by the Gallium increases the probability to obtain vertical nanowires because the symmetry of the cavity system is preserved. Intuitively, this helps the verticality because it can lead to a more homogeneous environment at the bottom of the hole for the first layers of crystal growth.

3.4 Initial stages of NW's growth

The VLS growth mode usually takes place as a homogeneous layer-by-layer epitaxy confined in the regions where the liquid droplet is present. From this assumption, the results obtained in the previous sections would be considered enough for explaining why a complete filling of the hole increases the probability to obtain vertical nanowires. Indeed, a partially filled cavity creates a system characterized by a gradient in the growth velocities: the uncovered regions are still in contact with the vapor and continue to react at a different rate with respect to the regions in contact with the liquid. The disomogeneity in the epitaxial growth rate can lead to the formation of slanted growth front causing the successive tilting of the whole crystal. To verify this hypothesis we decided to characterize the shape of the crystal seeds, formed after few minutes of nanowires growth. In Fig. 3.5 we show the AFM images of GaAs crystals after 15 minutes Gallium pre-deposition and 2 minutes of NW's growth into cavity having diameter of 45nm (a) and 90nm (b). [112]

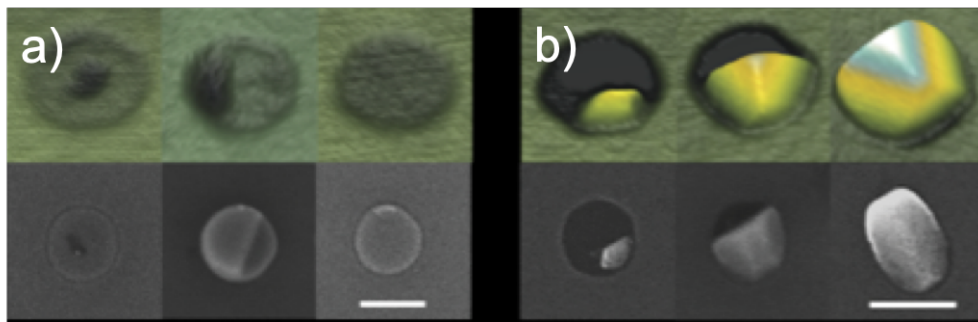


Figure 3.5 – AFM images of the initial stages of growth of GaAs crystals, obtained after 2 minutes nanowire's growth. The two samples differ for the cavity's diameter, which is respectively 45nm (a) and 90nm (b). The scale bar are 100nm and 200nm.[112]

Thanks to these AFM images it is possible to recognize the difference in the initial stages of the growth caused by the different droplets configuration. In particular, inset (a) can be associated with the complete filling of the hole. Multi-layer terraces and rings can be recognized at the bottom of the cavity. These results are a bit in contrast with the expected layer-by-layer growth mode and show that the fundamental mechanisms taking part to the growth process need further clarifications. In inset (b) the larger diameter of the cavity increases the range of stability of the edge configuration. For the same Gallium deposition time as the 45nm diameter holes, this means that the amount of material is not enough to ensure the transition to the complete configuration, thus allowing us to observe the crystals obtained from an initial condition of partially filled cavities. Such crystals have the shape of islands with large slanted lateral facets in agreement with the presence of tilted growth fronts and reasonably in agreement with a consequent growth of slanted nanowires.

3.5 Arsenic diffusion and shadowing effect

The atypical observation of ring shapes at the beginning of the growth process suggested that there were additional considerations needed to explain the growth mechanism of nanowires obtained from patterned substrate. We thus decided to consider another parameter detrimental to fully describe the droplet environment at the first stages of NW's growth. This parameter is the arsenic concentration, specifically As_4 in the liquid: due to the confinement into cavity and the shadowing effect caused by the sidewalls the flux of material inside the liquid will not be homogeneous and may create gradients influencing the growth dynamics. Fig. 3.6 (a) illustrates the configuration of the gallium droplet in the symmetrically filled hole and the directionality of the As_4 flux characteristics of the MBE. In addition we remind that the substrate rotates for the whole time of the process. We computed the concentration profile of the arsenic by numerically solving the Fick's equation (3.2), where J stands for the flux of the specie, D is the diffusion coefficient and c is the concentration profile in 3D.

$$J_i = -D\nabla c_i \quad (3.2)$$

The solutions to the the Fick's law are obtained through finite element method for each orientation of the impinging flux. The final concentration profile of the diffusing material inside the droplet is calculated as time average of all the solutions calculated in a complete period of rotation of the flux around the z -axis of the cylinder. The boundary conditions for solving the differential equations are reported in eq. (3.3) and (3.4):

$$c(x, y, z) = 0.1, [z = 0] \quad (3.3)$$

$$c(x, y, z) = 0.1, [x^2 + y^2 = 0.5^2] \quad (3.4)$$

Equations (3.3) and (3.4) define the absence of diffusion through the substrate (located at $z=0$) and the sidewalls of the cavity respectively, thus limiting our analysis to the internal part of the cylindrical cavity. No bouncing or desorption effects were taken into consideration. We considered the existence of an effective impinging flux just on the surface of the droplet intersecting the time dependent flux. The impinging time dependent flux also has an orientation dependent value: it has maximum intensity when it hits a region of the surface with normal parallel to the direction of the flux itself. The choice of the concentration is arbitrary and not relevant for obtaining numerical results.

In Fig. 3.6 we show the time averaged results of the concentration profile obtained for two

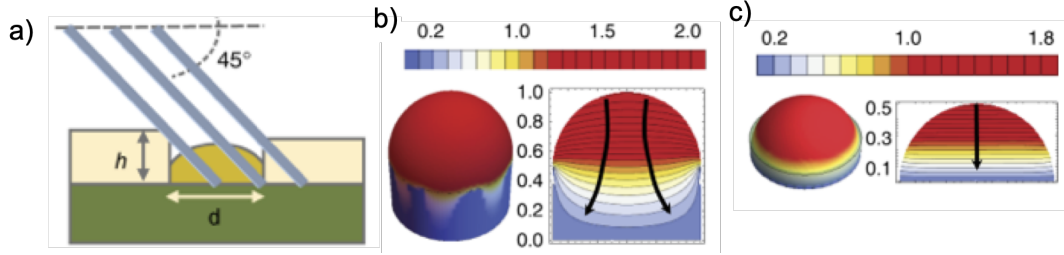


Figure 3.6 – (a) Sketch of the droplet configuration in the cavity with the directionality of As fluxes characterizing the MBE system. Computed 3D plot of the As concentration profile and its cut through the droplet center for cavities with aspect ratio (d/h) 2 (b) and 6 (c) [112]

different aspect ratio (d/h) of the hole: 2 (b) and 6 (c). The gradient in the arsenic concentration can be appreciated in the change of colors from which we identify the directionality of the flux (indicated by black arrows) in the cross-sectional plots (right column of the insets). For low aspect ratio ($d/h=2$) ratios, the arsenic flux is directed towards the oxide-substrate interface line due to the strong shadowing effect caused by the geometry of the cavity. The lack of arsenic in these zones creates a permanent concentration gradient which may alter the homogeneity in the growth dynamics. By increasing the aspect ratio, the arsenic diffusion flux is turned away from the substrate-oxide interface line in favor of a more perpendicular alignment. When the d/h ratios are too large, concentration gradient toward the oxide-substrate line becomes negligible. Hence, the arsenic diffusion towards the substrate becomes homogeneous proving that after a certain aspect ratio the shadowing effect becomes irrelevant.

Finally, we decided to verify what happens to the arsenic concentration profile in the case of droplets appearing in the edge configuration. For this analysis the droplet shape is approximated to a cap of a sphere intersecting a cylinder, with the center of the spherical cap in correspondence of the cylindrical sidewalls, as represented in the sketch in the first column of Fig. 3.7. The resolution of the Fick's law is performed in the same way as explained for the symmetrically filled cavity case. The density plots of the concentration profile for cavities having different aspect ratio, specifically 2(a), 4(b) and 6(c) are shown in Fig. 3.7.

As shown for the symmetric case, the shadowing effect strongly effect the concentration profile inside the droplet, creating a gradient in the As concentration which will enhance the diffusive processes towards the Silicon-Silicon Dioxide interface. In this case, even though there is gradient directed towards the edges of the cavity, the asymmetric nature of the wetting itself will provoke the asymmetry in the growth front.

3.6 Smoothing the sidewalls

In this additional section we introduce an innovative approach which combines the functionalities of the selective area epitaxy and the freedom of engineering the wetting angle. Also the experimental approach is interesting due to the absence of traditional lithographic

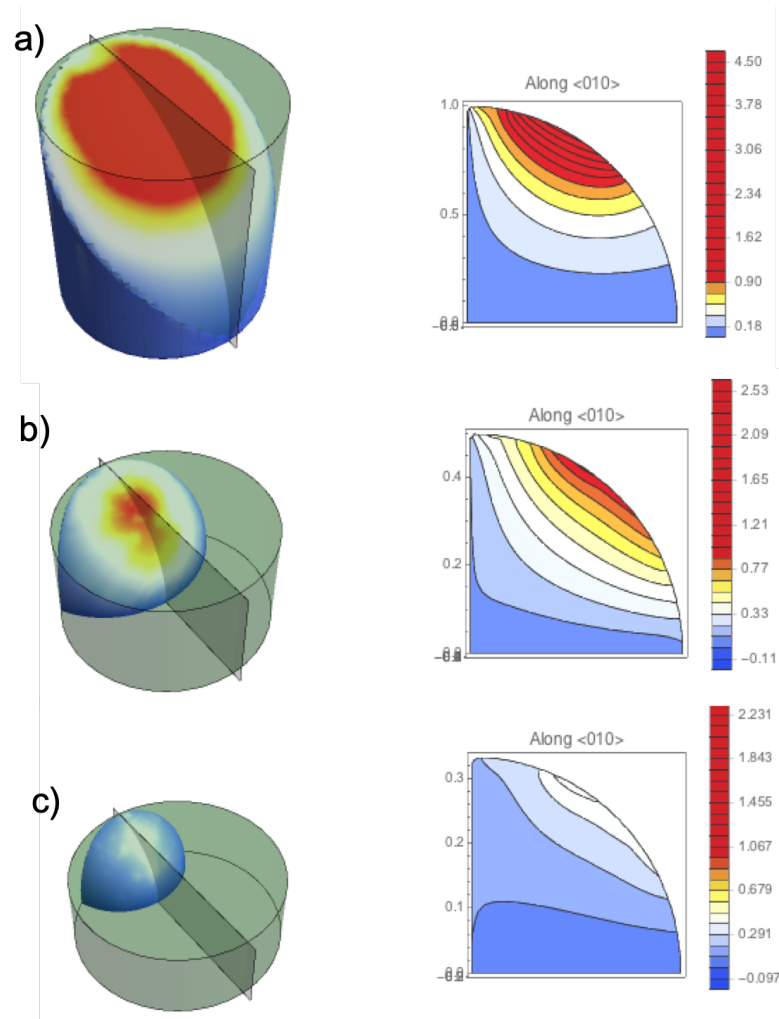


Figure 3.7 – Sketches of the asymmetrically filling droplet configuration inside a cylindrical cavity and corresponded sliced contour plot of the calculated Arsenic concentration profile for different aspect ratio: a) $d/h=2$, b) $d/h=4$, c) $d/h=6$. [112]

techniques while ensuring the localization of nanoparticles into ordered arrays. [113] The procedure follows a 2 steps annealing for the preparation of ordered nanowires arrays from micron-features. The micro-features are composed by a thin layer of gold deposited on a thin layer of antimony. The first annealing step induces the dewetting of the gold and causes the formation of nanoparticles close to the center of the micro-features. With the second annealing step, at higher temperatures, the nanoparticles are used to imprint their shape onto the oxide mask covering the substrate. Additional etching steps follow to remove the gold particles and reach the Silicon substrate underneath the oxide, to obtain the patterned sample ready for epitaxy. In Fig. 3.8 a) the resulting geometry of the cavities formed thanks to this approach are shown in AFM measurement of the profile. From the color contrast we can appreciate the lateral roundness and the ring formation around the nanoparticles. The arrow indicates the Si open area diameter. Thanks to the parabolic shape of the imprinted

hole it is possible to control the diameter of the substrate open area by controlling the reactive ion etching (RIE) parameters in the last part of the process. The growth of GaAs nanowires through self-catalyzed VLS approach was demonstrated and optimized, reaching yields of vertical NWs around 60%. [113] By analyzing the gallium pre-deposition step of the growth process, it was observed that the highest vertical yield are obtained for deposition time leading to high wetting angles of the gallium droplet (higher than 85°). The possibility to modify the wetting angle, while ensuring the localization of the droplets, represents a very interesting result since high vertical yield is often associated with high droplet wetting angle. In order to investigate the morphological advantages of these nanoimprinted structures, we performed simulations on the wetting behavior of sessile-droplets blocked in holes without edges or corners. Fig. 3.8 b) shows the cross section of the Gaussian curve representing the geometrical constraint imposed on the droplet. The aspect ratio between the height and the width of the hole is set to 1:10 to best approximate the experimental measurements. For the same reason, the interface between Si and SiO₂ is placed at $z = -0.66$, where a sharp modification in the contact angle is implemented.

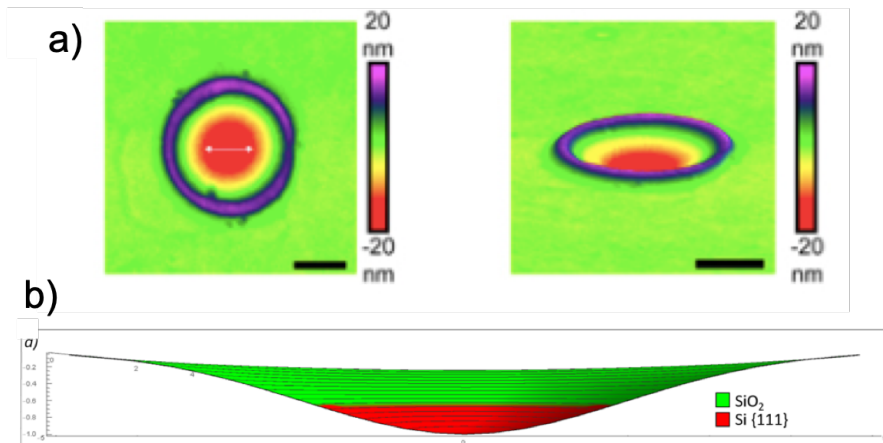


Figure 3.8 – (a) Color-coded AFM images of a single nanohole, top view on the left and 70°-tilted view on the right. Scale bar 100 nm. b) Cross section view of the 3D-Gaussian representing the hole geometry. The interface between Si and SiO₂ is placed at $z = -0.66$ [113]

We computed the morphological evolution of the droplet shape towards equilibrium thanks to Surface Evolver (section 2.2.1 for details). The contact angles of 51° and 116° are respectively for Silicon (red region) and for SiO₂ (green region). The droplet is placed at the bottom-center of the hole and the system conserves a circular symmetry throughout all simulations. Rather than focusing on the surface energy of the system we decided to focus mostly on the variation of the shape of the droplet as a function of the droplet's volume. In particular, we studied the change of the Ga wetting angle with the increment of the Ga droplet volume (V_{drop}). The results of our simulations are shown in Fig. 3.9.

In our results we study the apparent angle, which differs from the Young's equation related contact angle because its value cannot be taken as a reliable indication of the energetics of

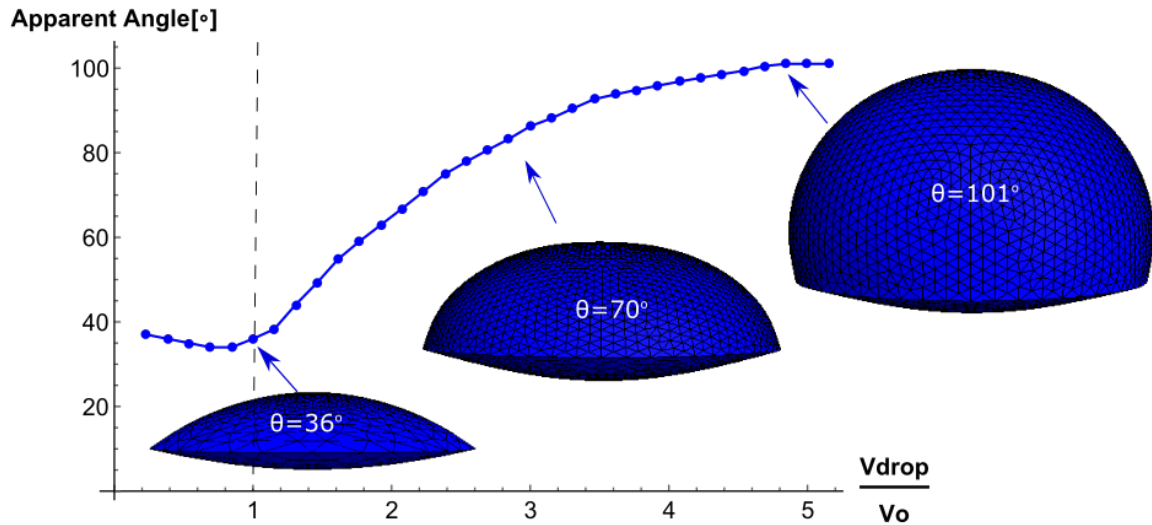


Figure 3.9 – Variation of the apparent angle of sessile droplets confined in a Gaussian-shape two-material hole morphology as a function of the volume of the droplet. The normalization V_0 is arbitrary. Values are obtained from the shapes evolved by the software Surface Evolver. [113]

the system. We define the apparent angle as the angle between the Ga droplet tangent at the triple-phase line and the horizontal plane. The dependency of the wetting angle on the volume is not monotone and can be analysed by distinguishing 2 different regimes. In the first regime, there is a reduction of the apparent angle for increasing droplet's volume, until the value of 34° at $V_{\text{drop}}/V_0 = 1$. This decrease is connected to the variation of the inclination of the sidewalls, particularly relevant close to the center; the resulting apparent angle corresponds to the difference between the value of the Ga contact angle on silicon (51°) and the inclination of the sidewalls of the hole. This first regime indicates the interval of volumes in which the droplet is allowed to spread. At $V_{\text{drop}}/V_0 = 1$, the presence of the minimum apparent angle value indicates that the droplet perimeter reached the sharp two-material separation interface, thus changing the dynamics of wetting. In the second regime, an increase in the droplet volume results into an increment of the droplet's apparent angle. For large volumes, the apparent angle reaches saturation at the value of 101° , in agreement with the expected apparent angle for a Gallium droplet freely wetting a tilted SiO_2 substrate (with real contact angle of 116°). The possibility to modify the apparent angle of droplets by spatial confinement is known as 'pinning effect'. We conclude that the observed high wetting angles are the result of the pinning of the droplet at the 2 materials interface line which, in the absence of edges constraining the shape, is free to develop larger wetting angle for larger volumes.

4 Liquid stability on top of cylindrical pillars for growth direction control


In this chapter we will focus on an approach for optimizing the growth of NWs, which can be taken as the complementary solution to the cavities-based selective area epitaxy. This method combines the localization of the droplet and the engineering of its wetting angle thanks to the patterning of the substrates into oxidized nanoscale pillars.[114] From an experimental point of view, this approach revealed to be interesting for obtaining vertical III-V-based structures when attempting to grow NWs starting from Si(100) substrates. Even though the yield obtained is around 10%, this remains among the best achievements for Au-free vertically [100]-oriented flat nanostructures. Nevertheless, from a more fundamental point of view the method used and the correlated tuning of the properties of the liquid catalyst droplet in terms of size and wetting angle deserve interest due to the combination of droplet confinement with a varying degree of effective wetting angles. Before entering into the details of the wetting on top of oxidized pillars, ensuring the confinement solely on the top part, we will focus first on the analysis of droplets wetting pillars composed by just one material, in order to clarify the simplest case first. At first we introduce important considerations regarding the droplet stability on top of single-material columns and their effects on the successive stages of the growth of NWs from an experimental point of view.[80] The second part of this chapter will focus on the single-material-column expansion given by the combination of two different materials composing the pillars: the tactic enabling a more precise confinement and a more refined tuning of the wetting properties, with the perspective of obtaining a larger range of NW's growth outcomes.

4.1 Droplet stability on top of single-material-pillars

In this section we report a detailed analysis of liquid stability on top of cylindrical pillars composed by just one material. Many considerations, even though apparently trivial, can clarify some interpretations and fundamental aspects of materials science that need to be revisited. Such discussions are important for developing new crystal growth models which are coherent with the special system represented by the liquid assisted growth mode. The theoretical dissertation and their main conclusions are then supported by experimental

evidences obtained by our colleagues. In particular, we consider the case of InAs NWs grown by self-assembly mode in MBE on top of GaAs(111)B substrates. The analysis of the wetting stability of the Indium droplet is done on top of these NWs after an annealing step, responsible for the formation of droplets. Thanks to SEM investigation, we collected enough data to verify our considerations about droplet stability and a conformal evolution with an increase of size. [80]

Questioning liquid droplet stability on nanowire tips: from theory to experiment

Lea Ghisalberti¹, Heidi Potts¹, Martin Friedl¹, Mahdi Zamani¹,
Lucas Güniat¹, Gözde Tütüncüoğlu¹, W Craig Carter^{1,2} and
Anna Fontcuberta i Morral^{1,3} 

¹Laboratoire des Matériaux Semiconducteurs, Institut des Matériaux, Ecole Polytechnique Fédérale de Lausanne, 1015 Lausanne, Switzerland

²Department of Materials Science and Engineering, MIT, Cambridge, MA, United States of America

E-mail: anna.fontcuberta-morral@epfl.ch

Received 20 January 2019, revised 25 March 2019

Accepted for publication 26 March 2019

Published 25 April 2019



Abstract

Liquid droplets sitting on nanowire (NW) tips constitute the starting point of the vapor–liquid–solid method of NW growth. Shape and volume of the droplet have been linked to a variety of growth phenomena ranging from the modification of growth direction, NW orientation, crystal phase, and even polarity. In this work we focus on numerical and theoretical analysis of the stability of liquid droplets on NW tips, explaining the peculiarity of this condition with respect to the wetting of planar surfaces. We highlight the role of droplet pinning at the tip in engineering the contact angle. Experimental results on the characteristics of In droplets of variable volume sitting on the tips or side facets of InAs NWs are also provided. This work contributes to the fundamental understanding of the nature of droplets contact angle at the tip of NWs and to the improvement of the engineering of such nanostructures.

Supplementary material for this article is available [online](#)

Keywords: nanowire, contact angle, stability, tilting, growth direction

(Some figures may appear in colour only in the online journal)

Introduction

Nanowires (NWs) are filamentary crystals with a tailored diameter in the few nanometer range. Semiconductor NWs and in particular III–V NWs, are promising building blocks for next-generation computing, sensing and energy harvesting devices [1–7]. NWs can be obtained in arrays of uniform structures [8–11] as well as by self-assembly on a substrate [12–16]. In this case, the characteristics of the structure may exhibit a higher degree of variation in terms of structure, growth direction and even crystal polarity. Flexibility of NW characteristics in the self-assembled approach may originate from the dispersion in NWs distance, diameter and nucleation points [17–19].

The most common method used for the growth of NWs is the vapor–liquid–solid method, VLS, in which a liquid metal

is used to preferentially decompose and gather growth precursors. Upon supersaturation of the precursors in the liquid phase, a solid NW is formed [20, 21]. Recently, it has been shown that the characteristics of the liquid droplet are essential for many aspect of the growth of the NWs. In particular, it has been shown that the droplet contact angle with the solid NW determines the crystal phase, growth direction, orientation and polarity of the NW itself [8, 22–26]. To that end, we believe that the direct translation of capillarity laws from the planar to the non-planar nanoscale case has not been discussed with enough depth. Important works have been published regarding the possible role of edges [27–29] and the effect of the droplet volume on the contact angle [25, 30]. However, given the prominent role of the contact angle in NW growth, this point deserves clarification. In this paper, we define basic capillarity laws determining the stability of nanoscale droplets on the tip of NWs. We start by providing a theoretical basis from a historical point of view.

³ Author to whom any correspondence should be addressed.

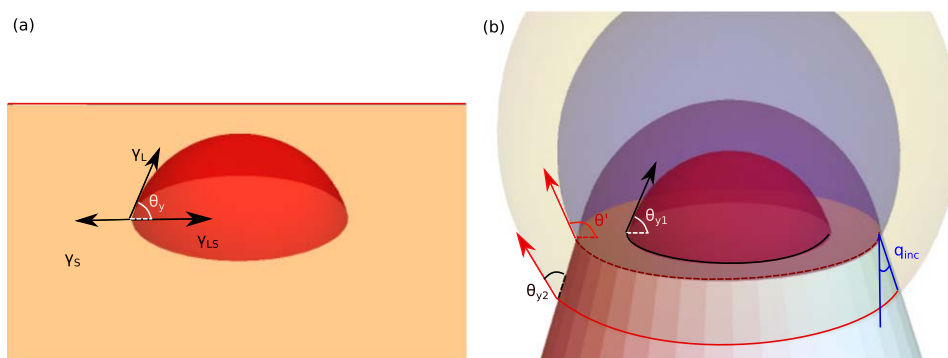


Figure 1. (a) Sketch of a sessile droplet wetting an ideal infinite solid and whose shape is characterized by the equilibrium angle, θ_Y , minimizing the surface energy of the system. (b) Sketch representing the pinning effect characterizing the wetting of variable volume droplets on top of a truncated cone. When the droplet triple phase line (TPL) is in touch with the edge, there is a continuous range of contact angles available from θ_{Y1} and $\theta_{Y2} + q_{incl}$, with q_{incl} representing the inclination of the sidewalls and θ_{Y2} the sidewalls equilibrium angle.

We then follow-up with numerical simulations that explain the stability conditions of the droplet, based on surface energy minimization. Finally, we provide experimental results on the In (droplet)/InAs (NW) system, consistent with the theoretical considerations. Our work provides new insights into the wetting properties of VLS droplets and improves our understanding of this NW growth mechanism.

Theoretical considerations

The Young–Dupré’s equation describes the wetting of a sessile droplet on a flat substrate. It defines the contact angle θ_Y as a balance between adhesion to the surface and the cohesive forces of the droplet constituents. Figure 1(a) shows the typical setting of the equation. γ_S , γ_L and γ_{SL} correspond respectively to the solid–vapor, liquid–vapor and liquid–solid interfacial energies. In the Young–Dupré equation, only the capillary forces in the plane of the solid sum to zero

$$\gamma_S = \gamma_{SL} + \gamma_L \cos \theta_Y. \quad (1)$$

Equation (1) assumes that the atoms in and on the surface of the solid are immobile. The vertical capillary forces are balanced by elastic stresses resolved onto the solid surface, as their sum should be zero everywhere across the contact surface in order to ensure the equilibrium. This equilibrium may change as soon as the surface available to the liquid becomes finite, close to the size of the liquid–solid interface, as is the case at the tip of a NW. A schematic drawing of four possible volume-dependent-scenarios of a liquid droplet wetting a NW tip is shown in figure 1(b). The droplet should change its shape depending on its own volume. Starting at small volumes, the droplet partially wets the tip in a similar manner as on an infinite planar surface (as in figure 1(a)). With the increase of volume, the droplet extends over the NW tip until it gets pinned at the edge. The line defining the interface between the vapor, liquid and solid interface is usually denoted as the triple-phase-line (TPL). The contact angle, θ_{Y1} , defined as the angle between the NW tip surface and the tangent of the droplet at the TPL is equivalent in these two cases. Further volume increase of the droplet results in an

apparent increase in the contact angle and possible wetting on the NW side facets, both in contradiction with the Young–Dupré equation. To date, most of the theoretical analyses of NW growth have considered the literal interpretation of the Young–Dupré equation. In these works, the surface tensions were interpreted by substituting the pinned angle by the Young angle [8, 26, 31–33]. However, the droplet pins as soon as the TPL reaches the edge, thus no conclusions on the solid–liquid interfacial energy can be derived from the contact angle and the values of the other surface energies [34]. In some cases, the equilibrium angle predicted by the Young equation may be satisfied at certain points of the TPL [29]. However, such considerations do not imply that a droplet is in equilibrium. The equilibrium condition is related to the balance of the entire TPL, where all its points satisfy the Young equation. In addition, one should also consider that the droplet surface should exhibit a constant mean curvature to ensure such an equilibrium condition [35]. In practice, there may be more than one solution, some of them representing droplets in a metastable equilibrium. To summarize, the Young–Dupré equation corresponds to a heuristic capillary force balance construction that lacks generality for anything on finite, non-flat surfaces. In general, the solution should correspond to the shape minimizing the total surface energy.

Numerical simulations of sessile droplets on a NW tip

In this section, we provide numerical calculations of the stability of sessile droplets on NW tips as a function of their volume. We also illustrate how the solid–liquid interface evolves as soon as the droplet becomes unstable. The goal of these calculations is to capture the physics behind the wetting of droplets on NW tips. For this, we have simplified the shape of the NW as cylindrical instead of the most commonly observed hexagonal cross-section. Indeed we observed that for droplet wetting the NW’s top, the general tendency is to maintain a spherical-cap shape. For the range of NW diameters considered here, the corners of the hexagonal cross-section do not influence the overall wetting and thus their

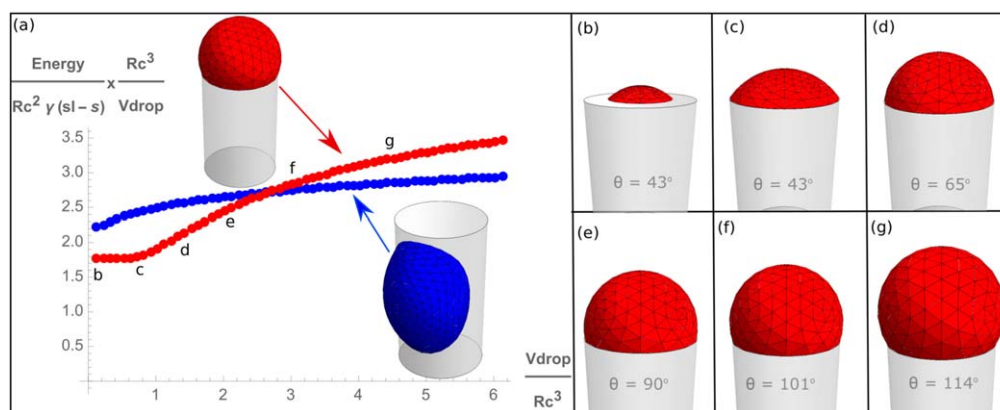


Figure 2. (a) Results of the computation of the droplet normalized surface energy (with respect to the radius of the cylinder R_c and the difference between the solid–liquid and the solid surface tension γ_{sl-s}) as a function of the volume (V_{drop}) for configurations on the top (red line) and on the side (blue line) of a cylindrical NW. The simulations were performed through the finite-element method based software Surface Evolver [36] with a contact angle of 43° on both the side and the top facets. (b)–(g) Illustrations of the equilibrium pinned droplet shape at different values of volume. The different volume values are indicated in the plot of normalized energy versus volume. The increasing volume produces an increase of the contact angle θ due to the pinning effect, as reported for each condition.

influence can be neglected. Regarding the wetting on the side facets, the droplet is not pinned nor influenced by the presence of the edges. It is therefore reasonable to simplify the shape by a cylinder. The chosen material system is liquid indium on InAs so that we can compare the theoretical/numerical results with our experiments.

To analyze the wetting behavior and stability of sessile droplets on top of a cylinder, we have used the modeling program Surface Evolver [36]. We have computed the surface energies of a sessile droplet as a function of its volume. We have analyzed three different configurations of the droplet: on the NW tip, half-way between the top and the side, and on the side of the NW. The half-way configuration is unstable for a cylindrical NW under the assumption of a perfectly flat tip. The results can be found in the supporting information (SI) is available online at stacks.iop.org/NANO/30/285604/mmedia. As input data of the material system, the computations use the experimental equilibrium contact angle of In on InAs, as measured on flat InAs by scanning electron micrographs (SEM). Surface Evolver uses this contact angle, a specified volume and contact constraints to iteratively modify the surface towards the shape of minimum surface energy.

Figure 2(a) illustrates the volume dependency of the surface energy associated with the equilibrium condition of the sessile droplet. According to Laplace's law, the surface energy is proportional to the mean curvature of the shape of the droplet and to its volume. The energy values reported have been normalized by the volume of the droplet, V_{drop} , the difference between the solid–liquid tension and the solid surface tension γ_{sl-l} and the radius of the cylinder, R_c . The red and blue points represent the configuration in which the droplet is respectively on the NW tip or side facet. Starting for the configuration on the NW tip, we see that the surface energy does not vary for increasing volume until pinning. As soon as the droplet is pinned at the edge of the NW tip, the surface energy starts to increase. The surface energy evolution of the droplet on the NW side facet is more gradually increasing. This is due to the particular variation of the shape

of the droplet on the cylindrical side facets. Our calculations show that at a certain volume (between points e and f in figure 2(a)) the droplet on the NW tip becomes less stable than on the side facet. This corresponds to the turning point of its stability and indicates the maximum value of the apparent contact angle. Overall, pinning of the droplet at the edge of the NW tip allows for the engineering of the contact angle from approximately 43° – 100° . This is a remarkably large range of variation.

So far, we have explained the interplay between the droplet volume, the contact angle and the stability of the droplet on the NW tip. Still, some open questions arise with respect to the nature of the TPL and the pinning line. We also have considered that the droplet pins on an atomically sharp corner at the NW edge. Still, chances are that this corner is not atomically sharp and that it exhibits a certain curvature as it is for the edges of the NW cross-section [37, 38].

Figure 3 illustrates the relationship between the advancing triple line, the apparent contact angle, the equilibrium angle, and the orientation of neighboring surfaces. One of the points we want to make is that the macroscopically observed contact angle θ' may differ from the Young contact angle θ_y on a planar substrate. Eventually, the contact angle may continue to be the Young contact angle θ_y locally, if the solid at the TPL deforms gradually and/or if the corner is not atomically sharp. In the left part of figures 3(a) and (b) we depict the variation in the observed contact angle for a droplet moving from the top to the side surface. We differentiate the cases in which the corner between the two surfaces is atomically sharp or round. The latter could also correspond to the case in which the solid at the TPL is deformable. We define the apparent angle θ' as the one measured with respect to the horizontal plane. θ' varies in a step-wise manner or continuously depending on whether the solid at the TPL is atomically sharp or smooth. In the case of smooth corners, θ' depends on the continuous change of inclination as the TPL traverses the rounded corner. From a macroscopic point of view, the abrupt increase of the droplet volume translates into

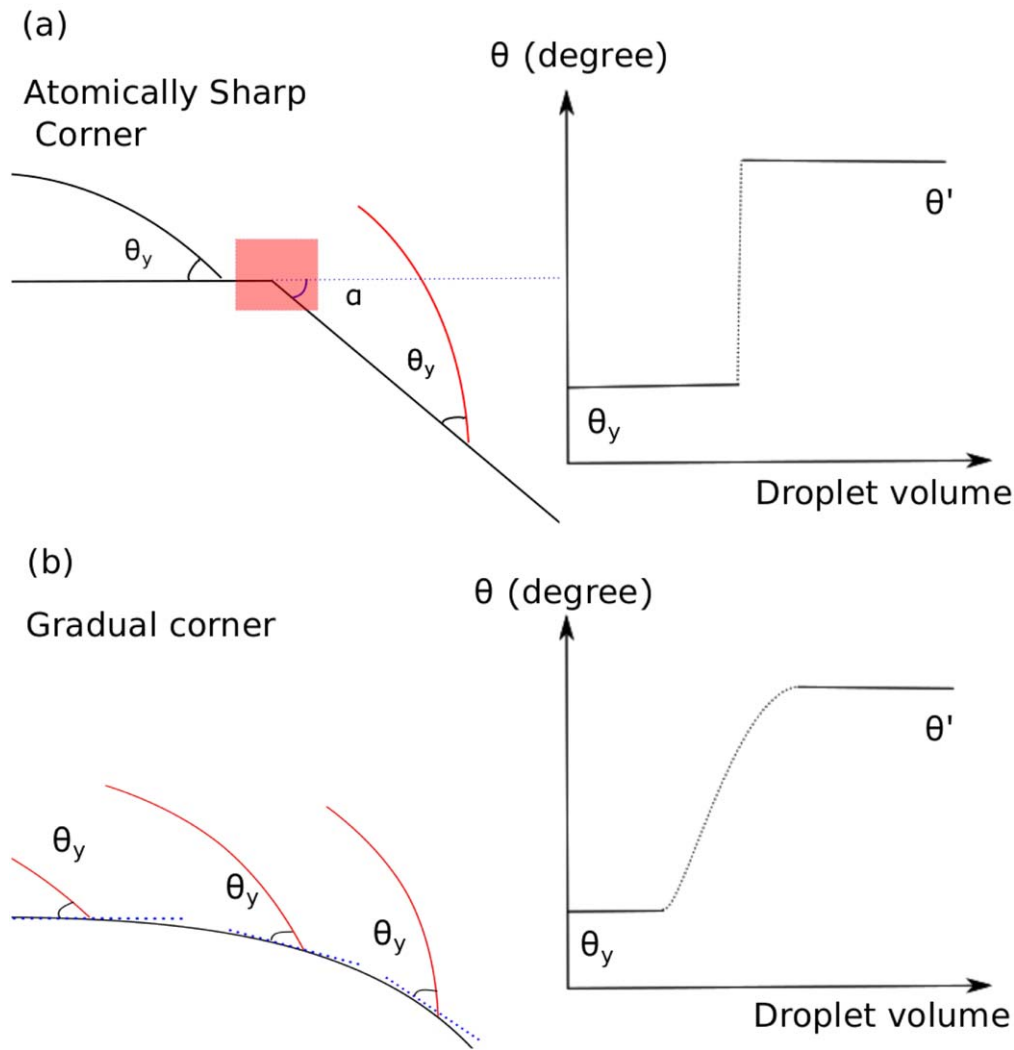


Figure 3. Representative sketch illustrating the behavior of the apparent angle of sessile droplets. The effect of neighboring facets is illustrated for both an atomically sharp (a) and a smooth corner (b). In the first case, the bistability condition of the apparent angle is due to the advancing of the TPL. The rapid change of apparent angle with triple line position in the microscopic illustration results in a seemingly discontinuous change in the macroscopic view.

the appearance of two preferential apparent angles (bistability condition). The first one corresponds to the equilibrium Young's angle θ_y , while the second one is the critical angle $\theta_{crit} = \theta_y + \alpha$, with α being the inclination of the neighboring facet, assuming Young's angle equal to θ_y also on the inclined surface. From a microscopic point of view, the departure of the triple line from the sharp corner needs a finite increase in the droplet volume and the deformation of the solid around the corner, which results in a continuous modification of the apparent angle until the value of the critical angle is reached. This defines the range of available pinned (apparent) angles as $\theta_y < \theta_{pin} < (\theta_y + \alpha)$ and consequently the related range of pinned volume.

We come back now to the detailed discussion of the Young–Dupré equation, to further discuss the force equilibrium at the TPL and its role in determining the droplet stability. In particular, we consider 2 main cases, depicted in figure 4:

Case 1 (C1): The triple line is constrained to a microscopically smooth planar solid-interface as shown in inset a of figure 4 (i.e. atoms in solid are immobile). The position of the triple line changes with droplet volume. The equilibrium at the triple junction requires that contact angles obey the Young–Dupré equation (1).

The previous equations are often derived also as a balance of forces at the TPL and thus as a vectorial equilibrium [39]. The Young–Dupré equation is a necessary boundary condition to a minimal surface problem. That is, it holds for any minimizing surface which has contact lines on smooth surfaces regardless if the surface is a global or local minimum. Furthermore, the condition can be satisfied with the motion of only tens of atoms whereas surface minimization requires long-range transport: it is impossible to stabilize a non-equilibrium contact angle on a smooth surface [35]. In the Young–Dupré equation, only the capillary forces in the plane of the solid sum to zero. The vertical capillary forces are

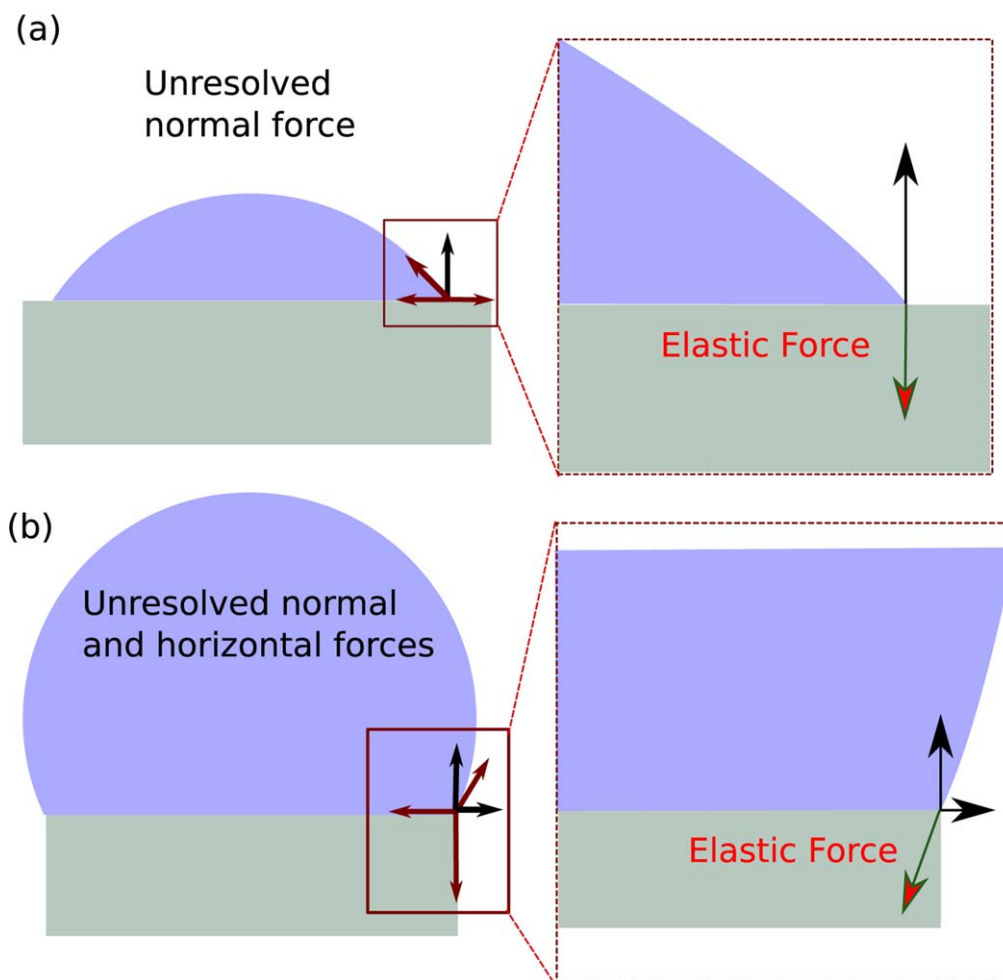


Figure 4. Sketch representing the 2 cases in which the Young equation does not ensure the balance of forces. (a) This happens already to the vertical component of the forces applied on the droplet, which is balanced by the elastic stresses of the solid. (b) When the triple junction is at the corner, the imbalance of the forces happens both in the vertical and in the horizontal plane, allowing the stress field of the solid to rotate at the corner.

depicted in the sketch (a) in figure 4 in the case the atoms on the surface of the solid are immobile. Because the forces must always sum to zero everywhere across the contact surface, the capillary forces are balanced by elastic stresses resolved onto the solid surface. If the solid were elastically compliant (i.e. a thin substrate), it would bend (and thereby reduce the total elastic energy). As an extension of this case, the solid–liquid and/or the vapor–solid interface may deform by diffusion in the solid, such as that observed by Tomsia *et al* [40]. In this condition, the equation (1) is adjusted to account for the deformation of the solid.

Case 2 (C2): The TPL intersects a solid edge and the atoms of the solid are immobile, as depicted in figure 4(b). In this case, the direction of the resolved singular elastic force in the vicinity of the TPL is no longer constrained to be vertical and the stress field can rotate at the edge. The TPL translational degree of freedom is removed and replaced by a variable apparent angle (i.e. the apparent angle increases as the droplet volume increases). The corner will continue to pin the triple line until the condition for capillary force-balance is satisfied on the adjacent solid surface—equivalently, the equilibrium Young angle is satisfied on the adjacent surface.

As discussed above, the range of stable angles can be treated as the limiting case as the solid interface’s radius of curvature goes to zero.

As an extension to case C2, we can consider also the case of rough surfaces. Microscopic corners and edges pin the contact line and the apparent angle can vary until the TPL unpins. Roughness adds further complexities as pinning can also occur at corners where three or more edges intersect and the direction of the edges needs not be parallel to the (macroscopic) TPL. Nevertheless, the elastic/capillary force balance always applies when geometric features are resolved at the microscopic scale. The difference between microscopic and apparent (macroscopic) geometric features gives rise to Cassie phenomena [41].

In summary, so far we have elucidated the volume dependency of the equilibrium condition of sessile droplets wetting the tip and the sidewalls of cylindrical NWs. We have then explained how the pinning of the droplets at the NW edge can account for a large variation of the observed contact angle from the equilibrium condition at a flat surface. Finally, we have proposed that the finite-size nature of the edges may also explain part of the variability in available contact angles.

Experimental results: indium droplets on InAs NWs

We turn now to the experimental investigation of liquid droplets on NW tips. We consider the system formed by an In droplet on an InAs NW. The InAs NWs were obtained in a catalyst-free manner by self-assembly on a GaAs(111) B substrates as in [24].

These NWs typically exhibit a flat tip. By annealing the NWs in vacuum after growth at 530 °C it is possible to incongruently evaporate the arsenic from the NW tip, forming a pure In droplet. The experiments show that, with increasing the annealing time, the droplets increase their volume and move from the NW tip to the side facets, wetting simultaneously two {110} facets. In a related publication, we have shown that these droplets can be further used to nucleate the growth of InAs in a second step in the form of branches perpendicular to the direction of the primary NW [24, 42].

Here, we analyze the evolution of the shape and stability of the droplets as a function of their volume, gauged by the annealing time. Spherical cap droplet shapes have been treated previously [26, 32]. To the best of our knowledge, the transition of the droplets to lower energy shapes and/or the evolution of TPL pinning and depinning have not been analyzed for pure Indium wetting InAs NWs.

Figures 5(a)–(e) shows the SEM of the InAs NW tips for five different annealing times: 3, 5, 7, 10 and 15 min. Here we consider the evolution of the droplets *ex situ*. Even if previous studies show that this is a reasonable assumption [43], we still remind the reader that contact angle values may be affected from the modification of the environment. We observe three different configurations of the droplets: at the tip, transitioning to the side facet and on the side facets. For the three observed configurations, we have measured the apparent contact angle, defined by the angle between the apparent L–S interface and the droplet tangent at the TPL. A histogram depicting the distribution of contact angles obtained for the different annealing times is shown in figure 5(f). The reported values have been determined using the Carl Zeiss Microscopy, LLC—AxioVision Software. The measurements are affected by both picture resolution uncertainty and human mistake. A statistics of the uncertainty performed on different SEM pictures show that the statistical variation of the measurement ranges from $\pm 3^\circ$ to $\pm 8^\circ$, depending on the resolution of the picture. After 3 min of annealing, some InAs NWs have small In droplets on their top surface. The measured apparent angle is 43° on average. This is consistent with the known equilibrium contact angle of indium droplet on (111)B InAs (i.e. determined by the Young–Dupré equation). As annealing proceeds and the droplet volume increases, the liquid spreads to the edges of the NW tip. As soon as the droplet pins at the edge, the angle increases. At 5 and 7 min, the average apparent angle is respectively 100° and 115° . We note that the angle distribution has become significantly broader, from few degrees to few tens of degrees. After 7 min annealing, the liquid droplets begin to relocate from the NW tip to the sides. We find an intermediate configuration in which the droplet is in the transition from the tip to the side

facet, which we denominated as half-way configuration. Clearly, in this case, the liquid–solid interface has been tilted. The fraction of droplets on the side facets increases with time and reaches a yield of 100% after 15 min. The distribution of the contact angle on the NW side facets is also quite broad. Half-way droplets have an even wider range of apparent angles. We believe this range results from uncertainty in the surface inclination, but also from the variation in the pinning at the sharp edge as it will be further elucidated here below. In figure 5(f), the graphic insets represent the three observed droplet configurations. The contact geometry is illustrated assuming that the NW is cylindrical, although it is known that (111)B InAs NW cross-sections are hexagonal [14, 44].

We turn now to the analysis of the droplets in the half-way configuration. In particular, we look at the shape of the liquid–solid interface. The indium droplet was removed by immersing the NWs for 10 min in isopropyl alcohol (IPA). Figure 6 shows representative SEM images of the tip of these NWs after removal of the droplet. This sample corresponds to the NWs annealed for 7 min. Numerous NWs terminated with truncated facets were observed. These truncated facets have 2 main inclinations with respect to the top surface; 67° and 52° . These facet inclinations would coincide respectively with the orientation of (111) and (311) surfaces. The formation of these slanted facets has been previously predicted for both self-catalyzed and gold-assisted III–V NWs growth techniques [3, 25, 32]. Their presence was also predicted by molecular dynamics simulations on the equilibrium of liquid–solid interfaces for VLS growth of NWs [45].

The presence of two preferential inclinations translate also in the observation of two preferential apparent angles. As shown in figure 5(f) the most probable apparent angles are 100° for smaller (5 min annealing) and 115° for larger droplets (7 min annealing). Smaller droplets tend to be located on the lowest inclination (52°) surface; while for larger droplets, the TPL line intersects the surfaces with inclination 67° , on their way to wet the vertical NW side facets. We thus propose that in the transition of the droplet from the NW tip to the side facets, the NW edge disappears to form new slanted facets with rising inclination when the volume increases. This observation confirms the non-static nature of the NW edges and the interaction/exchange of the material with the droplet. These results highlight that measuring the apparent contact angle and analyzing it with the Young–Dupré equation can lead to a misinterpretation. This is particularly evident in cases where the TPL contacts a surface with rapidly varying inclination. As opposed to the Young contact angle, the apparent angle of droplets on NW tips is measured with respect to the ideally perfectly horizontal top facet of the NWs. It is clear that the apparent angle is not necessarily related to the surface energy of the top facet of the NWs. As a consequence, relating the apparent angle to the Young–Dupré equation should necessarily lead to the misinterpretation of the energetics of the system (i.e. incorrectly assuming that neighboring facets have the same energy or that the apparent angle is not measured with respect to the correct surface).

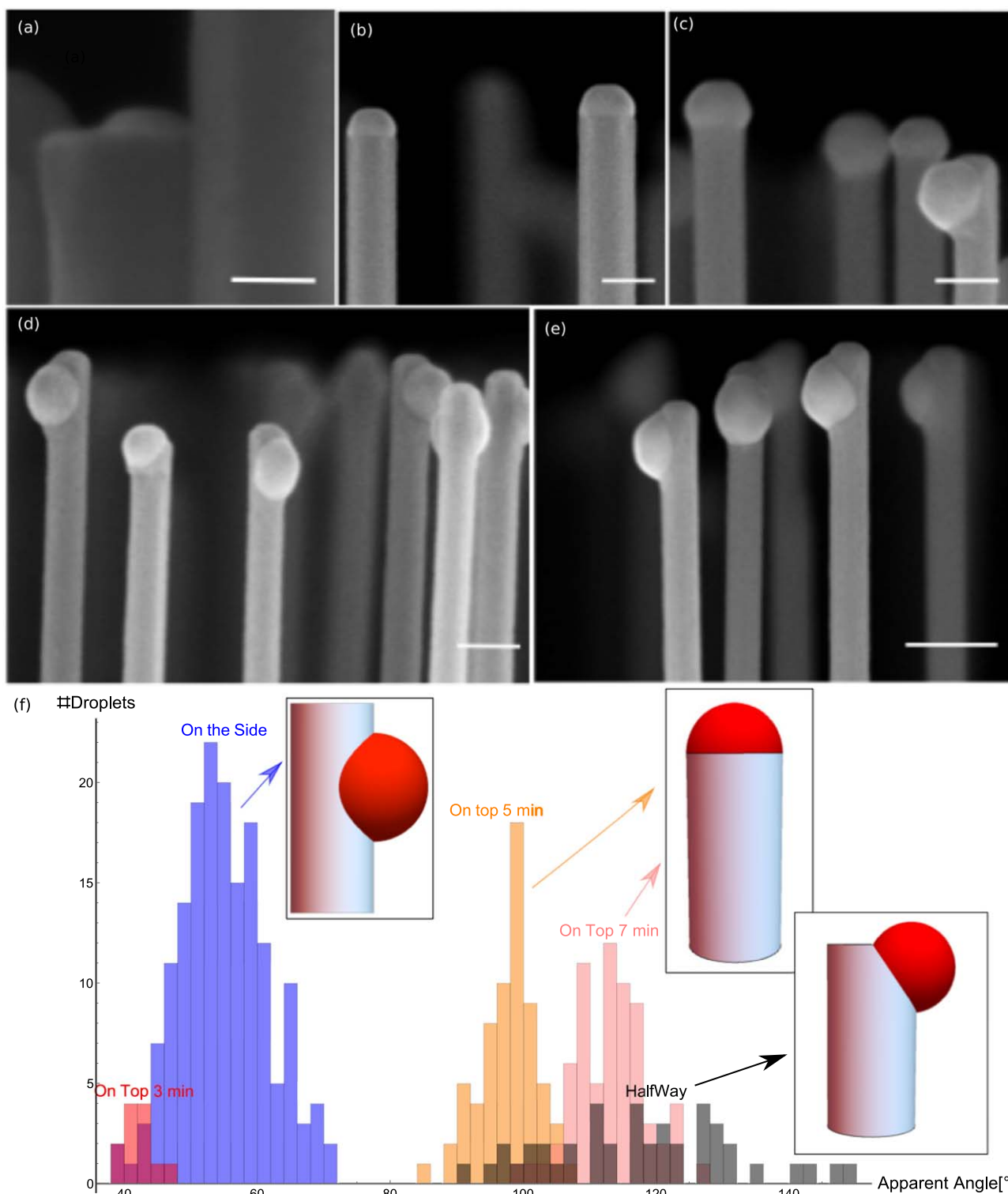


Figure 5. Stability of the In droplets on top of InAs NWs. (a)–(e) Scanning electron micrographs of the InAs NW tips after the annealing process. The annealing times were (a) 3 min, (b) 5 min, (c) 7 min, (d) 10 min and (e) 15 min. The scale bars represent 20 nm in (a) and 100 nm for the other images. (f) Distribution of the apparent angles for different annealing times and for the three different configurations: top of the NW, on the side facets and half-way. These configurations are shown schematically in the respective insets. The values of apparent angle of half-way (black) and side (blue) positioned droplets obtained with 7, 10 and 15 min annealing are similarly scattered and plotted together. The apparent angle of the liquid droplet on the top of the NW increases with increasing annealing time, and thus with the In volume. The annealing process introduces new facets onto the previously flat liquid–vapor interface.

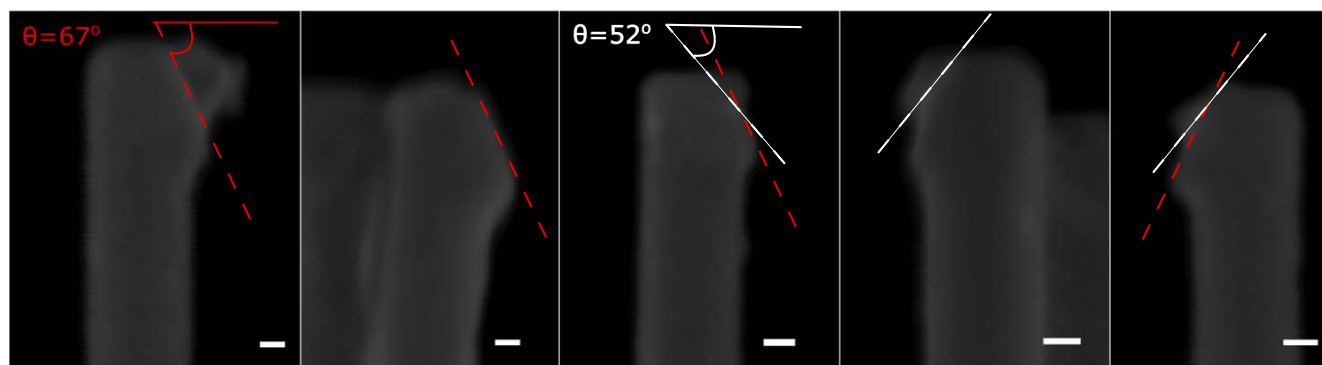


Figure 6. SEM pictures of the tip of InAs NWs grown on GaAs(111)B after a 7 min annealing procedure and removal of the Indium droplets. The inclinations of the slanted facets formed during arsenic evaporation are shown are of 67° and 52° for red and white dashed lines respectively. The scale bars correspond to 20 nm.

Conclusions

In conclusion, we have performed numerical simulations to show that the stability and morphology of a liquid droplet on a NW tip depend on three main factors: its volume relative to the dimensions of a NW, the presence of slanted facets and the equilibrium contact angle. As volume increases, the droplet is pinned by the NW edges that separate the NW side surfaces from its top surfaces. The apparent contact angle increases with the droplet volume up to a critical volume, after which the TPL unpins from the edges to relocate on the side of the NW. Our simulations are supported with experimental observations for indium droplets on InAs NWs. Finally, we also experimentally present the formation of slanted facets in the transition from the NW tip to the side facets and discuss their implications on contact angle measurements and interpretation.

Acknowledgments

Authors thank funding from SNSF via project nr 200021_169908, IZLRZ2_163861 and the NCCR QSIT, as well as H2020 program through project Indeed and Limquet.

ORCID iDs

Anna Fontcuberta i Morral  <https://orcid.org/0000-0002-5070-2196>

References

- [1] Ionescu A M and Riel H 2011 *Nature* **479** 329
- [2] Cartwright J 2011 *Nature News* **2011** 274
- [3] Krogstrup P, Jørgensen H I, Heiss M, Demichel O, Holm J V, Aagesen M, Nygård J and Fontcuberta i Morral A 2013 *Nat. Photon.* **7** 306
- [4] Dimroth F and Kurtz S 2007 *MRS Bull.* **32** 230
- [5] Plissard S *et al* 2013 *Nat. Nanotechnol.* **8** 859
- [6] Kammhuber J *et al* 2017 *Nat. Commun.* **8** 478
- [7] Alicea J, Oreg Y, Refael G, von Oppen F and Fisher M P A 2011 *Nat. Phys.* **7** 412
- [8] Kim W, Dubrovskii V G, Vukajlovic-Plestina J, Tütüncüoglu G, Francaviglia L, Güniat L, Potts H, Friedl M, Leran J-B and Morral A F i 2018 *Nano Lett.* **18** 49–57
- [9] Mårtensson T, Carlberg P, Borgström M, Montelius L, Seifert W and Samuelson L 2004 *Nano Lett.* **4** 699
- [10] Pierret A, Hocevar M, Diedenhofen S L, Algra R E, Vlieg E, Timmering E C, Verschuuren M A, Immink G W G, Verheijen M A and Bakkers E P A M 2010 *Nanotechnology* **21** 065305
- [11] Wu Z H, Mei X Y, Kim D, Blumin M and Ruda H E 2002 *Appl. Phys. Lett.* **81** 5177
- [12] Zamani M *et al* 2018 *Nanoscale* **10** 17080
- [13] Fonseka H A, Caroff P, Wong-Leung J, Ameruddin A S, Tan H H and Jagadish C 2014 *ACS Nano* **8** 6945
- [14] Koblmüller G, Hertenberger S, Vizbaras K, Bichler M, Bao F, Zhang J-P and Abstreiter G 2010 *Nanotechnology* **21** 365602
- [15] Jabeen F, Grillo V, Rubini S and Martelli F 2008 *Nanotechnology* **19** 275711
- [16] Koivusalo E, Hakkarainen T and Guina M 2017 *Nanoscale Res. Lett.* **12** 192
- [17] Givargizov E I 1975 *J. Cryst. Growth* **31** 20
- [18] Yazawa M, Koguchi M, Muto A, Ozawa M and Hiruma K 1992 *Appl. Phys. Lett.* **61** 2051
- [19] Glas F, Harmand J-C and Patriarche G 2007 *Phys. Rev. Lett.* **99** 146101
- [20] Wagner R S and Ellis W C 1964 *Appl. Phys. Lett.* **4** 89
- [21] Binkerd E F and Kolaril O E 1975 *Pergamon Press* **13** 655–61
- [22] Matteini F, Tütüncüoglu G, Potts H, Jabeen F and Fontcuberta i Morral A 2015 *Cryst. Growth Des.* **15** 3105
- [23] Yuan X, Caroff P, Wong-Leung J, Fu L, Tan H H and Jagadish C 2015 *Adv. Mater.* **27** 6096–103
- [24] Potts H, Morgan N P, Tütüncüoglu G, Friedl M and Fontcuberta i Morral A 2017 *Nanotechnology* **28** 054001
- [25] Jacobsson D, Panciera F, Tersoff J, Reuter M C, Lehmann S, Hofmann S, Dick K A and Ross F M 2016 *Nature* **531** 317
- [26] Tornberg M, Dick K A and Lehmann S 2017 *J. Phys. Chem. C* **121** 21678
- [27] O'Dowd B J *et al* 2014 *J. Appl. Phys.* **116** 063509
- [28] Schmidt V, Wittemann J V, Senz S and Gösele U 2009 *Adv. Mater.* **21** 2681
- [29] Krogstrup P, Curiotto S, Johnson E, Aagesen M, Nygård J and Chatain D 2011 *Phys. Rev. Lett.* **106** 125505
- [30] Kolibal M, Vystavěl T, Varga P and Šikola T 2014 *Nano Lett.* **14** 1756
- [31] Nebol'sin V A and Shchetinin A A 2003 *Inorg. Mater.* **39** 899
- [32] Dubrovskii V G 2017 *Crys. Growth Des.* **17** 2544–8

- [33] Zannier V, Ercolani D, Gomes U P, David J, Gemmi M, Dubrovskii V G and Sorba L 2016 *Nano Lett.* **16** 7183
- [34] Fang G and Amirfazli A 2012 *Langmuir* **28** 9421
- [35] Carter W 1988 *Acta Metall.* **36** 2283
- [36] Brakke K A 1992 *Exp. Math.* **1** 141
- [37] Heiss M *et al* 2013 *Nat. Mater.* **12** 439
- [38] Steinke L, Cantwell P, Stach E, Schuh D, Fontcuberta i Morral A, Bichler M, Abstreiter G and Grayson M 2013 *Phys. Rev. B* **87** 165428
- [39] Young T 1805 *Phil. Trans. R. Soc.* **95** 6
- [40] Saiz E, Tomsia A P and Cannon R M 1998 *Acta Mater.* **7** 2349
- [41] Cassie A B D and Baxter S 1944 *Trans. Faraday Soc.* **40** 546
- [42] Koivusalo E S, Hakkarainen T V, Galeti H V A, Gobato Y G, Dubrovskii V G and Guina M D 2017 *Nano Lett.* **17** 5350–5
- [43] Yuan X, Caroff P, Wong Leung J, Fu L, Tan H H and Jagadish C 2015 *Adv. Mater.* **27** 6096
- [44] Johansson J, Karlsson L S, Svensson C P T, Mårtensson T, Wacaser B A, Deppert K, Samuelson L and Seifert W 2006 *Nat. Mater.* **5** 574
- [45] Frolov T, Carter W C and Asta M 2014 *Nano Lett.* **14** 3577

4.2 The configuration of the droplet in a situation out of equilibrium

In the previous section we analysed the volume-induced transition between the two stable configurations of liquid droplets wetting cylindrical pillars: the top and the side locations. Nevertheless, from both theoretical predictions and experimental observations we identify an intermediate droplet shape, depicted in inset a) of Fig. 4.1. By testing this configuration through Surface Evolver simulations, performed with parameters in agreement with the previous section, the outcomes show a peculiar behaviour related to an unstable system. This instability can be observed due to the movement of the center of mass of the droplet during the iterations. The movement of the droplet is the result of unbalanced forces, meaning that the droplet enters into dynamic mode to reduce its own energy. The presence of an unbalanced condition is visible also by observing the computed shape of the droplet reported in inset a) of Fig. 4.1, which clearly wets the top and the side facets of the cylindrical pillar differently even though the wetting angles have been set at the same value of 43° . To visualize numerically this instability, we report in Fig. 4.1 b) the calculated mean curvature of the triangles composing the droplet surface as a function of their position along the x-axes. A variation of the mean curvature of the facets is observed as a function of their position, in particular its value increases going towards the side of the cylinder.

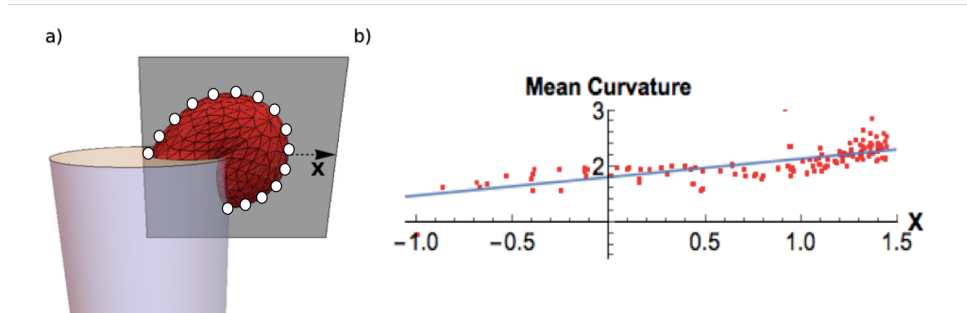


Figure 4.1 – a) Sketch of the droplet's edge configuration on top of an ideal cylinder b) Calculated mean curvature of the facets (white dots) composing the mesh of the droplet represented in inset a) as a function of their position along the x-axes.

According to Laplace's law, the mean curvature of a spherical droplet is proportional to its partial pressure or its stability with respect to the environment. As expected from the energy minimization principle, lower pressures are preferred to higher ones. This gradient in the mean curvatures is the origin of the displacement of the droplet towards the region where its mean curvature can be minor, that is to say towards the top part of the cylinder. This would impede the fall of the droplet to the side facets of the cylinder. The same behavior has been observed also for very small droplet, proving that we are not dealing here with a volume-induced instability. To understand the origin of this instability we should remind that this kind of motion is frequently observable in droplets wetting surfaces composed by different materials, thus creating a gradient in the surface energy which will translate into a

gradient in the wetting angle of the droplet along its perimeter. This same phenomenon is at the base of selective area epitaxy itself. In general, anytime a droplet is subjected to a distortion from its ideal spherical cap configuration and it is not constrained, it starts a motion with the target to rearrange its disposition. In our simulations we have the same wetting angle between the top and the sidewalls, thus the motion of the droplet cannot be related to a gradient in the surface energies of the system. What is changing in our system is the shape of the solid underneath, which goes from a flat surface (on the top of the cylinder) to a rounded one (on the sidewalls). Thanks to these computational results we suggest that liquid dynamics and asymmetric wetting behaviour can be induced by creating dishomogeneity in the curvature of the wetted surface, while keeping the same material. This phenomenon can be applied in many fields of surface science and technology, allowing to create selectivity without the need to add additional materials to the system. To conclude this section, we would like to highlight that for droplet wetting the edge of a cylinder there may exist a combination of contact angles on the top and side of the cylinder that allows the droplet to have constant mean curvature along its whole surface area. In this case, the difference in the wetting angles between the top and the side gets compensated by the different curvatures of the surface. However, the analysis of this case is not treated here.

4.3 Liquid stability on top of multi-material pillars

The growth via VLS approach combined with a geometrical constraint of the droplet in preferential configurations can ensure the fabrication of ordered arrays of NWs. The efficiency of constraining droplets through selective area to obtain ordered arrays has been proved.[112] In this case, a thin mask layer of silicon oxide is modified through lithography and preferential wetting sites are created. In this section we analyse the complementary situation, in which the preferential sites are created on top of silicon pillars surrounded by the non-wetting material mask.[114] The main characteristic of this approach is that the droplet is free to develop its vapor-liquid interface without any interference. The only constraint of the liquid is the contact area with the top part of the pillar, whose structure, composition and size can be controlled through microfabrication techniques. The selectivity in wetting solely the top part of the pillar is ensured by the presence of the non-wetting material all around the silicon pillar, except for the top part. In order to compare the effect of this additional layer of oxide covering the sidewalls of the cylinder, we computed the surface energy of the system as a function of the droplet volume for droplet configurations on the side and on the top. The energy values are normalized by the droplet volume and the difference in the interfacial energies. The characteristic wetting angle for the droplet on the side is 116° (wetting Ga-SiO₂) while on the top it is 51° . In Fig. 4.2, we report the plot of the computed system surface energy for the two configurations considered: the top and the side, depicted in the lateral insets. From these results, we can clearly notice an absence of crossing between the two configurations, meaning that in the range of volumes considered there is no transition allowed from the top to the side of the cylinder. This effect is due to an even lower stability of the side configuration caused by

the presence of the higher wetting angle in addition to the already curved surface destabilizing the droplet, as explained in section (3.2). We can already conclude that the localization of the droplet on the pillar and its coercion on the top can be obtained by adding a layer of low wetting material all around the sidewalls of the pillar. In the rest of this chapter we will show how the thickness of this external layer, combined with the variation of the droplet's volume, can give rise to the same pinning effect introduced in section (2.6) and discussed in section (3.1). This system can thus allow the manipulation of the wetting behaviour of the catalyzing droplet for increasing the range of NW's growth possibilities.

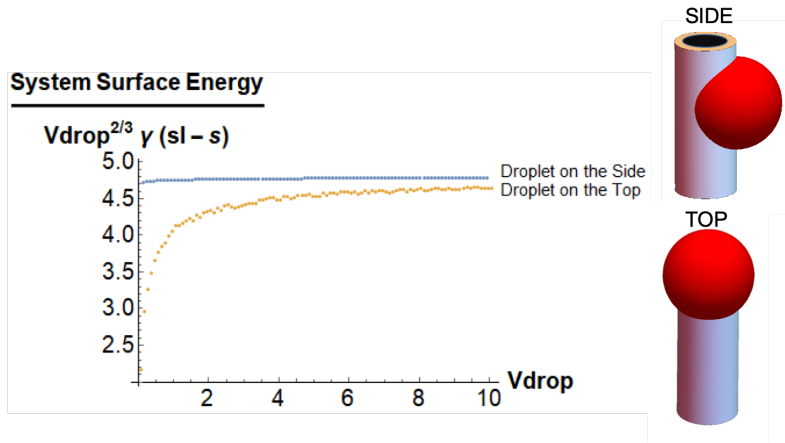


Figure 4.2 – Computed surface energies of the system as a function of the droplet volume for droplet's configuration on the side and on the top. The energy value are normalized by the droplet volume and the difference in the interfacial energies. The characteristic wetting angle for the droplet on the side is 116° (wetting Ga-SiO₂) while on the top it is 51° (wetting Ga-Si). The radius of the core is 0.5, covered by a 0.1 thickness layer of oxide.

Silicon pillars are prepared through selective etching of Si (111) substrates followed by a thermal oxidation of the lateral surface and decapping of the top oxide. This process ensure the realization of a platform for engineering the wetting behavior of metallic sessile droplets while continuing to prepare NWs through selective area epitaxy. The samples have pillars with different diameters and different thicknesses of the oxide. Gallium droplets are deposited inside the MBE system; the size distribution of the droplets can be increased by increasing the deposition time even if the upper limit is linked to the size of the pillars. Through the software Surface Evolver, we computed the equilibrium shape of the liquid and verified the development of the surface energy of the system as a function of the volume. The simulations have been performed for different combinations of pillar's diameters and oxide thicknesses in order to follow the experimental setup. Since the pinning effect of the droplet for NW's growth is interesting for its influence on the wetting angle of the droplet, we decided to compute and plot the variation of the droplet's apparent angle as a function of the droplet's volume.

Firstly, we consider the case in which the external radius of the pillar is fixed while the inner region (the low wetting angle part) varies. This situation can be related to experiments where the oxidation time of the Silicon pillar is changed. In particular the smaller the inner region

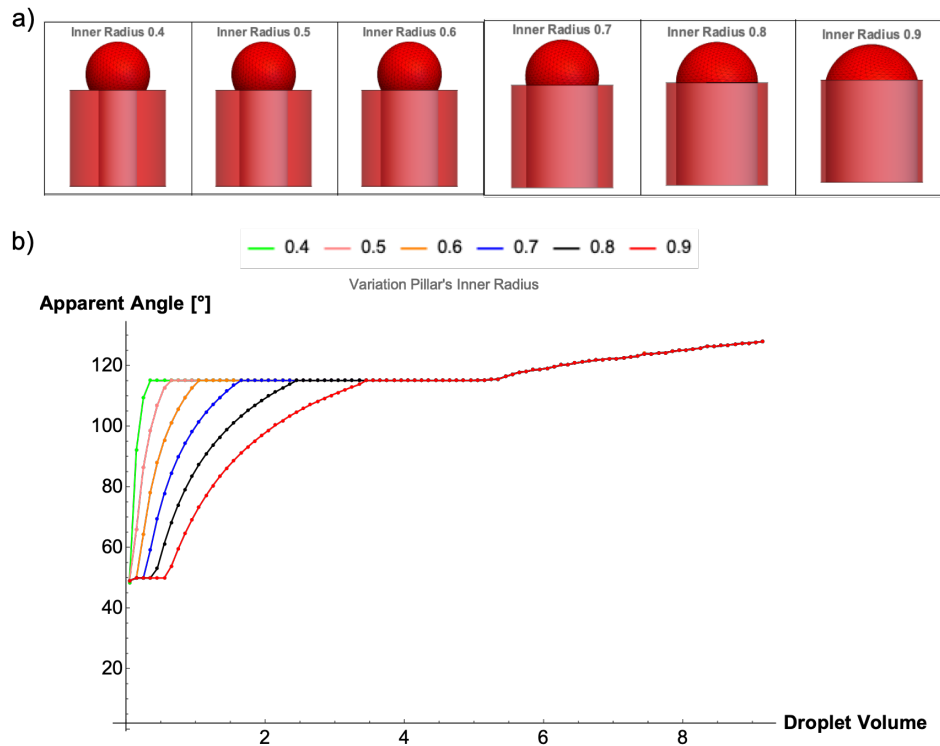


Figure 4.3 – (a) Sketches of the pillars analysed and the resulting equilibrium shape of the sessile droplet on top, taken with the same volume of 0.7 in all insets (b) Surface Evolver simulations on the variation of droplet's apparent angle as a function of the droplet's volume. The pillar system is built as a double cylinder characterized by 2 parameters: inner radius and external radius, defining the Silicon core and the external lateral SiO₂ coverage respectively. The difference in materials between the 2 regions is computed by using different wetting angles: 51° and 116° for wetting on Si and SiO₂ respectively. Note how the modification of the internal radius, while maintaining fixed the external radius, causes a modification in the rate with which the apparent angle modifies with the droplet's volume. The fixed external radius ensure that the "Second Pinning" threshold and development remains the same in all cases analyzed.

is, the longer is the oxidation time. The sketches related to the cases analysed, ordered for increasing inner region size (reducing oxidation time), are depicted in Fig. 4.3 (a). In Fig. 4.3 (b) we plot the development of the apparent angle as a function of the droplet volume for pillars having different inner radius. Already from the images it is possible to appreciate a clear variation of the pinning angle as a function of the inner region size at fixed droplet's volume. In particular, the droplet reduces its apparent angle for larger inner region, due to the larger area available for the droplet to spread spontaneously without suffering the constraining. From the data reported in Fig. 4.3 (b) we can see that the different inner radius of the pillars can provoke a wide range of apparent angles mostly for small droplet volumes. In the first region of the plot we can indeed recognize a different curve for each different pillar, meaning that the rate with which the pinning effect modifies the droplet's characteristics varies according to the value of the inner radius. In particular the rate of apparent angle variation, i.e. the slope of the curve, reduces for increasing inner region size. From this result we can conclude that for smaller pillars a precise control and the engineering of the apparent angle results more difficult than for larger pillars. From an analytical point of view, the size of the inner radius and the wetting angle value of the inner region define the volume of the droplet at which the pinning effect starts. Indeed once the characteristics of the system are defined it is always possible to calculate the critical volume (1), after which the droplet separates from its natural wetting behaviour. The larger the inner radius is, the larger is the critical volume for the pinning effect to start. The larger is the volume of a droplet, the larger is the variation of the volume necessary to appreciate a modification in its apparent angle due to the constraining. As expected by the presence of a high wetting angle region outside of the inner part of the pillar, all the curves saturate at the value of 116° at different critical volume (2). Smaller droplets saturate to this value faster than the larger ones. Once reached the apparent angle which equalize the Young's angle available on the second region, the droplet is left free to enlarge as a function of the volume without restrictions, while maintaining the same wetting angle. The apparent angle saturation region, visible as a plateau in the plot, indicates the range of volumes in which the droplet is not under pinning effect anymore. Due to the fixed value of the outer radius, that is to say the end of the pillar, the different pillars share the value of the critical volume(3) of 5.75 for the beginning of the second stage of the pinning of the droplet. Having the same critical volume makes the rate of apparent angle variation the same for all the pillars considered. Since the second pinning initial apparent angle, fixed at 116° , is already quite large, as well as the volume droplet, the slope of the curve has a much smaller coefficient with respect to the first pinning regime.

Secondly, we analyse the situation in which we fix the inner radius of the droplet and we vary the outer radius. The sketches showing the pillars analysed and the relative equilibrium shapes of the droplet constrained on the top are presented in Fig. 4.4 (a). In Fig. 4.4 (b) we plot the development of the apparent angle as a function of the droplet volume for pillars with different outer radius. From the droplet shapes, selected with all the same volumes equal to 5, we can appreciate a variation in the wetting properties as a function of the outer radius. Again, the apparent angle reduces for increased outer radius size, because for larger outer

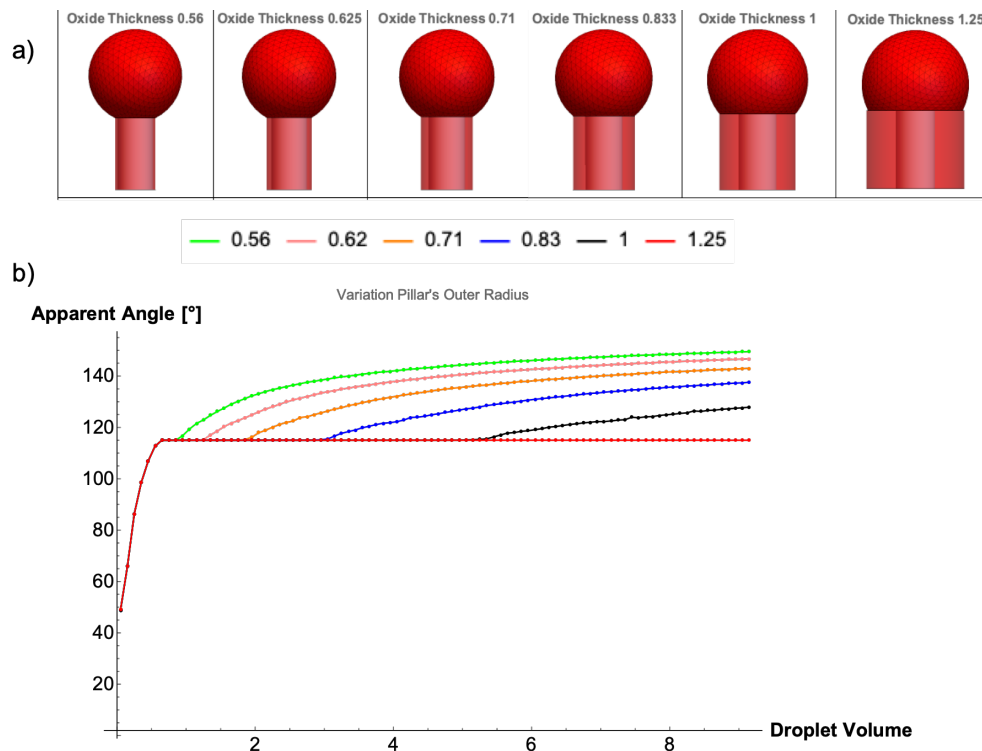


Figure 4.4 – (a) Sketches of the pillars analysed and the resulting equilibrium shape of the sessile droplet on top, taken with the same volume of 5 in all insets (b) Surface Evolver simulations on the variation of droplet's apparent angle as a function of the droplet's volume. The pillar system is built as a double cylinder characterized by 2 parameters: inner radius and external radius, defining the Silicon core and the external lateral SiO₂ coverage respectively. The difference in materials between the 2 regions is computed by using different wetting angles: 51° and 116° for wetting on Si and SiO₂ respectively. Note how the modification of the external radius, while maintaining fixed the inner radius, causes a shifting in the «second pinning» volume threshold.

radius there is a larger area available for the droplet to spread freely without being forced to pin. By analysing the development of the apparent angle as a function of the droplet's volume reported in Fig. 4.4 (b) we can appreciate the complementarity of this system with respect to the case presented before in Fig. 4.3 (b). The presence of a fixed inner radius and a fixed wetting angle on the inner region, namely 51°, unify the different pillars under the same critical volume(1) for the onset of the first pinning effect. Same critical volume for all pillars result in the same rate of apparent angle variation for all the curves, that's why for small volume of the droplet the plot is reduced to a single curve. The same rate of apparent angle variation result also in the same critical volume (2), at which we have the saturation to the apparent angle of 116° happening for all pillars at the same value of 0.4. After this critical volume, the wetting behaviour of the droplet start to differentiate according to the characteristics of the pillar they are wetting. Different size of the outer radius causes the variation of the critical volume (3) for the onset of the second pinning, the one caused by the confinement created by

the sidewalls of the cylinder. Pillars having shorter outer radius begin the second pinning at smaller volumes and they also offer larger apparent angle at any droplet's volume. From this part we can conclude that by modifying the outer radius of the pillar, which experimentally corresponds to change the thickness of the non-wetting layer surrounding the Silicon pillar, is possible to engineer the wetting behaviour of large droplets and obtain a fine tuning of the apparent angle for apparent angle larger than the contact angle of the outer region material.

Finally we treat also a more comprehensive case in which we analyse both inner and outer radius while maintaining the outer/inner ratio equal to 0.8. The main differences among different pillars are shown in panel (a) of Fig. 4.5, while the development of the apparent angle of the droplet for each case is reported in the plot shown in inset (b). All the pillars have different inner and outer radius, thus the critical volumes defining the beginning of the first pinning regime (1), its end (2) and the beginning of the second pinning regime (3) are all different. In this kind of system it is possible to observe the highest dispersion in the observed apparent angles for each droplet's volume considered: by varying the inner radius, small droplets get pinned differently while by varying the outer radius, the large droplets get constrained at different volumes.

For summarizing this section, the pinning effect at the interface of different materials and the pinning effect at the edge of the pillar can both be used to engineer the apparent wetting angle of droplets constrained on top of pillars. In Fig. 4.6 there are the main conclusions regarding the range of volumes controllable by the different configurations. The localization of the droplet is ensured by choosing a low wetting material (higher wetting angle) for surrounding the pillar. By playing with the relative size of inner radius, outer radius and droplet's volume it is possible to obtain a wide range of apparent angles.

From an experimental point of view, the realization and the analysis of the development of the wetting angle as a function of the diameter of Silicon pillars ranging from 35 to 270 nm in diameter has been performed by a colleague. The pillars have been fabricated through etching processes, oxidized, and loaded in the MBE (molecular beam epitaxy) chamber, where Gallium was deposited for 10 min under an ultrahigh vacuum.[114] In Fig. 4.7 (a) there are the SEM images, representative of the configurations obtained and the plot of the measured Gallium wetting angle as a function of the pillar diameter. For smaller pillars, the wetting angle reduces for increasing pillar's diameter. For higher diameter pillars, the wetting angle remain constant for increasing pillar's diameter, meaning that the regime of free wetting of liquid Ga on Si has been reached. By increasing the Gallium predeposition time, it is possible to shift the beginning of the plateau in the wetting angle, allowing a larger range of wetting angle tunability. Fig. 4.7 (b) (c) and (d) show the vertical nanostructures obtained in the range of contact angles marked in gray. The SEM pictures confirm the presence of a Ga droplet at the top, which confirms that they grow by the self-catalyzed VLS mechanism. These structures have been grown using a Ga predeposition step of 10 min, a Ga equivalent flux of 0.14×10^{-6} Torr, and a V/III ratio of 12. Fig. 4.7 indicates the yield as a function of the pillar diameter. The maximum yield achieved is 10% for 35 nm diameter pillars. The other pillars contain [111]B-

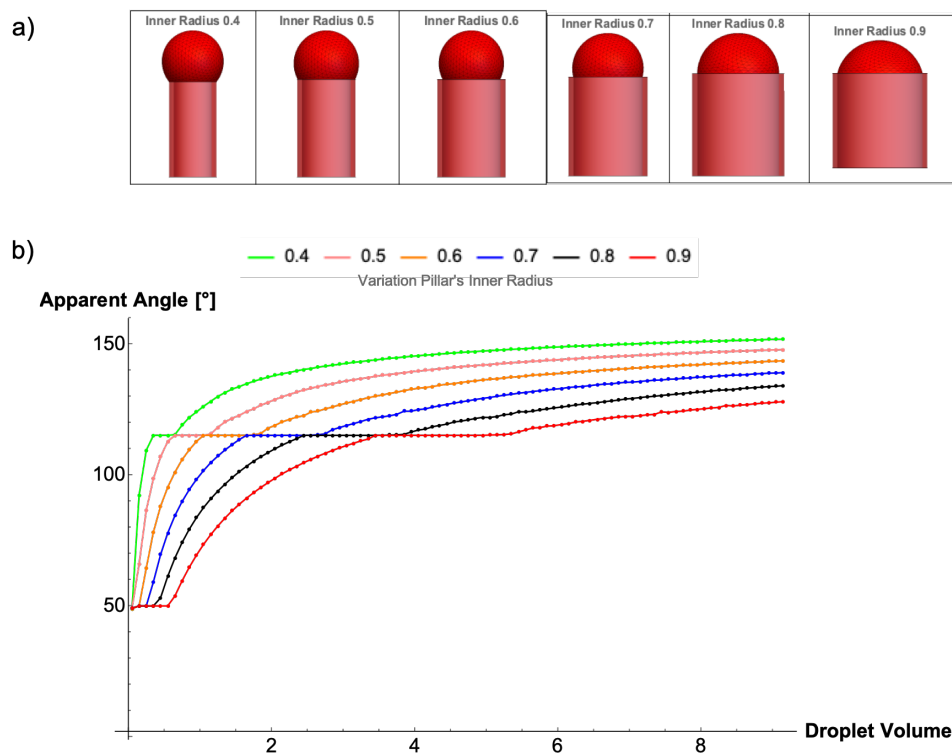


Figure 4.5 – (a) Sketches of the pillars analysed and the resulting equilibrium shape of the sessile droplet on top, taken with the same volume in all insets (b) Surface Evolver simulations on the variation of droplet's apparent angle as a function of the droplet's volume. The pillar system is built as a double cylinder characterized by 2 parameters: inner radius and external radius, defining the Silicon core and the external lateral SiO₂ coverage respectively. The difference in materials between the 2 regions is computed by using different wetting angles: 51° and 116° for wetting on Si and SiO₂ respectively. Note how the modification of the internal radius, cause the modification in the rate with which the apparent angle modifies with the droplet's volume. Modifying the outer radius as well, by keeping the ratio between the two equal to 0.8, causes the shifting in the «second pinning» volume threshold and a modification in the slope as well.

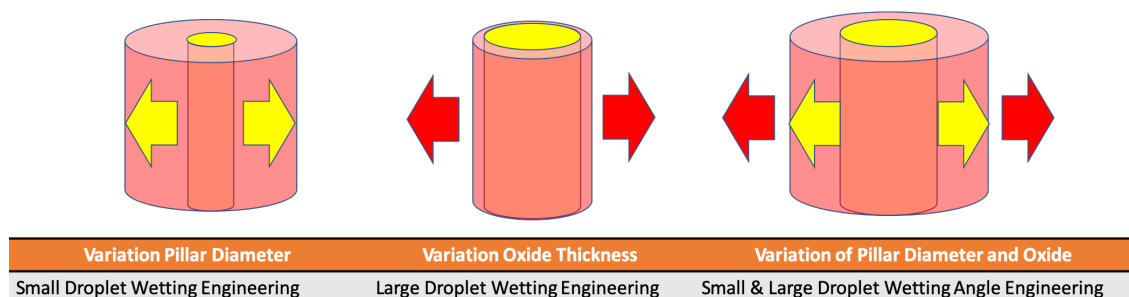


Figure 4.6 – Summary of the main regimes and configurations analyzed in this section

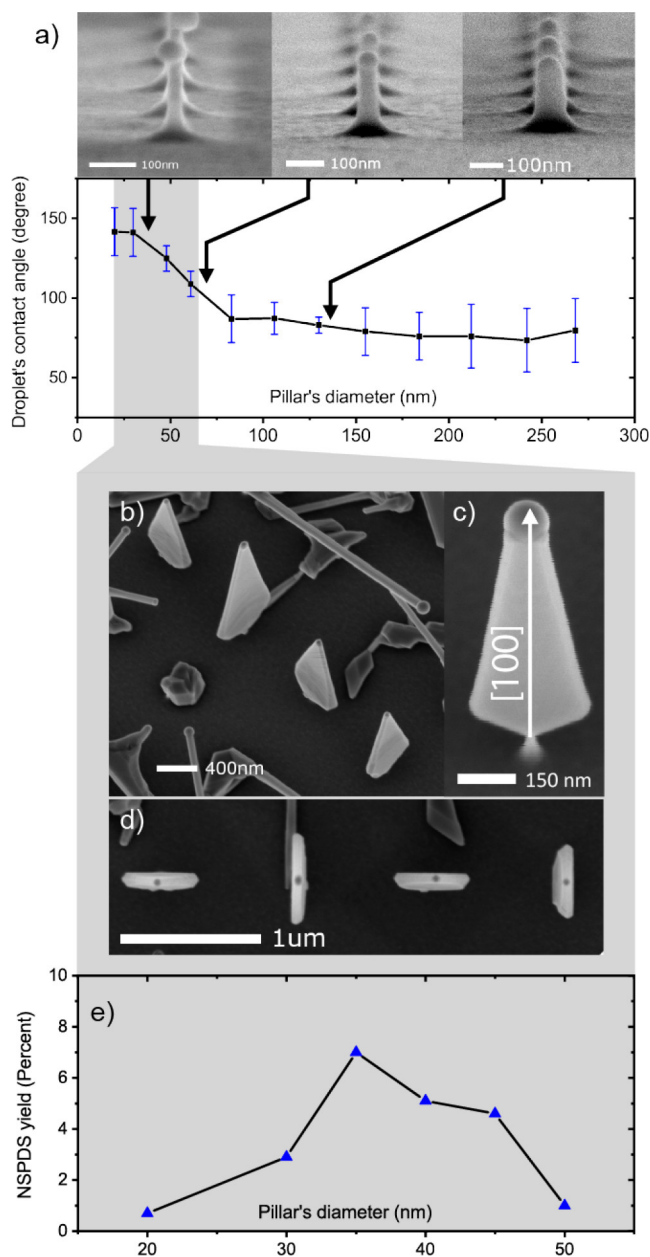


Figure 4.7 – (a) Table showing the relation between Si pillars' diameter and the Ga droplets' contact angle, along with SEM images representing certain diameters. (b, c, and d) SEM pictures of GaAs nanopads on Si pillars and their growth range in the table. (e) Relation between the yield of nanopads (NSPDs) and pillar diameter for a 20 nm (nominal) oxide mask. Copyright from ACS[114], further permissions related to the material excerpted should be directed to the ACS.

oriented GaAs NWs and parasitic growth. The yield drastically decreases for pillars larger than 50 nm, plummeting to a value of 1%. The low yield in smaller pillars can be explained by the Ga droplet falling down the side and, in larger pillars, by the energy of formation of the initial seed, as explained further below. [114]

4.4 Asymmetry in the droplet's wetting

Through the characterization of real systems, we observed an unexpected discontinuity in the wetting angle along the TPL of Gallium droplets wetting the top facet of Silicon pillars having cylindrical geometry and oxidized sidewalls. In Fig. 4.8, the SEM pictures shows the measurement of the wetting angle on different side of the droplet. For each droplet, when one side has apparent angle higher than 90° the other side present apparent angles lower than 90° . This asymmetry is the result of a process of compensation, caused by the fact that the droplet is leaving the ideal condition of morphology associated with an ideal spherical cap.

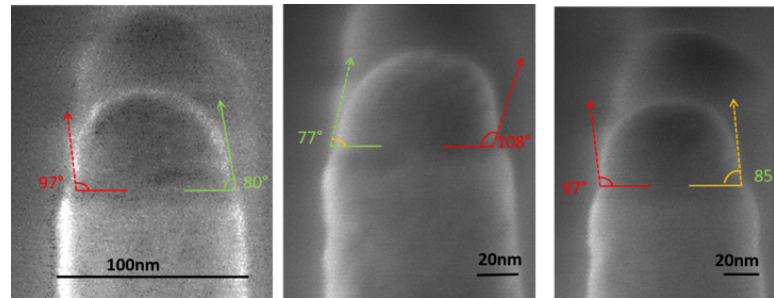


Figure 4.8 – SEM images of Gallium droplets wetting the top facet of Silicon cylindrical pillars having oxidized sidewalls.

In the hypothesis that the pillars have an ideally symmetric shape with sidewalls vertically aligned along the whole perimeter, such discontinuity could be attributed to the presence of local chemical and/or geometrical defects on the top surface. Such defects can locally modify the contact angle and, when sufficiently pronounced, the droplet cannot move even if capillary forces are applied to it. This phenomenon can happen during the motion from a hydrophobic to a hydrophilic substrate or during the rearrangement of the droplet's shape due to an increase of its volume, as introduced in section (3.2). Nevertheless, depending on the relative position of the defect, the droplet usually prefers to deviate its motion and slide around the side of the defect. For liquid wetting limited regions, the process of pinning at surface defects become particularly relevant especially for large droplet volume. In these situations, the droplet does not have the freedom to deviate its motion or simply to rearrange its shape to minimize the surface energy. In our system, we combine the interplay between a hydrophobic and a hydrophilic surfaces, the silicon oxide and the silicon part respectively, together with the restriction of the available area for wetting. In such conditions, in presence of defects having size in the range of the droplet's perimeter, we assume that the pinning at the defect contributes to the modification of the droplet's shape, resulting into the observation of

different apparent angle at different sides of the droplet, (as shown in Fig. 4.8).

In order to verify the lost in symmetry of the spherical cap defining the equilibrium shape of the wetting droplet, we decided to compute with Surface Evolver what happens to the liquid morphology once the wetting does not occur symmetrically. Always analysing the system of oxidized Silicon pillars, we study the situation in which one side of the droplet remains attached to the Si-SiO₂ interface while the other one can already start to spread onto the high-wetting angle surface. This configuration is available at the droplet just after the second critical volume, at which the droplet is allowed to surpass the 2-materials interface. In Fig. 4.9, we show the development of the normalized surface energy of the system (a) and the variation of the apparent angle (b) as a function of the droplet volume for the two configuration considered: the symmetric and the asymmetric one. From Fig. 4.9, the partial attachment of the droplet's perimeter at the material interface result in a clear reduction of the system surface energy, meaning that this configuration is more stable than the one in which the whole perimeter moves right away on the high wetting-angle materials. The partial attachment allows the droplet to remain in contact with the region of the pillar where the wetting requires less energy, thus stabilizing the whole system even though the shape of the droplets lose its shape as a spherical cap.

This result implies that the asymmetric spread of the droplet from the 2-materials interface is a fundamental configuration of the droplet wetting behaviour, characterizing a whole range of droplet's volume. The critical volume at which the droplet goes back to a symmetrical wetting depends on the thickness of the oxide layer. Indeed the unilateral spreading on the oxide can proceed until the further pinning at the end of the pillars. Once the second pinning starts, the part of the droplet pinned at the 2-materials interface will be forced to move away and start its spread on the high-wetting angle material. In this way, even though the droplet goes back to a spherical cap shape, the surface energy of the system will start rising due to the spread on the non-wettable material. With respect to the results of the development of the apparent angle reported in Fig. 4.9 (b) we show the computation of the average apparent angle for the asymmetric configuration due to the dispersion of the wetting angle along the perimeter of the droplet. The mean wetting angle tends to increase smoothly with the volume of the droplet. With this partial spreading along the oxide the plateau associated with a sharp transition to the highly wettable surface disappears. This smooth transition, which removes the discontinuity point at the ends of the plateau, further indicates that the asymmetric configuration represent the most stable configuration for a droplet spreading away from a 2-materials interface.

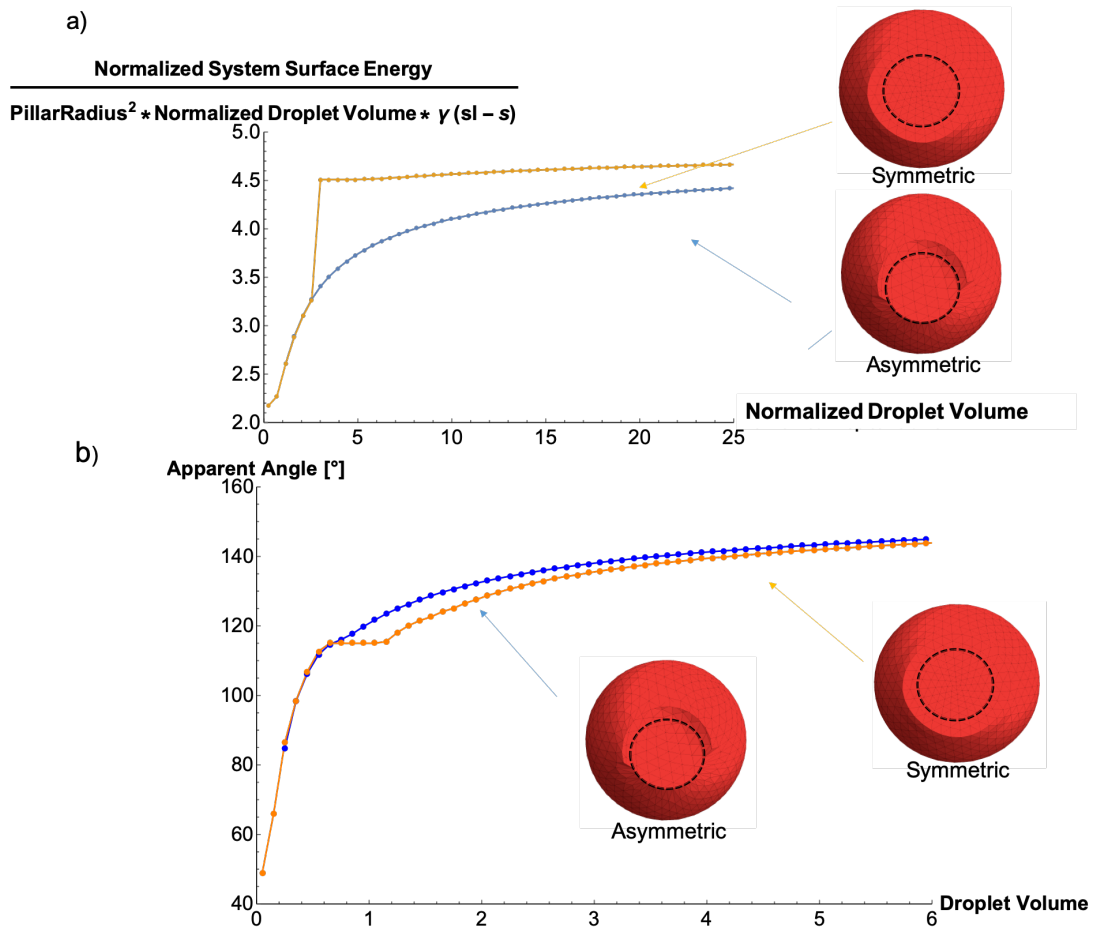


Figure 4.9 – Surface Evolver computation of the (a) variation of the system surface energy as a function of the droplet's volume normalized by the surface area of the pillar and the difference between the surface tension of the liquid-solid and solid-vapor interface. (b) Computation of the apparent angle of the droplets wetting the oxidized pillars symmetrically and asymmetrically. For the asymmetric configuration we report the mean apparent angle.

5 Wetting on top of non-cylindrical columns

NW properties and growth mechanisms are typically modelled by approximating their shape to a cylinder, in order to simplify the modelling. Nevertheless, the crystalline nature of NWs translates into the appearance of preferential surfaces and crystallographic planes, selected according to the growth direction and the crystal phase they have.[115, 116] Such surfaces can be predicted considering the thermodynamic stability of the system: according to the chemical environment there is a combination of crystal planes which minimizes the surface energy of the fixed volume crystal. III-V material based NWs are typically surrounded by facets belonging to the $\{110\}$ or $\{112\}$ family, which result to be the most stable crystallographic planes available around the typical kinetically active direction $[111]$, representing the growth front. Due to the hexagonal symmetry of the system the NWs exhibit hexagonal cross section, with 6 facets visible also through SEM characterization, as for the NWs shown in section 3.1. Experimental evidences report that NW's cross sections can also eventually differ from the hexagonal shape, with also triangular and squared geometries beyond the more typical hexagonal one.

In this chapter we analyse the physics of sessile droplets wetting faceted NWs, from the point of view of both system surface energy and the droplet morphology deformation. The droplet deformation is linked to the dispersion of the apparent wetting angle which follows the symmetry imposed by the geometrical constraint. In the first section we show the effects of the modification of the geometry of the spatial constraint of the wetting plane on the droplet stability and morphology. In the following section we include a submitted paper, where the experimental observation of a system combining droplet deformation and transitional geometrical constraints for the creation of II-V superlattice NWs. The contribution of the author have been the analysis of the growth mechanism and the computation of the system surface energy.

5.1 Geometric influence on the droplet wetting stability and apparent angle dispersion

Single crystal NW used as building blocks for optoelectronic applications often show a cross section differing from the cylindrical approximation. In this section we apply Surface Evolver to the analysis of sessile droplets wetting the top facet of columns having different cross-sectional geometries, such as the hexagonal, the squared and triangular ones. We compare them with the results obtained for the ideal case of wetting a cylindrical column.

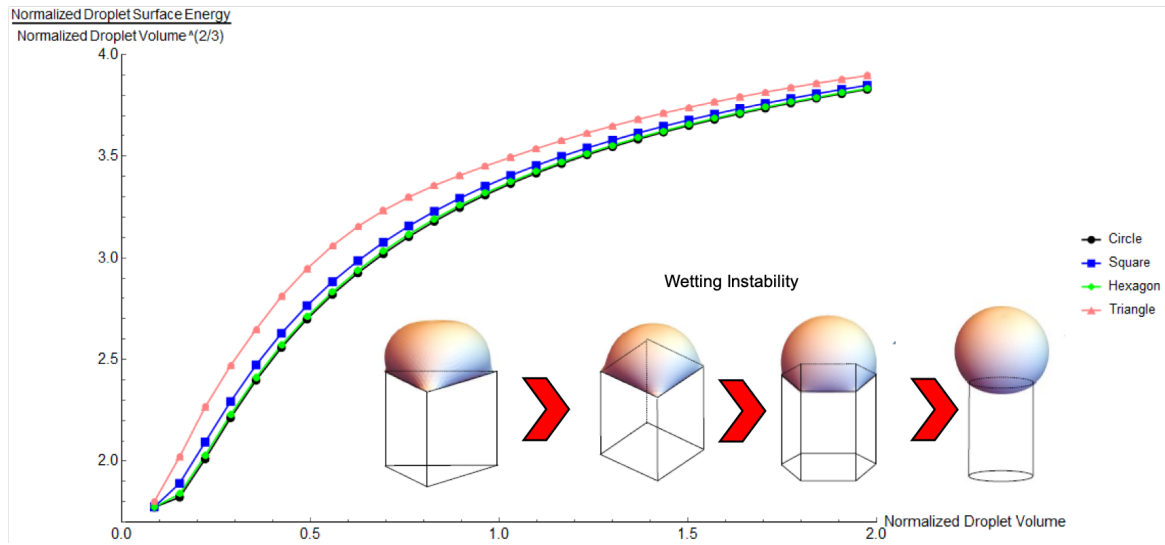


Figure 5.1 – Computed development of the normalized surface energy of the system composed by a sessile droplet wetting planes characterized by 4 different geometries: triangular, squared, hexagonal and circular (as depicted in the insets)

In Fig. 5.1 we show the comparison among the normalized surface energy of sessile droplets wetting different planes, having a limited and predefined geometrical shape, as depicted in the insets at the bottom of the figure. The normalized surface energy is the surface energy of the system divided by the difference between the solid-liquid and the solid interfacial energies, and by the surface area of the finite plane considered. The normalized droplet volume is the droplet volume divided by the surface area of the plane elevated to the power $2/3$. The wetting angle used in the simulations for characterizing the solid-liquid interfacial energy is fixed at 43° . The droplet perimeter is not pinned at the edge of the plane: it is free to wet the anywhere on the plane within the limit of the plane itself. From the comparison among the obtained results, the most stable configuration is the one associated to the wetting on top of the circular constraint. The less stable configuration is the one with droplet constrained onto a triangular plane. From these initial results we can conclude that the farther the geometrical constraint of the wetted plane goes away from a circle, the less stable the droplet configuration becomes. This behaviour is linked to the fact that ideal morphology of a free wetting droplet is a spherical cap. The spherical cap holds minimum surface energy contribution, characterized by the Young's contact angle. Droplets wetting limited and not-circular planes need to distance

from their ideal morphology, causing an increase in the total surface energy of the system. Among the different cross sections considered, the surface energy relative to the hexagonal is the closest to the circular case, thus showing that, at least from a system surface energy point of view, the approximation of a circular cross-section does not differ too much from the experimental case used in sect 3.1. Thus the approximation is reasonable. By reducing the number of facets composing the sidewalls of the NW, the surface energy of the system increases.

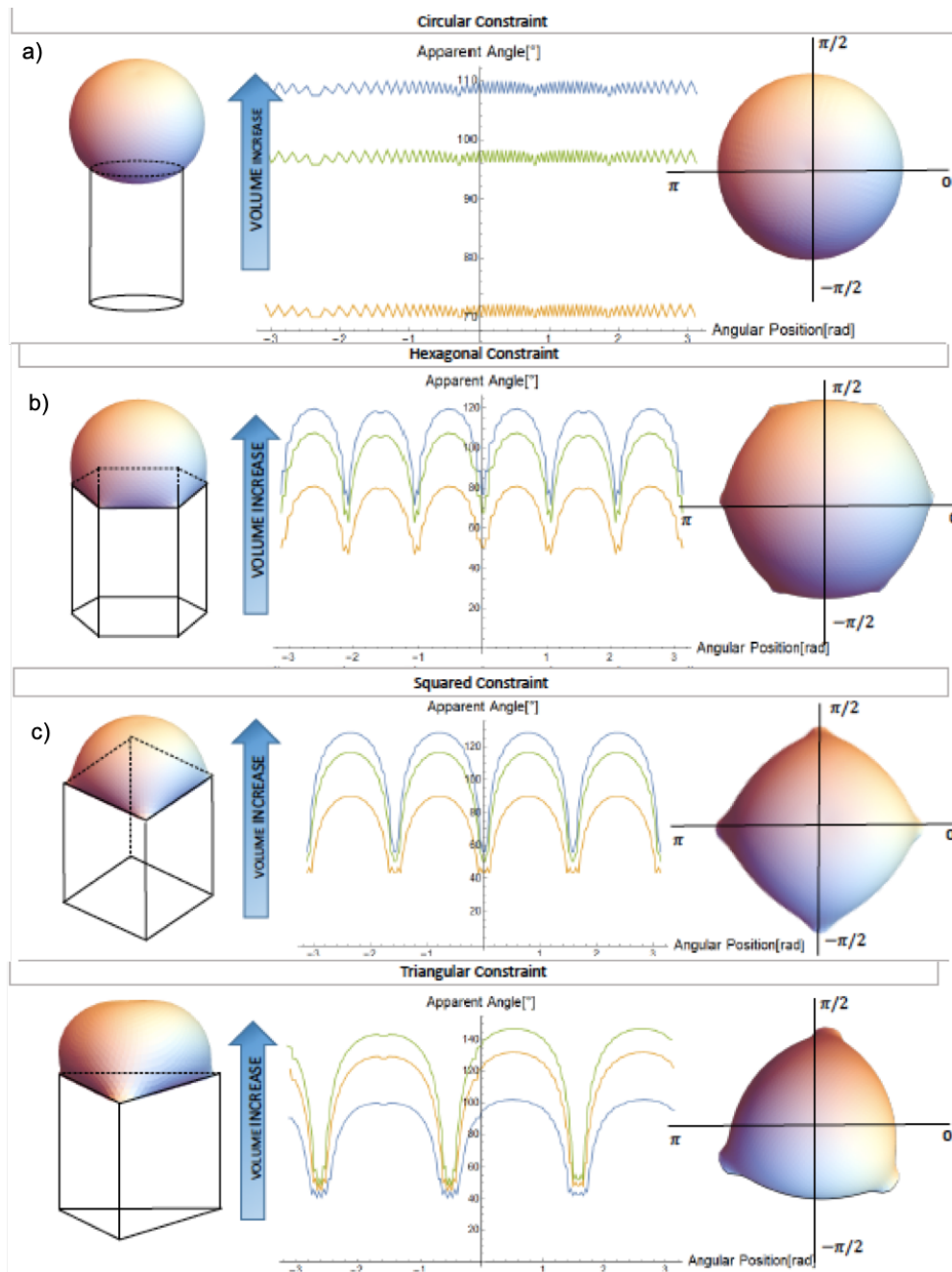


Figure 5.2 – Sketches of the systems analysed, apparent angle dependency along the perimeter of the droplet for 3 referential volumes (small, medium and large) and top view of the computed equilibrium morphology for different symmetry of the spatial confinement: circular (a), hexagonal (b), squared (c) and triangular (d).

The deformation of the droplet due to the removal of the circular symmetry is illustrated more representatively by the images presented in the right column of Fig. 5.2, showing the computed equilibrium shapes of droplets wetting hexagonal (b), squared (c) and triangular (d) finite

planes. For a more quantitative analysis of the deformation, we show in the central part of Fig. 5.2 the computation of the dispersion of the apparent angle along the perimeter (or TPL) of the droplet for the different cross sections considered. The apparent angle is determined, for each facet composing the perimeter of the droplet, through the software Surface Evolver by measuring the angle between the normal direction of the wetted plane and the normal direction of each facet. The apparent angle dispersion, for each configuration, is shown for 3 different droplet's volumes, namely the small (orange), medium (green) and large (blue). The first column of the figure helps to clarify the geometry of each system considered, by showing the side view of the droplet's mesh wetting a sketch of the hypothetical NW defining the plane's geometry. We now focus on the apparent wetting angle. In panel (a) of Fig. 5.2, where the circular constraint is shown, we can appreciate the uniformity of the wetting angle for each fixed volume. As already explained in sect. 3.1 the increase in the droplet's volume causes the increase in the value of the apparent angle due to the pinning effect, but it does not alter its uniformity along the perimeter. The uniformity in the apparent angle manifests itself in the circular symmetry characterizing the top view of the droplet's equilibrium morphology, shown in the column in the right. From panel (b) we can note the break of the circular symmetry on the wetting behaviour of the droplet due to the hexagonal geometry of the contact plane. The apparent angle oscillates along the perimeter following the 6-fold symmetry of the constraint, with amplitude of the oscillations determined by the droplet's volume together with the pinning effect. The oscillations in the apparent angle are the quantitative translation of the periodic deformation caused by the presence of sides and corners along the edge of the plane. Indeed for non-radially symmetric constraint, the pinning effect is not uniform, but it happens as a function of the position along the side of the edge (same for each side due to the 6-fold symmetry). The pinning effect is zero at corners while it reaches its maximum at the center of the side. This behaviour is caused by the droplet tendency to keep a spherical cap morphology which results into a dewetting of the corners (lower angle) compensated by an accumulation of volume at the sides (higher angle). This situation is visible also from the last column of panel (b), where six small tails can be recognized in correspondence of corners's localization. Panel (c) shows the results of the apparent angle oscillations onto a squared constraint, which follow the 4-fold symmetry given by the system. The disposition of the tails breaking the circularity in the top view of the computed equilibrium shape follows the imposed geometrical constraint as well. As last case analyzed, in panel (d) we show the results for the triangular constraint, where the apparent angle development as a function of the TPL's position oscillates recreating the 3-fold symmetry. Both the amplitude in the angle and the visibility of the deformation of the mesh appear to be of a much higher amplitude in this last case with respect to the previous ones.

In order to quantify the amplitude of the oscillations, we plot the dispersion of the wetting angle, defined as the difference between the maximum apparent angle value and the minimum value allowed to the droplet. In Fig. 5.3 we compare the dispersion on top of hexagon, square and triangle for 3 fixed referential volumes (small =1, medium= 2 and large= 3). The results show that the dispersion in the apparent angle increases for geometrical constraints

distancing from the circular symmetry; this same tendency reminds the results shown in Fig. 5.1 while considering the droplet's instability. The dispersion increases linearly also with the volume due to the pinning effect. From these results we can conclude that droplet's deformation, observable in the dishomogeneity of the apparent angle, appears together with droplet instability and may be related. In particular, the dispersion in the apparent angle along the perimeter of a constrained droplet increases with the increase in the droplet volume and with the lowering of the symmetry of the spatial confinement.

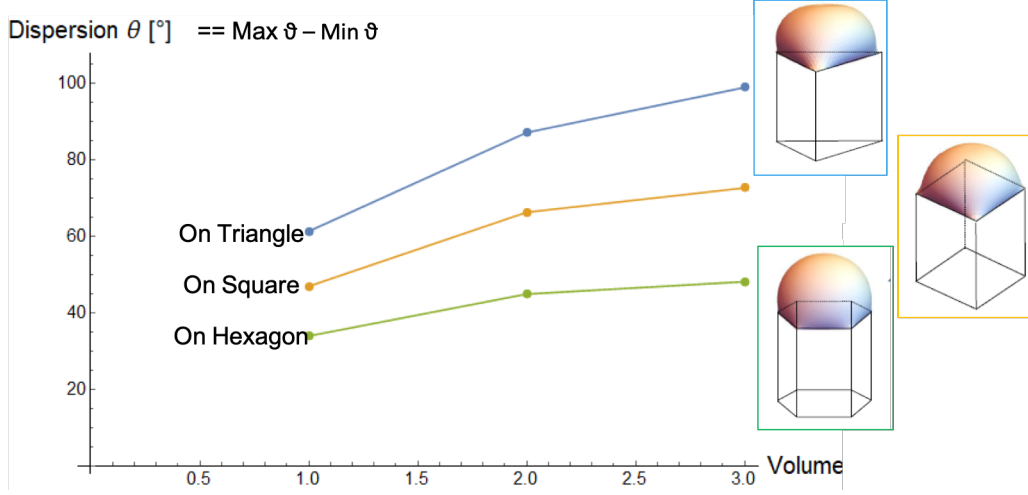


Figure 5.3 – Computation of the dispersion in the apparent angle of the droplet for wetting happening on the 3 low symmetry spatial confinement considered: hexagonal, squared and triangular. 3 referential volumes have been considered in order to take note of the pinning effect.

5.2 The role of liquid surface energy in the growth of NWs with a varying cross-section: the case of zig zag NWs

In this section we report an experimental evidence of a natural system taking advantage of droplet's deformation and transitional geometrical constraints to create innovative nanostructures, such as II-V zig zag NWs. These systems have a zig zag shape and their cross section periodically varies from an hexagonal shape to a triangular one. For understanding the growth mechanism of these NWs we computed the surface energy of the system composed by a droplet wetting different constraints, gradually shifting from a triangular geometry to an hexagonal one and back. This transition in the geometrical constraint has been built to recreate the transition in the cross section of the NW. According to the experimental observations, the insertion of a Indium-based heterotwin encompasses the zig to zag transtion. An heterotwin is a twin defect, typically merging 2 crystals with different orientation, composed by an element which differs from the elements composing the crystals. In our hypothesis the energy necessary for the heterotwin formation is provided also by the deformation energy stored in the droplet due to the unstable condition. Our hypothesis is verified by analysing the

effect of the droplet volume modification of the heterotwin insertion periodicity: for larger volume the deformation rate as a function of the spatial constraint reduces. When the deformation rate reduces it takes longer for the system to accumulate the necessary deformation energy for the heterotwin insertion, explaining why the interdistance of heterotwin is larger at the base of the NW, where the diameter is larger than at the end due to the tapering of the tip.

ARTICLE

Heterotwin Zn_3P_2 superlattice nanowires: the role of indium insertion in the superlattice formation mechanism and their optical properties

Received 00th January 20xx,
Accepted 00th January 20xx

DOI: 10.1039/x0xx00000x

Simon Escobar Steinvall,^{†a} Lea Ghisalberti,^{†a} Reza R. Zamani,^{†b} Nicolas Tappy,^a Fredrik S. Hage,^{c,d} Elias Stutz,^a Mahdi Zamani,^a Rajrupa Paul,^a Jean-Baptiste Leran,^a Quentin Ramasse,^{c,e} W. Craig Carter,^{a,f} Anna Fontcuberta i Morral^{a,g,*}

Zinc phosphide (Zn_3P_2) nanowires constitute prospective building blocks for next generation solar cells due to the combination of suitable optoelectronic properties and an abundance of the constituting elements in the Earth's crust. The generation of periodic superstructures along the nanowire axis could provide an additional mechanism to tune their functional properties. Here we present the vapour-liquid-solid growth of zinc phosphide superlattices driven by periodic heterotwins. This uncommon planar defect involves the exchange of Zn by In at the twinning boundary. We find that the zigzag superlattice formation is driven by reduction of the total surface energy of the liquid droplet. The chemical variation across the heterotwin does not affect the homogeneity of the optical properties, as measured by cathodoluminescence. The basic understanding provided here brings new perspectives on the use of II-V semiconductors in nanowire technology.

Introduction

Filamentary crystals, also known as nanowires, have provided additional design freedom in the elaboration of materials with desirable properties.^{1–4} This arises from the possibility of engineering the crystal phase, material composition, and for the possibility of expanding the structure in three dimensions.^{3,5,6} Among the design opportunities, the composition or structure of nanowires can be arranged periodically in the form of superlattices.^{6–9} The periodicity of the superstructure modulates both the electronic and phonon (vibrational) states, depending on the magnitude of the period.^{10–13} Semiconductor superlattices find applications in the optoelectronic and thermoelectric arena.^{14–17} In thin films, the materials combinations are mostly restrained due to lattice-mismatch and thermal expansion conditions. Superlattice nanowire structures circumvent these limitations, and have been

achieved by modulating the composition, crystal phase, and crystal orientation through rotational twins.^{5–8}

Twin superlattices (TSLs) in semiconductors were predicted by Ikonik *et al.* in 1993.¹⁸ More recently, they were implemented in nanowire form, first in Al_2O_3 and ZnSe , and subsequently in InP .^{19–21} These TSLs have been obtained mainly by the vapour-liquid-solid (VLS) method in which a nanoscale liquid droplet preferentially collects the growth precursors.²² In addition to a periodic arrangement of twins, these nanowire superlattices adopt a characteristic zigzag morphology with alternating (111)A/B facets in the case of zincblende nanowires.^{7,8} According to Algra *et al.*, twin formation is determined by energy minimisation involving the stability of the droplet and the surface energy of the facets as a function of their polarity –(111) a or B–.⁸

Zinc phosphide, Zn_3P_2 , has recently attracted attention as a compound semiconductor made of elements that are abundant in the Earth's crust with optoelectronic properties suitable for photovoltaic applications.^{23–28} Zn_3P_2 has been obtained both in the form of bulk crystals^{29,30}, thin films^{25,26,31}, and nanostructures^{9,24,32–34}. Zinc phosphide based solar cells with an efficiency of up to 6% have been reported.³⁰ This value is still well below the theoretical limit (>30%), illustrating the improvement potential of this material.^{35,36}

The synthesis of Zn_3P_2 nanowires can follow the VLS and the vapour-solid mechanisms, with In, Sn, and Au as catalysts.^{9,24,32–34,37,38} Zn_3P_2 nanowires adopt various morphologies depending on the fabrication method and/or growth conditions, including a zigzag superlattice.^{9,24,32–34} In contrast with III-V compound semiconductors, Zn_3P_2 exhibits a centrosymmetric tetragonal structure, and thus also non-polar facets and main crystal symmetry directions.²⁹ Consequently, all side facets of Zn_3P_2

^a Laboratory of Semiconductor Materials, Institute of Materials École Polytechnique Fédérale de Lausanne, 1015 Lausanne, Switzerland

^b Centre Interdisciplinaire de Microscopie Électronique, École Polytechnique Fédérale de Lausanne, 1015 Lausanne, Switzerland

^c SuperSTEM Laboratory, SciTech Daresbury Campus, Keckwick Lane, Warrington WA4AD, United Kingdom

^d Department of Materials, University of Oxford, Oxford, OX1 3PH, United Kingdom

^e School of Chemical and Process Engineering and School of Physics and Astronomy, University of Leeds, Leeds LS2 9JT, United Kingdom

^f Department of Materials Science and Engineering, Massachusetts Institute of Technology, Cambridge, Massachusetts 02139, United States of America

^g Institute of Physics, École Polytechnique Fédérale de Lausanne, 1015 Lausanne, Switzerland

[†] Equal Contributions.

* E-mail: anna.fontcuberta-morral@epfl.ch

Electronic Supplementary Information (ESI) available: [details of any supplementary information available should be included here]. See DOI: 10.1039/x0xx00000x

zigzag nanowires are always Zn-terminated.^{27,33} This means that the mechanism through which Zn_3P_2 obtains a zigzag morphology is inconsistent with the model proposed based on III-Vs.⁸

In this paper we reveal the nature of the defects leading to the zigzag structure using aberration-corrected and analytical scanning transmission electron microscopy (STEM). In addition, we explain the formation mechanisms based on simulations of the surface energetics of the droplet as a function of the nanowire cross-section. Finally, we outline the consequences of this periodic structure for the optical functionality through cathodoluminescence spectroscopy (CL).

Experimental

The Zn_3P_2 nanowires were epitaxially grown in a Veeco GENxplor molecular beam epitaxy (MBE) system on InP (100) substrates. They were grown through In catalysed VLS, with the In originating from the substrate.²⁴ The analysed samples were grown at a manipulator temperature of 250°C and a V/II ratio of 1.15 or 1.45 for four hours, with additional details on the growth in [24]. The nanowires were transferred to copper TEM grids with holey carbon by scraping the grid on the growth substrate for TEM studies, and were used as grown for CL studies.

Scanning electron microscopy (SEM) images were acquired using a Zeiss Merlin FE-SEM equipped with a Gemini column. The operating conditions were an acceleration voltage of 3 kV and a beam current of 100 pA. An in-lens secondary electron detector was used for the imaging.

Droplet simulations were performed using the Surface Evolver software³⁹, which computes minimised surface energy by optimising shapes given constraints and wetting angles. We implement the interfacial energy of the liquid-solid interface by means of the Young's equation with a contact angle of 43° when the triple line is unconstrained. The vertical axis in Fig 2c is the total energy divided by L^2 , with L being the average length of the sides, and the difference between the solid-liquid and the solid surface tensions. The average length of the side remains constant with a value of 1.57. Regarding the geometrical constraint, the triple line is not pinned to the edge, but is left free to move inside the polygon. To build the polygon, centred at the origin, we define an equation for each side of the hexagon through the lat and shrink parameters, illustrated in the SI. While the lat parameter is fixed at 0.55 and defines the apothem of the reference hexagon, the shrink parameter is variable controlling the shape of the constraint since it represents the normal between the facet centroid and the selected facet. By varying the shrink parameter from -0.25 to 0.25, we can reproduce the evolution of the nanowire cross-section from left oriented triangle to right oriented triangle (HT1 & HT2), passing through the hexagonal geometry at shrink equal to 0. To compare the effect of the volume we performed the simulations for three different droplet volumes: 0.125, 0.225, and 0.325 with dimensions of L^3 .

Aberration-corrected bright-field/high-angle annular dark-field (BF/HAADF) STEM images and electron energy loss spectroscopy (EELS) maps were collected on a STEM-dedicated

Nion microscope (US100MC) operating at 60 kV. The Nion UltraSTEM 100MC HERMES is equipped with a C5 Nion probe corrector (full correction up to 6-fold astigmatism C5, 6) and a UHV Gatan Enfium ERS spectrometer optimised for high energy resolution with high-stability electronics. The microscope is equipped with a cold-field emission gun (C-FEG), having an energy spread of 0.35 eV. The beam convergence semi-angle was 31.5 mrad and the EEL spectrometer entrance aperture semi-angle was 44 mrad. Image detector angles were 0-14 mrad (BF) and 100-230 mrad (HAADF). To minimise contamination, the specimens were baked prior to insertion at 130 °C in vacuum ($\sim 10^{-6}$ Torr), and the microscope column is maintained at ultrahigh vacuum (UHV). The denoising of STEM-EELS datasets was done using the MSA plugin for Gatan's Digital Micrograph suite, commercially available from HREM research.⁴⁰ Example spectra are shown in the SI, and the 443 eV and 1020 eV peaks were used for EEL mapping of In and Zn, respectively. Further imaging was also performed in a FEI Titan Themis 60-300 kV TEM operating at 200 or 300 kV. The machine is equipped with a field emission gun (X-FEG), a monochromators, two aberration correctors (one pre-specimen probe-corrector, and one post-specimen image corrector), and a Fischione HAADF detector. The collection angles are typically 85-200 mrad for HAADF-STEM images. The BF and HAADF images were denoised using radial a Wiener filter. Viewing direction illustrations were created in Mathematica.

An Attolight Rosa setup equipped with an Andor Newton 920 Si-CCD was used for CL measurements. It was operated at room temperature with an acceleration voltage of 3 kV, a beam current of <1 nA, and an exposure time of 50 ms per pixel. The nanowires were mounted on a stage with 20° tilt. Denoising of the hyperspectral maps was done through principal-component analysis (PCA) using the Hyperspy Software.⁴¹ Peak fitting was done after data treatment based on the approach described in ref. [42].

Results and Discussion

Electron Microscopy

Figure 1a shows a representative secondary electron SEM images of a typical zigzag Zn_3P_2 nanowire. These nanowires grow perpendicular to (101) with side facets belonging to {101}.^{24,33} While the lateral facets in III-V superlattices, (111)A and (111)B, can exhibit different polarities, this is not the case for Zn_3P_2 (101) facets as they are all Zn-terminated.^{7,8,27} The supposed difference between the lateral facets has been cited as one of the driving forces for the formation of TSL nanowires. This argument cannot be applied to this case as Zn_3P_2 does not display polar facets. Before discussing the mechanism, we disclose the nature of the interface dividing the zigzag regions in the nanowire.

Figure 1b shows an aberration-corrected BF-STEM image of a zigzag nanowire ([111] zone axis), revealing a "twin-like" planar defect separating different segments that are mirrored. This structural defect is akin to the twin planes in the III-V TSL

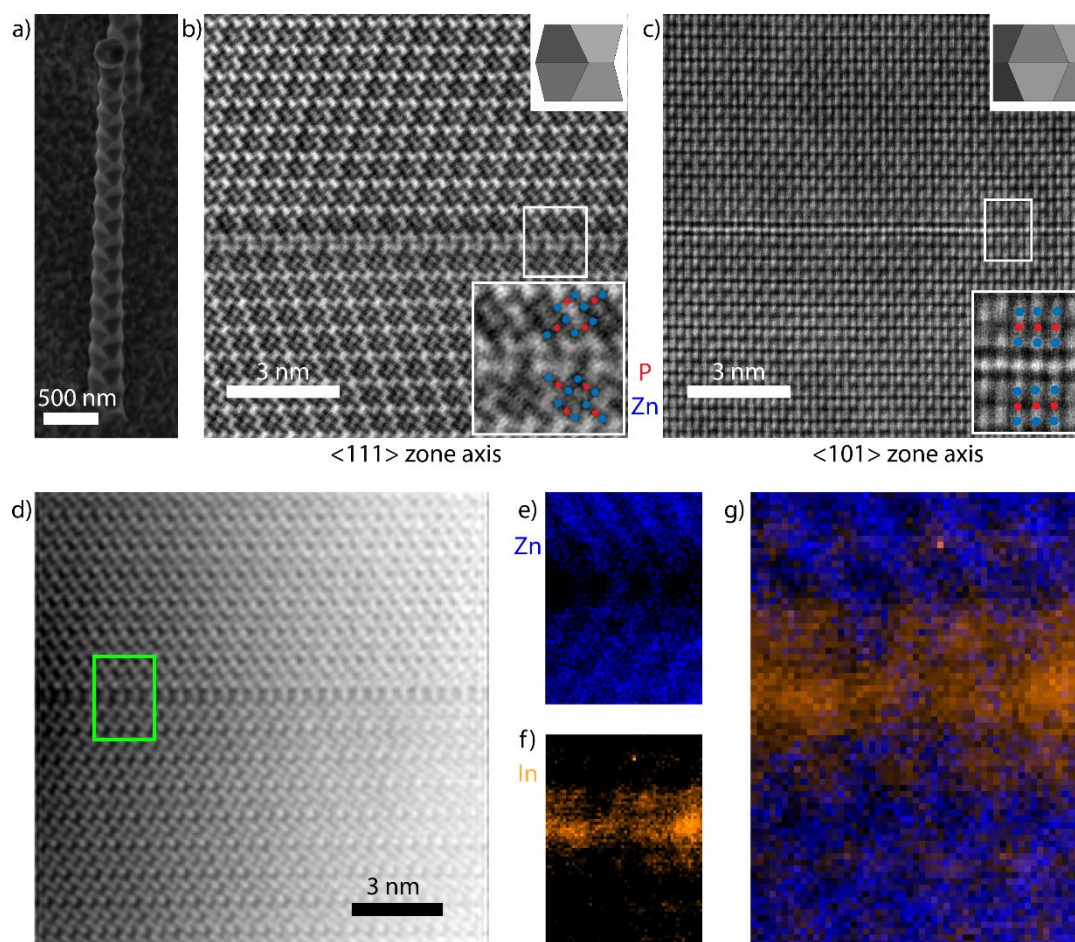


Figure 1. a) Secondary electron SEM image of a superlattice nanowire. b) Aberration corrected BF-STEM image taken along a $[111]$ zone axis in the region around the zigzag interface with an inset illustrating the viewing direction. c) Aberration corrected HAADF-STEM image taken along a $[101]$ zone axis in the region around the zigzag interface. The top inset illustrates the viewing direction and the bottom inset displays a “close up” on the interface. d) HAADF-STEM image ($[111]$ zone axis) of the region where the EELS maps were acquired (green). e–g) Core-loss EELS maps of Zn (blue – e), In (orange – f), and the combination (g), showing the localised presence of In in the region around the stacking fault.

nanowires: it interfaces two segments of the nanowire that appear to be rotated 180° around the nanowire growth axis – the (101) plane-, which is the most common twin plane in tetragonal systems.⁴³

Figure 1c shows the HAADF-STEM image of a region equivalent to that shown in Figure 1b, viewed along the other major zone axis, $[-101]$. The bottom insets corresponds to “close ups” of the interfaces, identifying sets of trimers (Zn – blue, P – red) at each side of the defect. The topmost insets show a three-dimensional model of the structure, highlighting the viewing direction of the respective zone axes. While the defect is easily discerned by the increase in intensity and break in periodicity in Figure 1c, the structure is not perfectly mirrored along this zone axis. Instead, we observe a translation of the top crystal by a (400) plane along the $\langle 100 \rangle$ direction perpendicular to the zone axis. Furthermore, as corroborated below, the interfacial defect extends to more than one monolayer, and is of a different composition than the neighbouring segments. Thus, the two rotated crystals are separated, not sharing any crystal lattice points, and consequently this defect cannot be considered a standard twin.

We not turn to the study of the nature of the interface separating the twinned regions by providing data on the

chemical composition. For this, we took the core-loss EELS of the “twin” and the adjacent regions –marked with a green square in Figure 1d, resulting in chemical maps with atomic-scale resolution.^{44,45} Figure 1e–g display the resulting chemical mapping of Zn (blue – e), In (orange – f), and combined (g). P mapping did not provide the same resolution, and a constant signal was observed throughout. The maps reveal the presence of In at the interface and the neighbouring layers, accompanied by a drop in the Zn content. The presence of In is consistent with the intensity analysis in the HAADF-STEM images, especially from the $[-101]$ direction (Figure 1c). The interface there appears slightly brighter than the rest, suggesting the presence of a heavier element, i.e. In. Given the chemical inhomogeneity across the boundary, the defect should rather be identified as a heterotwin.⁴⁶

The utilisation of a chemical heterogeneity at the boundaries or planar defects have been reported in Al/TiN composites and in doped II–VI compounds such as ZnO. In the case of Al, N-terminated TiN lowers the formation energy of twins, and they provide significantly improved mechanical properties.^{46,47} In ZnO, trivalent metals such as Al, Fe, Ga, or In have shown to precipitate at the interface of inversion domain boundaries.⁴⁸ The presence of trivalent metals in II–VI defects

modifies the bonding coordination from four in a tetrahedral fashion to eight in an octahedral one, causing the polarity inversion.^{49–52} However, in the case considered here the defect cannot be classified as an inversion domain boundary as there is no polarity inversion associated with it. In the following section we discuss the mechanism by which Zn_3P_2 forms a zigzag structure via a heterotwin.

Zigzag Mechanism

To investigate the driving forces prompting the regular insertion of heterotwins, we analysed the heterotwin periodicity along the nanowire length, x (nm), and as a function of W , an approximation of the cross-sectional apothem. The trend was observed in multiple nanowires, while the equation is based on the high-resolution TEM image shown in Figure S3. Similar to III-V TSL nanowires, the heterotwin periodicity in Zn_3P_2 nanowires depends on their diameter.^{7,53} The zigzag morphology results in the width being a periodic function with an amplitude with linear decay:

$$W(x) = \left(W_0 - \frac{W_0 - \frac{W_0}{2}}{2} - \frac{x}{\tan \frac{\pi}{2.02}} \right) \left(1 + \frac{1}{3} \cos \frac{2\pi x}{h_0 e^{-2 \times 10^{-5} x}} \right) \quad (1)$$

Where W_0 is the initial width and h_0 is the distance between the initial segment separation. Equation 1 shows that the heterotwin interdistance reduces with the reduction of the nanowire diameter, in agreement with studies on non-tapered superlattice ZnSe and GaAs nanowires.^{20,53} In particular, the term $\pi/2.02$ corresponds to 89° , i.e. the measured tapering angle characterising the reduction of the nanowire's diameter. The origin of the tapering is explored in detail in ref. [24].

Regarding possible explanations for the heterotwin formation mechanism, previous studies argued that twins in a zigzag structure form to minimise the nanowire surface energy.^{8,54} The argument is reasonable for compound semiconductor nanowires exhibiting facets with different polarities and thus different surface energies. However, Zn_3P_2 is not polar. The basic structural unit consists of symmetric Zn-P-Zn trimers, instead of asymmetric cation-anion dumbbells such as In-P in InP, and its centrosymmetric crystal structure.^{29,48,55} Thus, all facets in the zigzag structure are equivalent.²⁷ This means we cannot reasonably attribute the instigation of the Zn_3P_2 twinning process to nanowire surface energy minimisation alone. As discussed below, deformation of the liquid droplet during growth provides a more compelling argument.

We studied the droplet stability as a function of the volume and underlying cross-section of the nanowire, which varies during the zigzag formation as depicted in Figure 2a-b. To this end, we computed the surface energy of the liquid droplet and the interface with the nanowire using the finite-element based software Surface Evolver.³⁹ We used a Young angle of 43° , which is the experimental value found ex-situ.⁵⁶ Young's angles differing from 43° do not change the conclusion regarding alternating stability, the only modify the threshold for heterotwin formation.

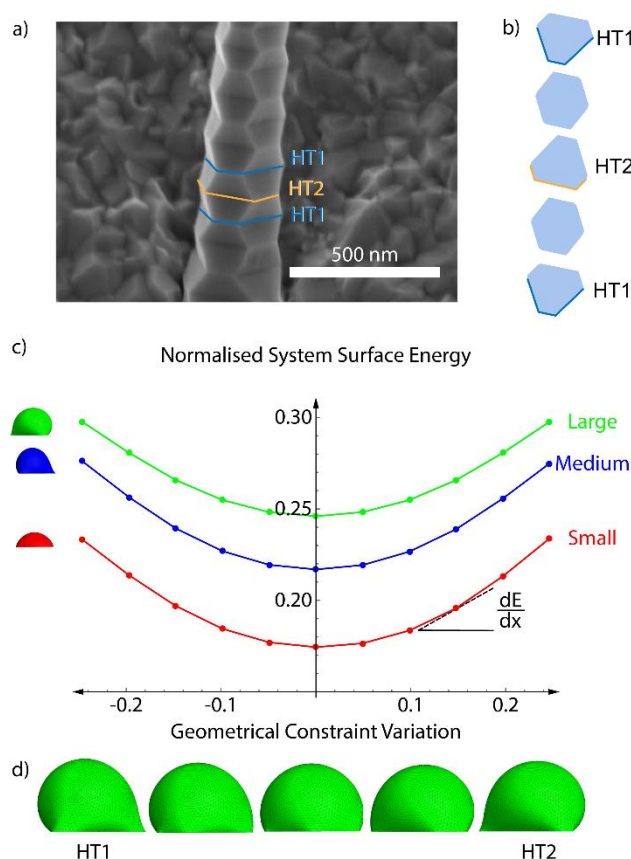


Figure 2. a) Secondary electron SEM image of a zigzag Zn_3P_2 nanowire b) schematic of the development of the cross-section of the nanowire as a function of the nanowire's growth axis, c) Results of the computation of the system (droplet and nanowire's top facet) normalised surface energy (normalisation explained in the text) as a function of the variation of the geometry of the NW's top facet for three different referential droplet volume: small (red), medium (blue) and large (green); d) 3D sketch of the large droplet morphology upon the zigzag period.

Figure 2c illustrates the evolution of the surface energy of the droplet plus the liquid-solid interface during one zigzag cycle. We include the curves for three relative values of droplet volumes, which all follow a similar trend. The total surface energy has been normalised by the average length of the sides, constant throughout all simulations, by the surface energy of a floating sphere with an identical volume, and by the surface tension of the liquid-vapour interface. Due to the pinning of the liquid at the edge of the faceted nanowires, an increase in the liquid volume results in the increase of the apparent contact angle.⁵⁶ The normalised surface energy increases with the liquid volume due to the expansion and deformation of the liquid surface at the edges. The lowest normalised surface energy corresponds to the configuration with hexagonal nanowire cross-section, where the droplet is the least deformed. The normalised surface energy increases parabolically (to a second order approximation) with the modification of the liquid-solid interface area. The slope of the curve increases with the droplet deformation. A representative display of the predicted droplet shape during the zigzag process is shown in Figure 2d. It shows that the deformation is larger at the corners of the cross-section. In addition, the local and overall deformations are the largest when the cross-section is the closest to a triangular shape. This increasing deformation with the deviation from a

hexagonal cross-section explains the increase in the normalised surface energy.

The introduction of a heterotwin constitutes a mechanism to stop the increase in surface energy during the nanowire elongation caused by the droplet's deformation.^{53,57} As the energy required to form a heterotwin (E_{HT}) is fixed, there is a critical geometry of the nanowire's cross-section after which it is energetically favourable to insert a heterotwin rather than to continue increasing the total normalised surface energy. The probability of creating a heterotwin along the nanowire axis, $P(x)$, should thus increase with the normalised surface energy of the system, $\gamma(x)$, as:

$$P(x) \sim \frac{\gamma(x)}{E_{HT}A(x)} \quad (2)$$

After formation of a heterotwin, the normalised surface energy decreases with nanowire elongation due to the change in the facet orientation and return towards a hexagonal cross section.

Optical Properties

Previous studies on Zn_3P_2 indicate that it exhibits a direct bandgap at ~ 1.5 eV, which is close to the ideal bandgap for the highest efficiency of single junction solar cells.⁵⁸ In our recent work, we demonstrated that zigzag Zn_3P_2 nanowires luminesce at 1.43 eV at cryogenic temperatures, which is relatively close to the expected value of the bandgap.²⁴ We have observed that in Zn_3P_2 nanowires with a square cross-section, luminescence can vary with the relative stoichiometry between the Zn and P.²⁴ Given the composition variation at the heterotwin in the zigzag nanowires, the question arises of whether the optical properties vary at these points. To ascertain their potential influence, we performed CL on zigzag nanowires at room temperature. The experimental conditions were chosen as to decrease the diffusion length and allow for higher spatial resolution measurements compared to previous studies.

Figure 3a shows a panchromatic map of the CL emission. We observe a $\sim 10\%$ variation in the emission intensity around edges and on the outward facet orientation compared to that of the inward orientation of the zigzag structure. We attribute this fluctuation to the variations in electron-beam excitation as a function of the morphology (see SI for more details). Detailed spectra along one oscillation of the zigzag morphology indicated by the arrow in Figure 3a are shown in Figure 3b. The spectra along and on each side of the heterotwin are qualitatively extremely similar. The similarity of the spectra along the zigzag structure could be due to the carrier diffusion length being larger than the excitation volume.⁵⁸ We observe two main peaks centred around 869 and 950 nm (1.43 eV and 1.30 eV, respectively), which correspond to sub-bandgap emission, potentially caused by the incorporation of indium in the bulk.⁵⁹ First principle simulations should be performed to confirm this hypothesis. We also distinguish a third weaker peak centred around 748 nm (1.66 eV). This peak could correspond to emission from the Γ^2 transition 260 meV above the bandgap, available due to the high energy excitation of CL.^{58,60}

Conclusions

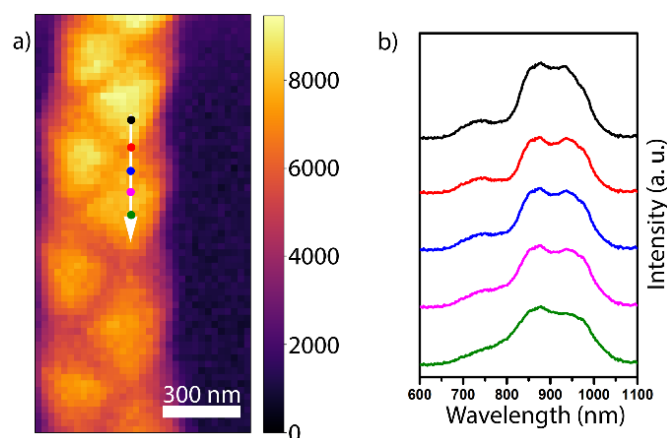


Figure 3. (a) High-resolution panchromatic CL intensity map of a zigzag nanowire with the white arrow indicating the linescan of the extracted spectra in (b), of which the second and fourth from the top were extracted from regions on top of the heterotwin.

In conclusion, we have demonstrated that the Zn_3P_2 superlattice nanowires do not form through regular twinning, as observed in their III-V analogue. Instead, an In-rich heterotwin is formed, as shown through EELS mapping and aberration-corrected STEM imaging, which facilitates the rotation of the crystal structure between segments through the inset of a separate material. Furthermore, we developed a model to explain the onset of heterotwin formation. Based on the non-polar nature of Zn_3P_2 we could tie the model solely to the constraints posed by the droplet shape as a function of the nanowire cross-section. Characterisation of the emission through room temperature CL shows no effect of the heterotwins on the functional properties.

Conflicts of interest

There are no conflicts to declare.

Acknowledgements

S. E. S., E. S., M. Z., R. P., J. L., and A. F. i M. were supported by the SNSF Consolidator grant BSCGIO-157705. N. T. and A. F. i M. were supported by SNSF grant 20B2-1 17668. L.G., W. C. C., and A. F. i M. were supported by SNSF via project 200021_169908 and SCR0222237. R. R. Z. was supported by EPFL-CIME. F. S. H., Q. M. R., and the SuperSTEM Laboratory, the U. K. National Research Facility for Advanced Electron Microscopy, were supported by the Engineering and Physical Sciences Research Council (EPSRC).

Notes and references

- 1 J. Arbiol, M. de la Mata, M. Eickhoff and A. F. i Morral, *Mater. Today*, 2013, **16**, 213–219.
- 2 P. C. McIntyre and A. Fontcuberta i Morral, *Mater. Today Nano*, 2020, **9**, 100058.
- 3 K. A. Dick, K. Deppert, M. W. Larsson, T. Mårtensson, W. Seifert, L. R. Wallenberg and L. Samuelson, *Nat. Mater.*, 2004, **3**, 380–384.

- 4 L. Güniat, P. Caroff and A. Fontcuberta i Morral, *Chem. Rev.*, 2019, **119**, 8958–8971.
- 5 M. S. Gudiksen, L. J. Lauhon, J. Wang, D. C. Smith and C. M. Lieber, *Nature*, 2002, **415**, 617–620.
- 6 K. A. Dick, C. Thelander, L. Samuelson and P. Caroff, *Nano Lett.*, 2010, **10**, 3494–3499.
- 7 P. Caroff, K. A. Dick, J. Johansson, M. E. Messing, K. Deppert and L. Samuelson, *Nat. Nanotechnol.*, 2009, **4**, 50–55.
- 8 R. E. Algra, M. A. Verheijen, M. T. Borgstrom, L.-F. Feiner, G. Immink, W. J. P. van Enckevort, E. Vlieg and E. P. A. M. Bakkers, *Nature*, 2008, **456**, 369–372.
- 9 G. Shen, P.-C. Chen, Y. Bando, D. Golberg and C. Zhou, *J. Phys. Chem. C*, 2008, **112**, 16405–16410.
- 10 D. Spirkoska, J. Arbiol, A. Gustafsson, S. Conesa-Boj, F. Glas, I. Zardo, M. Heigoldt, M. H. Gass, A. L. Bleloch, S. Estrade, M. Kaniber, J. Rossler, F. Peiro, J. R. Morante, G. Abstreiter, L. Samuelson and A. Fontcuberta i Morral, *Phys. Rev. B*, 2009, **80**, 245325.
- 11 M. De Luca, C. Fasolato, M. A. Verheijen, Y. Ren, M. Y. Swinkels, S. Kölling, E. P. A. M. Bakkers, R. Rurali, X. Cartoixa and I. Zardo, *Nano Lett.*, 2019, **19**, 4702–4711.
- 12 Z. Ikonik, G. P. Srivastava and J. C. Inkson, *Phys. Rev. B*, 1995, **52**, 14078–14085.
- 13 Z. Ikonik, G. P. Srivastava and J. C. Inkson, *Phys. Rev. B*, 1993, **48**, 17181–17193.
- 14 M. Y. Swinkels and I. Zardo, *J. Phys. D*, 2018, **51**, 353001.
- 15 N. Guan, X. Dai, A. V. Babichev, F. H. Julien and M. Tchernycheva, *Chem. Sci.*, 2017, **8**, 7904–7911.
- 16 P. Krogstrup, H. I. Jørgensen, M. Heiss, O. Demichel, J. V. Holm, M. Aagesen, J. Nygard and A. Fontcuberta i Morral, *Nat. Photonics*, 2013, **7**, 306–310.
- 17 S. A. Mann, R. R. Grote, R. M. Osgood Jr., A. Alu and E. C. Garneet, *ACS Nano*, 2016, **10**, 8620–8631.
- 18 Z. Ikonik, G. P. Srivastava and J. C. Inkson, *Solid State Commun.*, 1993, **86**, 799–802.
- 19 X.-S. Fang, C.-H. Ye, L.-D. Zhang and T. Xie, *Adv. Mater.*, 2005, **17**, 1661–1665.
- 20 Q. Li, X. Gong, C. Wang, J. Wang, K. Ip and S. Hark, *Adv. Mater.*, 2004, **16**, 1436–1440.
- 21 G. Shen, Y. Bando, B. Liu, C. Tang and D. Golberg, *J. Phys. Chem. B*, 2006, **110**, 20129–20132.
- 22 R. Wagner and W. Ellis, *Applied Physics Letters*, 1964, **4**, 89–90.
- 23 R. Katsube and Y. Nose, *J. Solid State Chem.*, 2019, **280**, 120983.
- 24 S. Escobar Steinvall, N. Tappy, M. Ghasemi, R. R. Zamani, T. LaGrange, E. Z. Stutz, J.-B. Loran, M. Zamani, R. Paul and A. Fontcuberta i Morral, *Nanoscale Horiz.*, 2020, **5**, 274–282.
- 25 J. P. Bosco, G. M. Kimball, N. S. Lewis and H. A. Atwater, *J. Cryst. Growth*, 2013, **363**, 205–210.
- 26 R. Paul, N. Humblot, S. E. Steinvall, E. Z. Stutz, S. S. Joglekar, J.-B. Loran, M. Zamani, C. Cayron, R. Logé, A. G. del Aguila, Q. Xiong and A. F. i Morral, *Cryst. Growth Des.*, 2020, 3816–3825.
- 27 N. Y. Dzade, *Phys. Chem. Chem. Phys.*, 2020, **22**, 1444–1456.
- 28 M. Y. Swinkels, A. Campo, D. Vakulov, W. Kim, L. Gagliano, S. Escobar Steinvall, H. Detz, M. De Luca, A. Lugstein, E. P. A. M. Bakkers, A. Fontcuberta i Morral and I. Zardo, *Phys. Rev. Appl.*
- 29 M. V. Stackelberg and R. Paulus, *Z. phys. Chem*, 1935, **28**, 427–460.
- 30 M. Bhushan and A. Catalano, *Appl. Phys. Lett.*, 1981, **38**, 39–41.
- 31 T. Suda, K. Kakishita, H. Sato and K. Sasaki, *Appl. Phys. Lett.*, 1996, **69**, 2426–2428.
- 32 H. S. Im, K. Park, D. M. Jang, C. S. Jung, J. Park, S. J. Yoo and J.-G. Kim, *Nano Lett.*, 2015, **15**, 990–997.
- 33 H. S. Kim, Y. Myung, Y. J. Cho, D. M. Jang, C. S. Jung, J. Park and J.-P. Ahn, *Nano Lett.*, 2010, **10**, 1682–1691.
- 34 S. B. Choi, M. S. Song and Y. Kim, *J. Phys. Chem. C*, 2019, **123**, 4597–4604.
- 35 W. Shockley and H. J. Queisser, *J. Appl. Phys.*, 1961, **32**, 510–519.
- 36 S. Rühle, *Sol. Energy*, 2016, **130**, 139–147.
- 37 R. Yang, Y.-L. Chueh, J. R. Morber, R. Snyder, L.-J. Chou and Z. L. Wang, *Nano Lett.*, 2007, **7**, 269–275.
- 38 G. Lombardi, F. de Oliveira, M. Teodoro and A. Chiquito, *Appl. Phys. Lett.*, 2018, **112**, 193103.
- 39 K. A. Brakke, *Exp. Math.*, 1992, **1**, 141–165.
- 40 *MSA for Digital Micrograph*, HREM Research, <https://www.hremresearch.com/Eng/plugin/MSAEng.html>.
- 41 F. de la Pena, T. Ostasevicius, V. Tonaas Fauske, P. Burdet, P. Jokubauskas, M. Nord, M. Sarahan, E. Prestat, D. N. Johnstone, J. Taillon, undefined Jan Caron, T. Furnival, K. E. MacArthur, A. Eljarrat, S. Mazzucco, V. Migunov, T. Aarholt, M. Walls, F. Winkler, G. Donval, B. Martineau, A. Garmannslund, L.-F. Zagonel and I. Iyengar, *Microsc. Microanal.*, 2017, **23**, 214–215.
- 42 J. Mooney and P. Kambhampati, *J. Phys. Chem. Lett.*, 2014, **5**, 3497–3497.
- 43 C. Klein, B. Dutrow, J. D. Dana and C. Klein, *Manual of mineral science*, Wiley New York, 2002.
- 44 R. R. Zamani, F. S. Hage, S. Lehmann, Q. M. Ramasse and K. A. Dick, *Nano Lett.*, 2018, **18**, 1557–1563.
- 45 J. A. Mundy, Q. Mao, C. M. Brooks, D. G. Schlom and D. A. Muller, *Appl. Phys. Lett.*, 2012, **101**, 042907.
- 46 D. Bhattacharyya, X.-Y. Liu, A. Genc, H. L. Fraser, R. G. Hoagland and A. Misra, *Appl. Phys. Lett.*, 2010, **96**, 093113.
- 47 D. Bhattacharyya, N. A. Mara, P. Dickerson, R. G. Hoagland and A. Misra, *Acta Mater.*, 2011, **59**, 3804–3816.
- 48 R. R. Zamani and J. Arbiol, *Nanotechnology*, 2019, **30**, 262001.
- 49 A. P. Goldstein, S. C. Andrews, R. F. Berger, V. R. Radmilovic, J. B. Neaton and P. Yang, *ACS Nano*, 2013, **7**, 10747–10751.
- 50 J. Hoemke, E. Tochigi, T. Tohei, H. Yoshida, N. Shibata, Y. Ikuhara and Y. Sakka, *J. Am. Ceram. Soc.*, 2018, **101**, 2616–2626.
- 51 J. Hoemke, E. Tochigi, T. Tohei, H. Yoshida, N. Shibata, Y. Ikuhara and Y. Sakka, *J. Am. Ceram. Soc.*, 2017, **100**, 4252–4262.
- 52 H. Schmid, E. Okunishi, T. Oikawa and W. Mader, *Micron*, 2012, **43**, 49–56.
- 53 T. Burgess, S. Breuer, P. Caroff, J. Wong-Leung, Q. Gao, H. Hoe Tan and C. Jagadish, *ACS Nano*, 2013, **7**, 8105–8114.
- 54 N. Isik Goktas, A. Sokolovskii, V. G. Dubrovskii and R. R. LaPierre, *Nano Lett.*, 2020, **20**, 3344–3351.
- 55 M. de la Mata, R. R. Zamani, S. Martí-Sánchez, M. Eickhoff, Q. Xiong, A. Fontcuberta i Morral, P. Caroff and J. Arbiol, *Nano Lett.*, 2019, **19**, 3396–3408.
- 56 L. Ghisalberti, H. Potts, M. Friedl, M. Zamani, L. Güniat, G. Tütüncüoğlu, W. C. Carter and A. F. i Morral, *Nanotechnology*, 2019, **30**, 285604.
- 57 F. M. Ross, J. Tersoff and M. C. Reuter, *Phys. Rev. Lett.*, 2005, **95**, 146104.
- 58 G. M. Kimball, A. M. Mueller, N. S. Lewis and H. A. Atwater, *Appl. Phys. Lett.*, 2009, **95**, 112103.
- 59 R. Katsube, H. Hayashi, A. Nagaoka, K. Yoshino, Y. Nose and Y. Shirai, *Jpn. J. Appl. Phys.*, 2016, **55**, 041201.
- 60 J. Andrzejewski and J. Misiewicz, *Phys. Status Solidi B*, 2001, **227**, 515–540.

Supplementary Information to “Heterotwin Zn_3P_2 superlattice nanowires: the role of indium insertion in the superlattice formation mechanism and their optical properties.”

Simon Escobar Steinvall^{1*}, Lea Ghisalberti^{1*}, Reza R. Zamani^{2*}, Nicolas Tappy¹, Fredrik S. Hage³, Elias Stutz¹, Mahdi Zamani¹, Rajrupa Paul¹, Jean-Baptiste Leran¹, Quentin M. Ramasse³, W. Craig Carter^{1,4}, Anna Fontcuberta i Morral^{1,5}

* Equal contribution

1 Laboratory of Semiconductor Materials, Institute of Materials, École Polytechnique Fédérale de Lausanne, 1015 Lausanne, Switzerland

2 Centre Interdisciplinaire de Microscopie Électronique, École Polytechnique Fédérale de Lausanne, 1015 Lausanne, Switzerland

3 SuperSTEM Laboratory, SciTech Daresbury Campus, Keckwick Lane, Warrington WA4 4AD, United Kingdom

4 Department of Materials Science and Engineering, Massachusetts Institute of Technology, Cambridge, Massachusetts 02139, USA

5 Institute of Physics, École Polytechnique Fédérale de Lausanne, 1015 Lausanne, Switzerland

Parameter definition

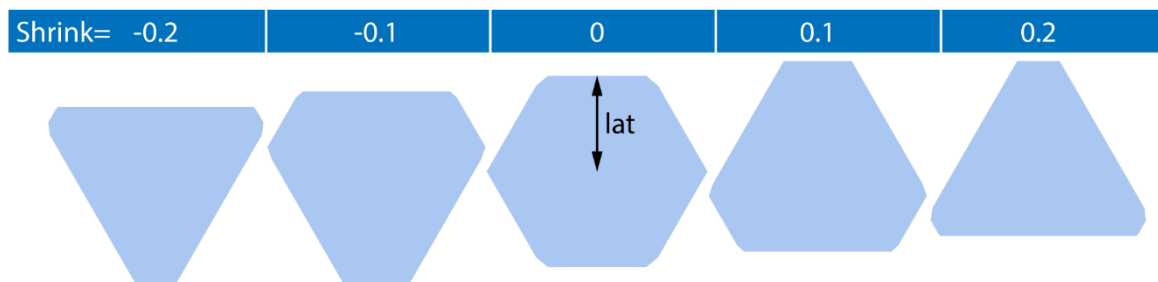


Figure S1. Illustration of the parameters used to model the droplet behaviour.

Core-loss electron energy-loss spectra

Fitting of the EEL maps are done using the peak at 443 eV for In and 1020 eV for Zn. EEL spectra after denoising are shown in Figure S2, showing the In (a) and Zn signal (b). The fitting is done using the software Gatan Digital Micrograph v2.32.

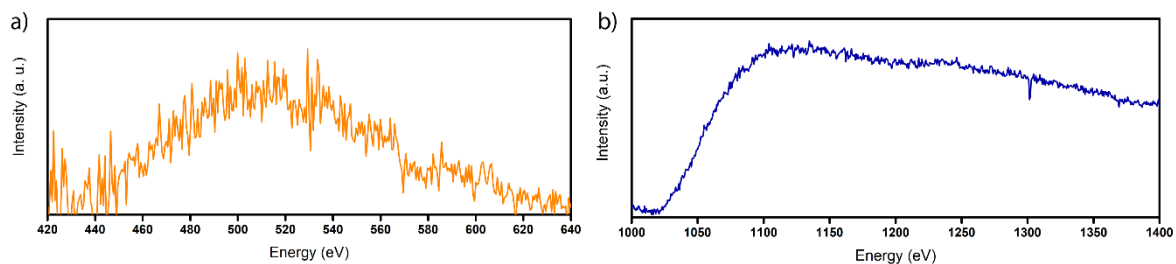


Figure S2. (a) EEL spectrum showing the In peak and (b) EEL spectrum showing the Zn peak used for mapping.

Oscillation Modelling

In Figure S3a we show a HR-TEM image of a zigzag Zn_3P_2 nanowire. We can clearly observe the presence of a sharp interface between regions having different crystal orientation (having different contrast as well). This interface occurs where the heterotwin forms and produces the change the crystal orientation. To investigate the driving forces at the origin of this growth process, we looked for a periodicity rule in the insertion of these

heterotwins as a function of the length of the nanowire. Due to the tapering effect influencing the width of the nanowire along its growth axis, we decided to measure the position and the nanowire's width at which the heterotwin is inserted through the software ImageJ. In Figure S3b we show the data points collected and the periodic function fitting the data.

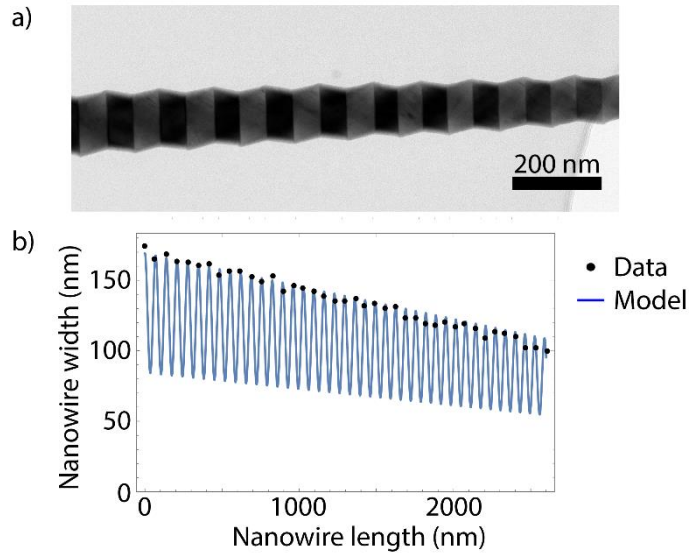


Figure S3. a) TEM image of zigzag Zn_3P_2 nanowire grown by MBE and b) plot of the development of an approximation of the nanowire's width as a function of the nanowire's growth axis: the dots represent the measurements taken on the sample shown in a) with fitting function reported in equation (1).

The selected periodic function (eq. 1) has a linear decay in the amplitude and an exponential decay in the frequency of insertion of the heterotwin. W_0 and h_0 are the initial width of the nanowire and the initial separation between the first two consecutive heterotwins observed in the nanowire. The fitting to the data produces $\pi/2.02$ (89°) for the tapering factor, which corresponds to the tapering angle measured in zigzag nanowires through SEM analysis (i.e., the amplitude linear decay); and 2×10^{-5} for the continuous decay rate of the separation, characterizing the exponential decay in the heterotwin insertion periodicity. We believe that the tapering factor and the continuous decay rate coefficient depends on the MBE growth conditions, i.e. temperature and II-V ratio.

$$W(x) = \left(W_0 - \frac{W_0 - \frac{W_0}{2}}{2} - \frac{x}{\tan \frac{\pi}{2.02}} \right) \left(1 + \frac{1}{3} \cos \frac{2\pi x}{h_0 e^{-2 \times 10^{-5} x}} \right) \quad (1)$$

Casino simulations of energy deposition in a superlattice nanowire

The simulations performed using CASINO software (V3.3) are presented in Figure S4. It can be observed that the extent of the beam interaction volume in Zn_3P_2 does not exceed 50 nm in depth and laterally at an acceleration voltage of 3kV. The assumption that no energy reaches through the sample at this acceleration voltage is thus well verified for most probed points on the CL map. Additionally, the total amount of energy deposited in the sample varies by 17% between outwards and inwards facing apices. This is explained by the variation in backscattering coefficient (η), which is largely influenced by the local geometry. We make the argument that the CL emission should follow the energy deposited by the beam. Accordingly, the superlattice nanowire local geometry is sufficient to explain the dark edge-contrast observed in the panchromatic CL map (Figure 3).

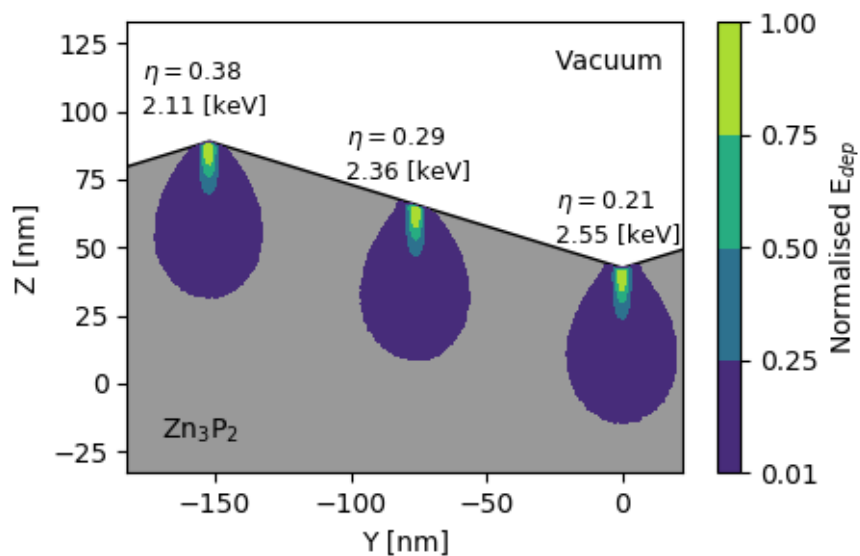


Figure S4 CASINO Simulation of energy deposited in the sample for different edge configuration. Coloured surfaces show the decrease in energy density deposited in the sample, normalised to the maximum. Annotations show the fraction of backscattered electrons (η) and the total amount of energy (in keV) deposited in the sample per electron, for each edge configuration. It is observed that outwards facing apices (left) show enhanced backscattering compared to inwards facing apices (right) or facets (middle). Simulations were performed using a collimated electron beam of 10 nm diameter at 3 kV and a density of 4.55 g cm^{-3} for Zn_3P_2 . Due to the limited possibilities of simulating complex geometries in CASINO 3, we model the sample with truncated pyramids. This approximation reproduces well local edge configuration, but would not be valid in experiment conditions where a significant part of the beam energy is transmitted through the sample, e.g. at high beam energies.

6 Nucleation in the vapor-liquid-solid growth mode modeled with Surface Evolver

Beyond the basic considerations regarding the NW's geometrical constraints, the presence of sides and corners composing the edge of the top facet creates some inhomogeneity from the energetical point of view. The majority of the nucleation theories proposed until now for NW growth highlight the importance of the nucleation site in the determination of the crystal phase. For example, in the case of gold-catalyzed MOCVD GaAs NWs it was observed through in-situ TEM measurements that Wurtzite structure develops in a layer-by-layer growth, starting from the TPL line.[109]. Also for self-catalyzed GaAs NWs, it has been shown experimentally that wurtzite monolayers nucleate at the corners.[117] The fact that the formation of a new layer starts at the TPL may suggest that the nucleation of such layer is happening at the TPL, which gives further relevance to the liquid-contribution to the phenomenon. Indeed, even though the difference in the reactive properties of edges and corners from the chemical/physical prospective is well known, linked to dangling bonds and crystallographic plane stability, the effect of edges and corners on the morphology and stability of the liquid phase is often neglected when analysing the growth. We think that the dispersion in the apparent wetting angle resulting from the presence of faceted NWs may alter the local energetic stability of the system along the TPL. The target of this analysis is to provide insight in the nucleation of GaAs crystals by VLS methodology, particularly for NW's growth, is influenced and facilitated at the TPL due to the presence of unbalanced capillarity tension along the perimeter of the catalytic droplet.[93] The effect of these forces becomes evident observing liquids wetting deformable materials. In such cases the deformation often leads to the formation of peaks following the inclination of the wetting angle itself along the TPL. This is why we think that disomogeneity in the apparent angle around the droplet perimeter can cause preferential nucleation sites. In this work we indicate that the stretching caused by the liquid cause a deformation in the shape of the nucleus of the new phase, with consequent change in the surface energy of the system modifying the overall dynamic of nucleation. In order to check this hypothesis, we adopt the following main assumption: early stage nuclei behave as liquids. This assumption is supported by the recent observations through Atomic Electron Tomography of the anisotropy of early stages nuclei for FePt nanoparticles undertaking phase transition.[79] Thanks to this assumption we can take advantage of the software Surface

Evolver to compute and determine the equilibrium morphology of the new stretched phase and its surface energy size-dependence, essential for the computation of the nucleation curve, representing the Gibbs energy necessary for the considered transition as a function of the size of the nucleating phase. In the first part of this chapter, we first introduce the method used for computing the volumetric and the superficial contributions to the total energy of the system. We verify the method by applying it to the well known cases of homonucleation and heteronucleation far away from the TPL. The obtained results are then compared to the nucleation taking place at the TPL. In the second section, we observe the effect of droplet's wetting angle on the morphology of the germ of the new phase, and analyse its deformation caused by capillary forces. We verify the effect of this deformation by studying the variation of the critical size and nucleation barrier for the new layer germ formation as a function of the liquid wetting angle.

6.1 System definition and computation of the free energy values

The aim of this chapter is to analyse the nucleation event at the origin of GaAs NWs by computing the nucleation curves for a specific phase transition. The shape and geometry of the nucleus is key in determining the nucleation curves, due to the continuous interplay between surface and bulk effects. Since phase transitions corresponds to saddle points in the energy landscape of the system, we identify the most reasonable shape as the one associated with the local minimum. For determining the critical nucleation energy barrier, characterizing the saddle point, we then shift towards a maximizing process in which we study the increase of the energy of the system by increasing the volume. In this section, we compute the morphologies associated with these saddle points by minimizing the surface energy of the system analysed in different configurations and under different constraints. We will then proceed in determining their nucleation volumes and energies. The computations are an extension of the classical homogeneous nucleation problem on a flat surface, where the minmax shape is a spherical cap. Here, the most important contribution is to consider another case where nucleation occurs along a triple line—and the minimal shape does not consist of a spherical cap, or a combination of several such caps.

To compute the nucleation curves we define the volumetric and surface contribution to the system total energy of final and initial states in order to figure out the size-dependence of the Gibbs free energy. The system considered is composed by the substrate, the vapor, the liquid and the nucleating solid phases. The substrate is GaAs, the liquid is 98% Gallium and 2% Arsenic and the vapor is a mixture of Ga and As₄. The new solid phase nucleating in the liquid is FCC GaAs. In order to properly define the formation energy relative to this phase transition, we need to define the system and its referential Gibbs free energy curves. The phase diagram and curves considered here have been calculated by Dimitra Spathara for the equilibrium at 740°C and 2% As mole fraction through the software Calphad and they are reported in Fig. 6.1

For calculating the formation energy of GaAs we assume that the liquid phase has fixed volume

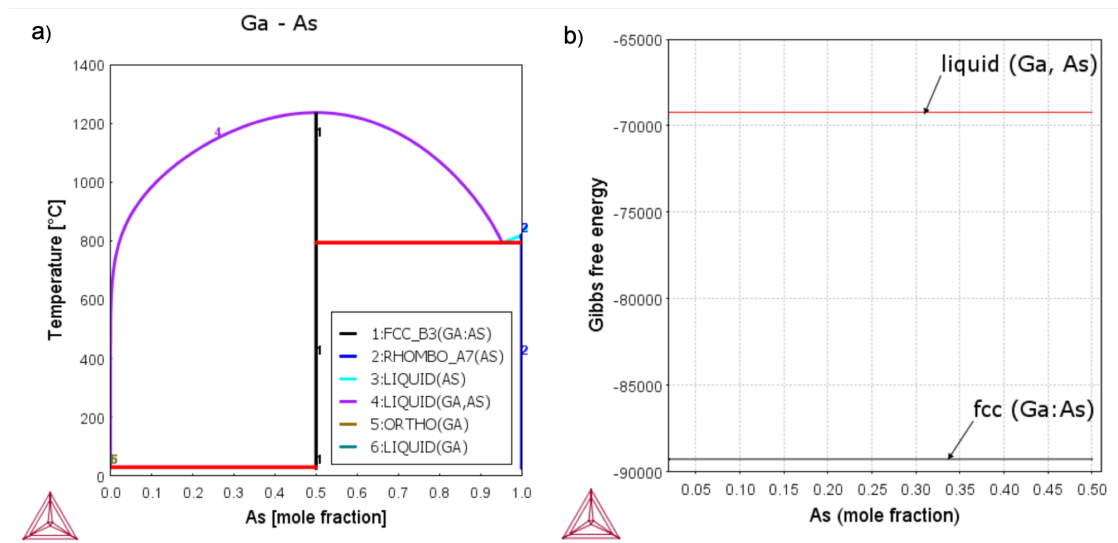


Figure 6.1 – Phase diagram (a) and the free energy curves (b) computed through Calphad of the system analyzed.

during the process as a result of a steady state reactive condition: we assume that the balance between the material used to generate the new phase and the material supplied by the vapor phase is perfect, allowing the liquid phase to maintain constant volume. By considering the values calculated through Calphad and reported in Fig. 6.1 we subtract from the Gibbs free energy of the final state (fcc GaAs) the Gibbs free energy of the initial state (liquid) and we transform the values from J/mol to J/m³. The obtained value of the formation energy is $-7.40304 \cdot 10^8$ J/m³. Regarding the surface energy contribution to the total energy, we fix the liquid to nucleus ratio to 200. The surface tensions implemented are set as follows: liquid-vapor tension= 1 N/m, nucleus-vapor tension= 0.9 N/m and nucleus-liquid tension= 1.1 N/m. The selected values are not specific for the different phases themselves but they were chosen in order to ensure the right condition of the system. In particular, the condition reported in eq. (6.1) need to be satisfied in order to avoid both separation and engulfing between the two phases.

$$\gamma^{(nucleus-vapor)} < \gamma^{(liquid-vapor)} + \gamma^{(liquid-nucleus)} \quad (6.1)$$

For the energetic contributions related to the substrate-liquid interface and the substrate-liquid interfaces we used the Young equation with, respectively, 51° and 60° wetting angles. Since the equilibrium shape of the new phase in both homogeneous and heterogeneous cases can be easily modelled, we performed the calculations by hand following the classical definition of system surface energy: the sum of all the surface areas present in the system multiplied for their respective surface energy. In the case of the nucleation at the TPL, due to the capillary forces acting on the new phase, we use the software Surface Evolver for computing the equilibrium

shape and the associated system surface energy.

6.2 Modelling nucleation with Surface Evolver

The main focus of this part is to determine the modification of the nucleation curve as a function of the position of the nucleation event. The configurations selected for this analysis are depicted in Fig. 6.2, being correspondent to the following nucleation cases: homonucleation, heteronucleation far away from the TPL and heteronucleation at the TPL. An additional location for the nucleation has been identified at the vapor-liquid interface, which can be represented as a floating disk on the catalyzer surface. Nevertheless we do not treat this case here since it is not directly connected with the NW growth mode happening through layer-by-layer mechanism, thus taking place at the substrate-liquid interface.

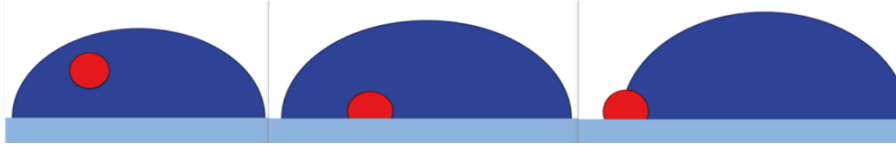


Figure 6.2 – Sketches of the 3 configurations in which the nucleation of the new solid phase can take place.

In order to quantitatively determine the kinetically favoured process for this phase transition we can measure from the nucleation curve its specific critical radius and energy barrier. The critical radius refers to the minimal size of the germ of the new phase allowing the system to enter into a stable state. The lower it is, the easier it is to nucleate the stable germ which will then enlarge during the growth. The energy barrier is the Gibbs energy necessary to reach the critical size for stability, thus representing the price to pay for the the formation of the new phase. The critical size is the radius solving eq. (6.2) while the energy barrier (ΔE) is defined by eq. (6.3) :

$$\frac{\delta \Delta G}{\delta r} = 0 \quad (6.2)$$

$$\Delta E = \Delta G(r^{crit}) \quad (6.3)$$

At first we want to clarify the reliability of the absolute values of both critical radius and energy barrier obtained. Our results, in particular regarding the critical radius, are indeed too small to have physical meaning but nevertheless they do not hinder the efficacy of the main purpose of this analysis: that is to say the comparison between the nucleation probability at different locations. In this work we are interested in the relative results and not to the

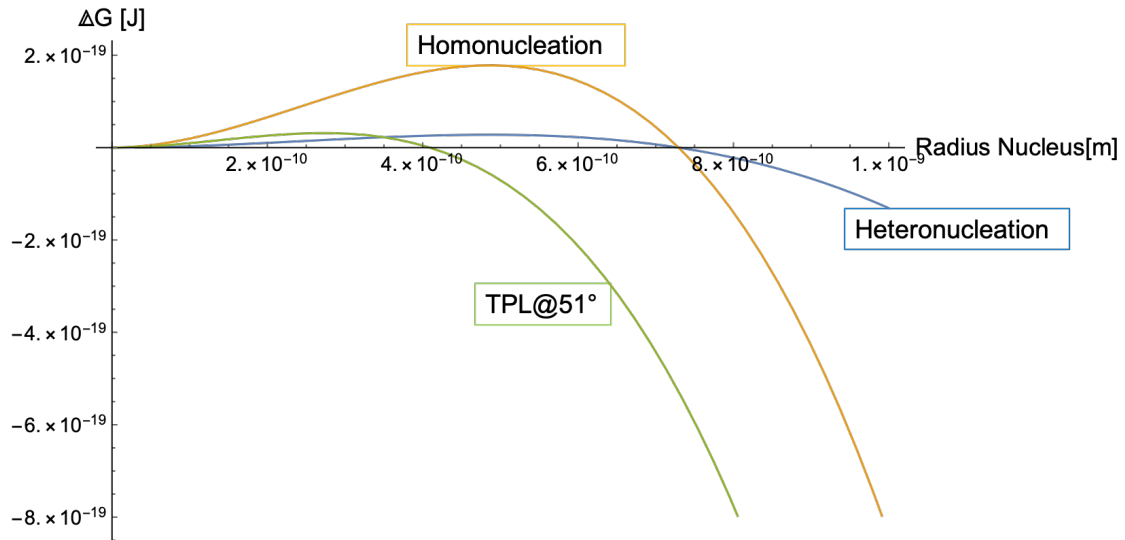


Figure 6.3 – Computation of the nucleation curves for the GaAs phase transtion through VLS growth mode with the liquid wetting angle 51° and nucleus wetting angle 60° as a function of the radius of the nucleus for the 3 location considered: floating in the droplet, heteronucleation far away from the TPL and heteronucleation at the TPL.

absolute ones. Moreover, the absolute results strongly depends on the approximations adopted in our model and on the values we took as references for the different interfacial energies considered. These values, being based on theoretical predictions and ideal computational values, often distance them self from real system, still making it impossible to make absolute predictions. We compare the results for the traditional homogeneous and heterogeneous cases, in order to verify the reliability of our simulations. Regarding the critical radius of the nucleus, that is to say the radius at which the nucleation curve reaches its maximum, these two configurations share the same values. According to nucleation theory, the equivalence in the critical radius is expected due to the spherical cap approximation used to calculate the curve for the heterogeneous nucleation. Indeed even if the critical radius is the same, the critical size is smaller for the heteronucleation because the real shape of the nucleus is just a portion of the sphere defined by the critical radius: the shape is the spherical cap whose morphology is defined by the contact angle of the nucleus itself. By focusing on the energy barrier, the maximum height of the nucleation curve, we can confirm that the homonucleation case requires around twice the energy necessary for the heteronucleation case, as expected by nucleation theory. With further analysis we verified and confirmed that the relationship between the two values follows the theoretical predictions reported in eq. (6.4) and (6.5). It is important to underline that traditionally, when far away from the TPL, the wetting angle used in eq. (6.5) refers to the wetting angle that the new phase creates with the substrate: it is thus fundamentally different from the wetting angle of the catalytic liquid phase,

whose contribution really enters into action when analysing the TPL location.

$$\Delta G^{het} = f(\theta) \Delta G^{hom} \quad (6.4)$$

$$f(\theta) = \frac{2 - 3\cos(\theta) + \cos^3(\theta)}{4} \quad (6.5)$$

We focus now on the comparison between the traditional heteronucleation (occurring far away from the TPL) and the one taking place at the TPL with a liquid wetting the substrate with a contact angle equal to 51° . The critical radius is reduced, meaning that from the point of view of kinetics of reaction, this location ensures the smallest size for stability and thus it is the one with higher probability to happen and start the growth process. While the reduction of the critical size was expected, the energy barrier results slightly increased with respect to the heteronucleation, meaning that the system has to pay more from an energetic point of view, to reach and maintain that configuration. This additional price may be linked to the deformation of the nucleus's shape caused by the capillary forces, which do not allow to get to the lower state of spherical cap configuration. The germ's morphology minimizing the surface energy of the nucleating system computed thanks to Surface Evolver is reported in Fig. 6.4, as a top view in panel (a) and from the side view in panel (b). From the top view image the nucleus show a football-ball shape clearly elongated and stretched by the substrate-liquid-vapor TPL line. From the side view it is possible to appreciate the vertical component of the germ's deformation, visible as a stretching in the direction defined by the wetting angle of the liquid and forming a peak along the whole nucleus-liquid-vapor contact line.

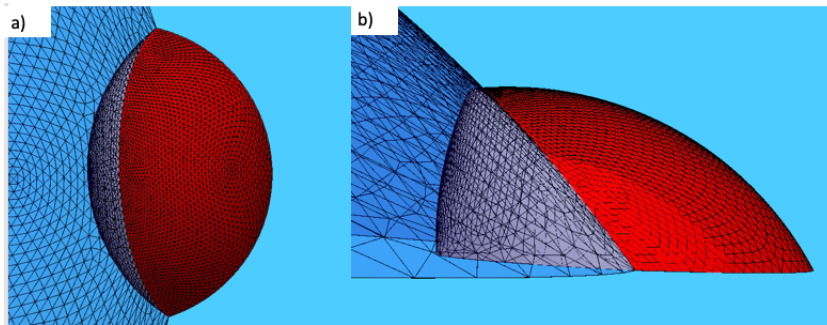


Figure 6.4 – Equilibrium shape of the nucleating phase taking place at the TPL for wetting angle equal to 51° : (a) top view and (b) side-view

6.3 Energy barrier dependency on the liquid wetting angle

In order to investigate the influence of the direction of the capillary forces and their deformation effect on the forming new phase, we decided to compute the equilibrium shapes and the corresponding nucleation curves for different liquid wetting angle, ranging from 30° to 110° . In Fig. 6.6 we show the Surface Evolver morphologies minimizing the surface energy of the systems composed by substrate, nucleus, liquid and vapor for nucleus wetting angle of 60° and liquid wetting angle respectively of (a) 30° , (b) 51° , (c) 70° , (d) 90° , (e) 100° and (f) 110° .

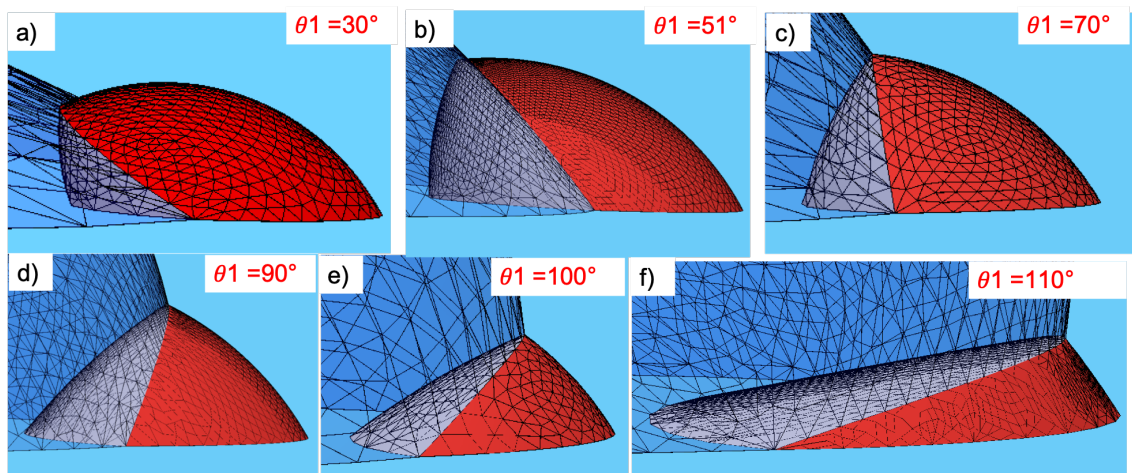


Figure 6.5 – Surface Evolver morphologies minimizing the surface energy of the systems composed by substrate, nucleus, liquid and vapor for nucleus wetting angle of 60° and liquid wetting angle respectively of (a) 30° , (b) 51° , (c) 70° , (d) 90° , (e) 100° and (f) 110°

By changing the droplet wetting angle, it is possible to obtain very different morphologies of the nucleus, going from a partially floating spherical cap (a), passing through a section of a spherical cap (d) until obtaining a disk attached to the substrate (f). Our hypothesis is that different germ's morphologies may influence the next steps of growth, leading for example to Stranski-Krastanov growth regime (d) or to a layer-by-layer mode (f). Nevertheless, it is interesting to note that within wetting angle below 90° the obtained shapes recall pointy ellipsoids, with the sharpness stretching along the direction defined by the wetting angle. For higher wetting angle, the ellipsoid is lost in favour for a more planar geometry. Moreover, it appears that the nucleus's surface area exposed to the vapor phase reduces for increasing wetting angle. This behaviour suggests that for increasing liquid wetting angle there is both an increase in the nucleus deformation (intended as distancing from a spherical cap condition) and a stronger confinement of the new phase into the liquid, represented by the shorter surface area in contact with the vapor.

In Fig. 6.5 we report the computed nucleation curves for GaAs phase transition through VLS growth mode at the TPL with nucleus wetting angle of 60° and liquid wetting angle ranging from 30° to 110° . From the plot it is possible to appreciate the reduction of both the critical size and the nucleation barrier for increasing wetting angle, proving that the higher the wetting

angle is, the easier the nucleation event at the TPL becomes. In particular, we observe that the energy barrier values reduces linearly with the increase of the liquid wetting angle.

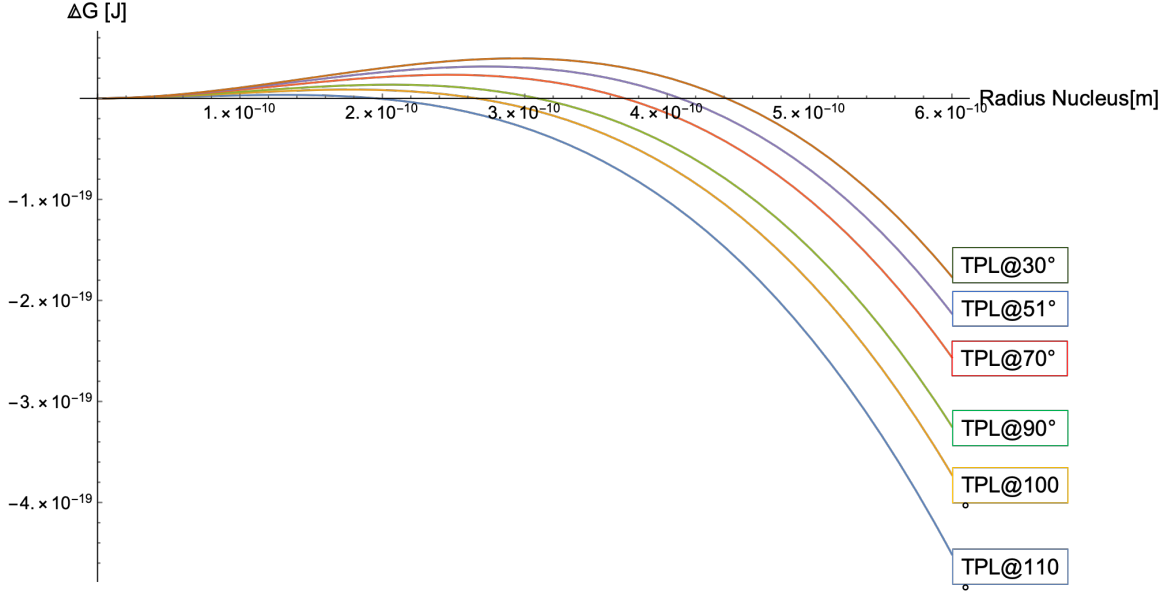


Figure 6.6 – Computation of the nucleation curves for the GaAs phase transtion through VLS growth mode at the TPL with nucleus wetting angle 60° and liquid wetting angle of (a) 30°, (b) 51°, (c) 70°, (d) 90°, (e) 100° and (f) 110°

Recalling the relationship between the homogeneous and heterogeneous nucleations, described by eq. (6.4) and (6.5), we decided to investigate the corresponding relationship also between heterogeneous nucleation far away from the TPL and heteronucleation happening at the TPL. From the results reported in Fig. 6.5 we measured the energy barriers corresponding to each curve and divided them by the value of the energy barrier for the heteronucleation far away from the TPL. The obtained values have been plotted in Fig. 6.7 and fitted through eq. (6.6), given by applying eq. (6.5) applied to a new ratio of energy barriers: the TPL and heteronucleation energy barriers with liquid wetting angle defined by α . Here α is finally taking into consideration the contribution of the catalyzer in the nucleation event. It is practically different from eq. (6.5) since it is considering the next level of wetting, that is to say the wetting of the liquid on the nucleus-substrate system.

$$\frac{\Delta G^{TPL}}{\Delta G^{Het}} = \frac{2 - 3\cos(\alpha) + \cos^3(\alpha)}{4} \quad (6.6)$$

The agreement between the data points and the theoretical prediction suggests us that the stabilization given by the capillary forces can be interpreted as if there was an additional plane available for the nucleus to wet and reduce its surface energy. We can conclude that

the presence of the TPL is not important for the line itself, but mostly for being the border of the liquid-vapor interface, representing a new plane available for the germ to spread and wet and stabilize. We can summarize these findings by interconnecting the homogeneous case with the TPL-nucleation one through eq. (6.7), where θ is the wetting angle of the nucleus on the substrate while α is the wetting angle of the liquid on the substrate. In this equation, the nucleus's wetting process and the influence of the liquid's capillary forces follow the same dependency on each respective wetting angle and their effect can convolute together to describe the entire system.

$$\frac{\Delta G^{TPL}}{\Delta G^{hom}} = f(\theta)f(\alpha) \quad (6.7)$$

Although there is no a priori justification for assuming a fit of the form $f(\theta)f(\alpha)$, it provides a simple characterization in terms of two parameters. As it can be observed by panels (a) and (b) in Fig. 6.6, referred to the cases with low liquid wetting angle, the nucleus is expanding along the vapor-liquid interface like a floating ellipsoid. By considering the liquid-vapor interface as an additional plane suitable for the wetting process, we can thus interpret the TPL as a special type of edge given by the intersection between a solid substrate and the vapor-liquid interface. The advantage of having a vapor-liquid interface stabilizing the nucleus as a solid but at the same time deforming it due to its capillary forces, enables the system and, in particular the nucleus, to adopt new shapes and geometries, creating the initial conditions for the development of different growth modes.

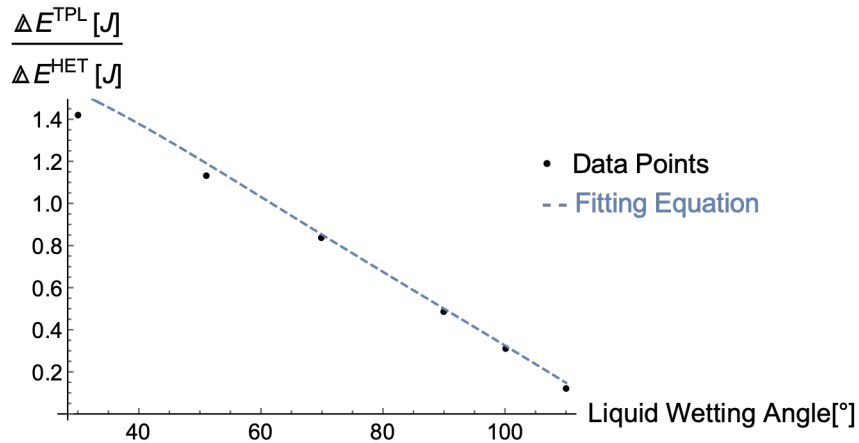


Figure 6.7 – Comparison between data points representing the development of the TPL energy barrier (measured from the curves shown in ig. 6.5, as a function of the wetting angle and the fitting equation reported in eq.(5.6)

Considering the particular case of GaAs NWs grown by VLS method, we can conclude that in case of nucleation at the TPL, the higher the wetting angle of the liquid is, the higher the kinetics of reaction is. Indeed both critical size and energy barrier reduce for increasing

wetting angle, increasing the probability that the GaAs germ will start its growth from this condition. Moreover, by observing the deformation of the nucleus's geometry caused by the capillary forces, we think that the nucleus presenting the most suitable shape for the onset of layer-by-layer growth, typical of III-V NWs, is close to the one shown in Fig. 6.6 (f), given by a liquid wetting angle of 110° . Considering the development of the apparent angle across the perimeter of a droplet wetting a hexagonal-cross section NW, we expect the nucleation to happen along the side of the top facets, where higher apparent angle will be observed.

In this chapter we showed that the presence of the capillary forces acting on the germ of nucleation in correspondence of the triple phase line can modify the dynamics of phase transition. In particular thanks to the software Surface Evolver we estimated the morphology associated with local minima of the system and we performed an investigation of their properties as saddle points by maximizing the volume of the morphology analysed. In this way we could compute referential critical radii and energy barriers which helped us comparing the nucleation event at the TPL with the traditional cases of homonucleation and heteronucleation far away from the TPL.

7 Conclusions and Outlooks

In this thesis we investigated key questions in the fundamental understanding of Vapor-Liquid-Solid growth mode of nanowires. This understanding is extremely important to perform reproducible NW fabrication and their utilization in applications. The first main insight concerns the preparation of arrays of semiconductor nanowires through VLS and selective area epitaxy and the possibility to optimize the vertical yield thanks to the engineering of the wetting behavior of the catalytic droplets at the initial stages of growth. The same phenomenon is first analyzed for arrays produced from cylindrical cavities obtained through traditional lithographic techniques and secondly for arrays produced without lithography and presenting smooth cavities. The second topic analyzed is the wetting behavior of droplets constrained on top of nanowires and/or cylindrical pillars. In such conditions, droplet volume and constraint geometry are the key factors for determining the most stable configuration of the droplet and thus the direction of further layers of growth. Theoretical considerations are linked to experimental results proving the modification of the growth direction of InAs NWs and the possibility to obtain exotic nanostructures by changing the liquid confinement on top of Silicon pillars. Adding a further degree of complexities, we analysed the wetting behavior of droplets on top of non-cylindrical constraints and observed the effect of droplets wetting angle dispersion due to the presence of edges and corners. Zig-zag nanowires and their growth mechanism have been inspected. We observed the interconnection between the modification of the top facet morphology and the liquid deformation, possible responsible of the oscillatory behaviour of the whole structure. In the last chapter we present also some considerations about the nucleation event at the triple-phase line, showing that the support provided by the presence of the liquid can be associated to the addition of a further interface stabilizing the nucleation process.

Our method relies on the continuous interplay between experimental efforts and theoretical modeling, together with the interconnections between thermodynamics and kinetic properties of the system. In particular we proved that the software Surface Evolver is a flexible and reliable tool for analysing many different problems and for contributing in figuring out some invisible factors characterizing solid-liquid interfacial equilibrium and thus influenc-

ing any phase transition processes as well. Just on the base of a solid understanding of the fundamental mechanisms taking place during crystal growth, it is possible to manage and optimize both preparation techniques and final performances of the devices. The generality of the findings that are gathered ensures their transfer to both other growth processes, other type of nanostructures and other materials as well. From a larger point, the analysis of liquid-solid interaction and its consequences on the equilibrium of the system can be relevant also for medical applications and in the development of bioinspired materials. In particular we would like to highlight the need to develop more updated bottom-up based models for analysing nucleation event and growth dynamics. These new theories should be based on the nanometric scale and specific properties of the reactive system in order to surpass the outdated top-down modelling approach of materials phase transition, which relies mostly on bulk materials assumptions.

Bibliography

- [1] Saw-Wai Hla. “Scanning tunneling microscopy single atom/molecule manipulation and its application to nanoscience and technology”. In: *Journal of Vacuum Science Technology B: Microelectronics and Nanometer Structures* 23 (July 2005). DOI: 10.1116/1.1990161.
- [2] Morten Møller et al. “Automated extraction of single H atoms with STM: tip state dependency”. In: *Nanotechnology* 28.7 (2017), p. 075302. DOI: 10.1088/1361-6528/28/7/075302. URL: <https://doi.org/10.1088%2F1361-6528%2F28%2F7%2F075302>.
- [3] D. M. Eigler and E. K. Schweizer. “Positioning single atoms with a scanning tunnelling microscope”. In: *Nature* 344.6266 (Apr. 1990), pp. 524–526. ISSN: 1476-4687. DOI: 10.1038/344524a0. URL: <https://doi.org/10.1038/344524a0>.
- [4] D. Mailly. “Nanofabrication techniques”. In: *The European Physical Journal Special Topics* 172.1 (June 2009), pp. 333–342. ISSN: 1951-6401. DOI: 10.1140/epjst/e2009-01058-x. URL: <https://doi.org/10.1140/epjst/e2009-01058-x>.
- [5] Abhijit Biswas, Ilker S. Bayer, Alexandru S. Biris, Tao Wang, Enkeleida Dervishi, and Franz Faupel. “Advances in top–down and bottom–up surface nanofabrication: Techniques, applications future prospects”. In: *Advances in Colloid and Interface Science* 170.1 (2012), pp. 2 –27. ISSN: 0001-8686. DOI: <https://doi.org/10.1016/j.cis.2011.11.001>. URL: <http://www.sciencedirect.com/science/article/pii/S0001868611001904>.
- [6] Yifang Chen. “Nanofabrication by electron beam lithography and its applications: A review”. In: *Microelectronic Engineering* 135 (2015), pp. 57 –72. ISSN: 0167-9317. DOI: <https://doi.org/10.1016/j.mee.2015.02.042>. URL: <http://www.sciencedirect.com/science/article/pii/S016793171500101X>.
- [7] Department of Electronics and Communication, Jaypee university of Information Technology, Waknaghat, Solan – 173234, India, Himangi Sood, Viranjay M. Srivastava, Department of Electronic Engineering, Howard College , University of KwaZulu - Natal, Durban – 4041, South Africa, Ghanshyam Singh, and Department of Electrical and Electronics Engineering Sciences, Auckland Park Kingsway Campus, University of Johannesburg, PO Box 524, Johannesburg - 2006 , South Africa. “Advanced MOS-FET Technologies for Next Generation Communication Systems - Perspective and Challenges: A Review”. en. In: *Journal of Engineering Science and Technology Review*

- 11.3 (Apr. 2018), pp. 180–195. ISSN: 17919320, 17912377. DOI: 10.25103/jestr.113.25. URL: <http://jestr.org/downloads/Volume11Issue3/fulltext251132018.pdf> (visited on 04/27/2020).
- [8] Himangi Sood, Viranjay Srivastava, and Ghanshyam Singh. “Advanced MOSFET Technologies for Next Generation Communication Systems - Perspective and Challenges: A Review”. In: *Journal of Engineering Science and Technology Review* 11 (Apr. 2018), pp. 180–195. DOI: 10.25103/jestr.113.25.
- [9] Gabriel Lozano, Said RK Rodriguez, Marc A Verschuuren, and Jaime Gómez Rivas. “Metallic nanostructures for efficient LED lighting”. In: *Light: Science & Applications* 5.6 (June 2016), e16080–e16080. ISSN: 2047-7538. DOI: 10.1038/lsa.2016.80. URL: <https://doi.org/10.1038/lsa.2016.80>.
- [10] Debabrata Sikdar, John B. Pendry, and Alexei A. Kornyshev. “Nanoparticle meta-grid for enhanced light extraction from light-emitting devices”. In: *Light: Science & Applications* 9.1 (July 2020), p. 122. ISSN: 2047-7538. DOI: 10.1038/s41377-020-00357-w. URL: <https://doi.org/10.1038/s41377-020-00357-w>.
- [11] Yi Qi and Michael C. McAlpine. “Nanotechnology-enabled flexible and biocompatible energy harvesting”. In: *Energy Environ. Sci.* 3 (9 2010), pp. 1275–1285. DOI: 10.1039/C0EE00137F. URL: <http://dx.doi.org/10.1039/C0EE00137F>.
- [12] Elena Serrano, Guillermo Rus, and Javier García-Martínez. “Nanotechnology for sustainable energy”. In: *Renewable and Sustainable Energy Reviews* 13.9 (2009), pp. 2373–2384. ISSN: 1364-0321. DOI: <https://doi.org/10.1016/j.rser.2009.06.003>. URL: <http://www.sciencedirect.com/science/article/pii/S1364032109001087>.
- [13] Z. Abdin et al. “Solar energy harvesting with the application of nanotechnology”. In: *Renewable and Sustainable Energy Reviews* 26 (2013), pp. 837–852. ISSN: 1364-0321. DOI: <https://doi.org/10.1016/j.rser.2013.06.023>. URL: <http://www.sciencedirect.com/science/article/pii/S1364032113004000>.
- [14] Jayanta Kumar Patra et al. “Nano based drug delivery systems: recent developments and future prospects”. In: *Journal of Nanobiotechnology* 16.1 (Sept. 2018), p. 71. ISSN: 1477-3155. DOI: 10.1186/s12951-018-0392-8. URL: <https://doi.org/10.1186/s12951-018-0392-8>.
- [15] Graham G. Walmsley et al. “Nanotechnology in bone tissue engineering”. In: *Nanomedicine: Nanotechnology, Biology and Medicine* 11.5 (2015), pp. 1253–1263. ISSN: 1549-9634. DOI: <https://doi.org/10.1016/j.nano.2015.02.013>. URL: <http://www.sciencedirect.com/science/article/pii/S1549963415000635>.
- [16] Dwaine F Emerich and Christopher G Thanos. “Nanotechnology and medicine”. In: *Expert Opinion on Biological Therapy* 3.4 (2003). PMID: 12831370, pp. 655–663. DOI: 10.1517/14712598.3.4.655. eprint: <https://doi.org/10.1517/14712598.3.4.655>. URL: <https://doi.org/10.1517/14712598.3.4.655>.

- [17] Jia Yang, Chuang Zhang, XiaoDong Wang, WenXue Wang, Ning Xi, and LianQing Liu. "Development of micro- and nanorobotics: A review". In: *Science China Technological Sciences* 62.1 (Jan. 2019), pp. 1–20. ISSN: 1869-1900. DOI: 10.1007/s11431-018-9339-8. URL: <https://doi.org/10.1007/s11431-018-9339-8>.
- [18] Jiang Li, Alexander A. Green, Hao Yan, and Chunhai Fan. "Engineering nucleic acid structures for programmable molecular circuitry and intracellular biocomputation". In: *Nature Chemistry* 9.11 (Nov. 2017), pp. 1056–1067. ISSN: 1755-4349. DOI: 10.1038/nchem.2852. URL: <https://doi.org/10.1038/nchem.2852>.
- [19] K Eric Drexler. "Productive nanosystems: the physics of molecular fabrication". In: *Physics Education* 40.4 (2005), pp. 339–346. DOI: 10.1088/0031-9120/40/4/003. URL: <https://doi.org/10.1088/0031-9120/40/4/003>.
- [20] Laixia Yang, Iskander Akhatov, Mohammed Mahinfalah, and Bor Jang. "Nano-fabrication: A review". In: *Journal of the Chinese Institute of Engineers* 30 (Apr. 2007), pp. 441–446. DOI: 10.1080/02533839.2007.9671272.
- [21] Hua Wang, Minghua Sun, Kang Ding, Martin T. Hill, and Cun-Zheng Ning. "A Top-down Approach to Fabrication of High Quality Vertical Heterostructure Nanowire Arrays". In: *Nano Letters* 11.4 (2011). PMID: 21417458, pp. 1646–1650. DOI: 10.1021/nl2001132. eprint: <https://doi.org/10.1021/nl2001132>. URL: <https://doi.org/10.1021/nl2001132>.
- [22] Hai-Dong Yu, Michelle D. Regulacio, Enyi Ye, and Ming-Yong Han. "Chemical routes to top-down nanofabrication". In: *Chem. Soc. Rev.* 42 (14 2013), pp. 6006–6018. DOI: 10.1039/C3CS60113G. URL: <http://dx.doi.org/10.1039/C3CS60113G>.
- [23] Li Wang, Yujing Sun, Zhuang Li, Aiguo Wu, and Gang Wei. "Bottom-Up Synthesis and Sensor Applications of Biomimetic Nanostructures". eng. In: *Materials (Basel, Switzerland)* 9.1 (Jan. 2016). Publisher: MDPI, p. 53. ISSN: 1996-1944. DOI: 10.3390/ma9010053. URL: <https://pubmed.ncbi.nlm.nih.gov/28787853>.
- [24] Masatsugu Shimomura and Tetsuro Sawadaishi. "Bottom-up strategy of materials fabrication: a new trend in nanotechnology of soft materials". In: *Current Opinion in Colloid Interface Science* 6.1 (2001), pp. 11–16. ISSN: 1359-0294. DOI: [https://doi.org/10.1016/S1359-0294\(00\)00081-9](https://doi.org/10.1016/S1359-0294(00)00081-9). URL: <http://www.sciencedirect.com/science/article/pii/S1359029400000819>.
- [25] Zhenbo Peng and Haitao Liu. "Bottom-up Nanofabrication Using DNA Nanostructures". In: *Chemistry of Materials* 28.4 (2016), pp. 1012–1021. DOI: 10.1021/acs.chemmater.5b04218. eprint: <https://doi.org/10.1021/acs.chemmater.5b04218>. URL: <https://doi.org/10.1021/acs.chemmater.5b04218>.
- [26] A.J. Ptak, S.W. Johnston, Sarah Kurtz, D.J. Friedman, and W.K. Metzger. "A comparison of MBE- and MOCVD-grown GaInNAs". In: *Journal of Crystal Growth* 251.1 (2003). Proceedings of the Twelfth International Conference on Molecular Beam Epitaxy, pp. 392–398. ISSN: 0022-0248. DOI: [https://doi.org/10.1016/S0022-0248\(02\)02201-7](https://doi.org/10.1016/S0022-0248(02)02201-7). URL: <http://www.sciencedirect.com/science/article/pii/S0022024802022017>.

- [27] P.M. Petroff and S.P. DenBaars. “MBE and MOCVD growth and properties of self-assembling quantum dot arrays in III-V semiconductor structures”. In: *Superlattices and Microstructures* 15.1 (1994), p. 15. ISSN: 0749-6036. DOI: <https://doi.org/10.1006/spmi.1994.1004>. URL: <http://www.sciencedirect.com/science/article/pii/S0749603684710044>.
- [28] Tak-Sing Wong, Branden Brough, and Chih-Ming Ho. “Creation of functional micro/nano systems through top-down and bottom-up approaches”. eng. In: *Molecular & cellular biomechanics : MCB* 6.1 (Mar. 2009), pp. 1–55. ISSN: 1556-5297. URL: <https://pubmed.ncbi.nlm.nih.gov/19382535>.
- [29] Boon K. Teo and X. H. Sun. “From Top-Down to Bottom-Up to Hybrid Nanotechnologies: Road to Nanodevices”. In: *Journal of Cluster Science* 17.4 (Dec. 2006), pp. 529–540. ISSN: 1572-8862. DOI: 10.1007/s10876-006-0086-5. URL: <https://doi.org/10.1007/s10876-006-0086-5>.
- [30] P.C. McIntyre and A. Fontcuberta i Morral. “Semiconductor nanowires: to grow or not to grow?” In: *Materials Today Nano* 9 (2020), p. 100058. ISSN: 2588-8420. DOI: <https://doi.org/10.1016/j.mtnano.2019.100058>. URL: <http://www.sciencedirect.com/science/article/pii/S2588842019301270>.
- [31] Ann L. Greenaway et al. “Selective Area Epitaxy of GaAs Microstructures by Close-Spaced Vapor Transport for Solar Energy Conversion Applications”. In: *ACS Energy Letters* 1.2 (2016), pp. 402–408. DOI: 10.1021/acsenergylett.6b00217. eprint: <https://doi.org/10.1021/acsenergylett.6b00217>. URL: <https://doi.org/10.1021/acsenergylett.6b00217>.
- [32] Naiyin Wang et al. “Shape Engineering of InP Nanostructures by Selective Area Epitaxy”. In: *ACS Nano* 13.6 (2019). PMID: 31180645, pp. 7261–7269. DOI: 10.1021/acsnano.9b02985. eprint: <https://doi.org/10.1021/acsnano.9b02985>. URL: <https://doi.org/10.1021/acsnano.9b02985>.
- [33] L. Desplanque, A. Bucamp, D. Troadec, G. Patriarche, and X. Wallart. “Selective area molecular beam epitaxy of InSb nanostructures on mismatched substrates”. In: *Journal of Crystal Growth* 512 (2019), pp. 6–10. ISSN: 0022-0248. DOI: <https://doi.org/10.1016/j.jcrysgro.2019.02.012>. URL: <http://www.sciencedirect.com/science/article/pii/S002202481930082X>.
- [34] Chuang Zhang, Yongli Yan, Yong Sheng Zhao, and Jiannian Yao. “Synthesis and applications of organic nanorods, nanowires and nanotubes”. In: *Annu. Rep. Prog. Chem., Sect. C: Phys. Chem.* 109 (0 2013), pp. 211–239. DOI: 10.1039/C3PC90002A. URL: <http://dx.doi.org/10.1039/C3PC90002A>.
- [35] Yu Li, Xiao-Yu Yang, Yi Feng, Zhong-Yong Yuan, and Bao-Lian Su. “One-Dimensional Metal Oxide Nanotubes, Nanowires, Nanoribbons, and Nanorods: Synthesis, Characterizations, Properties and Applications”. In: *Critical Reviews in Solid State and Materials Sciences* 37.1 (2012), pp. 1–74. DOI: 10.1080/10408436.2011.606512. eprint:

- <https://doi.org/10.1080/10408436.2011.606512>. URL: <https://doi.org/10.1080/10408436.2011.606512>.
- [36] Andrea Tao et al. “Langmuir-Blodgett Silver Nanowire Monolayers for Molecular Sensing Using Surface-Enhanced Raman Spectroscopy”. In: *Nano Letters* 3.9 (2003), pp. 1229–1233. DOI: 10.1021/nl0344209. eprint: <https://doi.org/10.1021/nl0344209>. URL: <https://doi.org/10.1021/nl0344209>.
- [37] “Nanowire-Based Biosensors”. In: *Analytical Chemistry* 78.13 (2006). PMID: 16856252, pp. 4260–4269. DOI: 10.1021/ac069419j. eprint: <https://doi.org/10.1021/ac069419j>. URL: <https://doi.org/10.1021/ac069419j>.
- [38] Sakon Rahong, Takao Yasui, Noritada Kaji, and Yoshinobu Baba. “Recent developments in nanowires for bio-applications from molecular to cellular levels”. In: *Lab Chip* 16 (7 2016), pp. 1126–1138. DOI: 10.1039/C5LC01306B. URL: <http://dx.doi.org/10.1039/C5LC01306B>.
- [39] Nicklas Anttu. “Absorption of light in a single vertical nanowire and a nanowire array”. In: *Nanotechnology* 30.10 (2019), p. 104004. DOI: 10.1088/1361-6528/aafa5c. URL: <https://doi.org/10.1088/1361-6528/aafa5c>.
- [40] Rune Frederiksen, Gozde Tutuncuoglu, Federico Matteini, Karen L. Martinez, Anna Fontcuberta i Morral, and Esther Alarcon-Llado. “Visual Understanding of Light Absorption and Waveguiding in Standing Nanowires with 3D Fluorescence Confocal Microscopy”. In: *ACS Photonics* 4.9 (2017), pp. 2235–2241. DOI: 10.1021/acsp Photonics.7b00434. eprint: <https://doi.org/10.1021/acsp Photonics.7b00434>. URL: <https://doi.org/10.1021/acsp Photonics.7b00434>.
- [41] Peter Krogstrup et al. “Single-nanowire solar cells beyond the Shockley–Queisser limit”. In: *Nature Photonics* 7.4 (Apr. 2013), pp. 306–310. ISSN: 1749-4893. DOI: 10.1038/nphoton.2013.32. URL: <https://doi.org/10.1038/nphoton.2013.32>.
- [42] Erik C. Garnett, Mark L. Brongersma, Yi Cui, and Michael D. McGehee. “Nanowire Solar Cells”. In: *Annual Review of Materials Research* 41.1 (2011), pp. 269–295. DOI: 10.1146/annurev-matsci-062910-100434. eprint: <https://doi.org/10.1146/annurev-matsci-062910-100434>. URL: <https://doi.org/10.1146/annurev-matsci-062910-100434>.
- [43] Matt Law, Lori E. Greene, Justin C. Johnson, Richard Saykally, and Peidong Yang. “Nanowire dye-sensitized solar cells”. In: *Nature Materials* 4.6 (June 2005), pp. 455–459. ISSN: 1476-4660. DOI: 10.1038/nmat1387. URL: <https://doi.org/10.1038/nmat1387>.
- [44] Luchan Lin et al. “Contact engineering of single core/shell SiC/SiO₂ nanowire memory unit with high current tolerance using focused femtosecond laser irradiation”. In: *Nanoscale* 12 (9 2020), pp. 5618–5626. DOI: 10.1039/C9NR10690A. URL: <http://dx.doi.org/10.1039/C9NR10690A>.
- [45] Se-Ho Lee, Yeonwoong Jung, and Ritesh Agarwal. “Highly scalable non-volatile and ultra-low-power phase-change nanowire memory”. In: *Nature Nanotechnology* 2.10 (Oct. 2007), pp. 626–630. ISSN: 1748-3395. DOI: 10.1038/nnano.2007.291. URL: <https://doi.org/10.1038/nnano.2007.291>.

- [46] J. Appenzeller, J. Knoch, M. T. Bjork, H. Riel, H. Schmid, and W. Riess. "Toward Nanowire Electronics". In: *IEEE Transactions on Electron Devices* 55.11 (2008), pp. 2827–2845.
- [47] C. Thelander et al. "Nanowire-based one-dimensional electronics". In: *Materials Today* 9.10 (2006), pp. 28–35. ISSN: 1369-7021. DOI: [https://doi.org/10.1016/S1369-7021\(06\)71651-0](https://doi.org/10.1016/S1369-7021(06)71651-0). URL: <http://www.sciencedirect.com/science/article/pii/S1369702106716510>.
- [48] Mark S. Gudiksen, Lincoln J. Lauhon, Jianfang Wang, David C. Smith, and Charles M. Lieber. "Growth of nanowire superlattice structures for nanoscale photonics and electronics". In: *Nature* 415.6872 (Feb. 2002), pp. 617–620. ISSN: 1476-4687. DOI: 10.1038/415617a. URL: <https://doi.org/10.1038/415617a>.
- [49] Xiaocheng Jiang, Qihua Xiong, Sungwoo Nam, Fang Qian, Yat Li, and Charles M. Lieber. "InAs/InP Radial Nanowire Heterostructures as High Electron Mobility Devices". In: *Nano Letters* 7.10 (2007). PMID: 17867718, pp. 3214–3218. DOI: 10.1021/nl072024a. eprint: <https://doi.org/10.1021/nl072024a>. URL: <https://doi.org/10.1021/nl072024a>.
- [50] Oki Gunawan et al. "Measurement of Carrier Mobility in Silicon Nanowires". In: *Nano Letters* 8.6 (2008). PMID: 18444687, pp. 1566–1571. DOI: 10.1021/nl072646w. eprint: <https://doi.org/10.1021/nl072646w>. URL: <https://doi.org/10.1021/nl072646w>.
- [51] Önder Gül et al. "Towards high mobility InSb nanowire devices". In: *Nanotechnology* 26.21 (2015), p. 215202. DOI: 10.1088/0957-4484/26/21/215202. URL: <https://doi.org/10.1088%2F0957-4484%2F26%2F21%2F215202>.
- [52] Bernt Ketterer, Emanuele Uccelli, and Anna Fontcuberta i Morral. "Mobility and carrier density in p-type GaAs nanowires measured by transmission Raman spectroscopy". In: *Nanoscale* 4 (5 2012), pp. 1789–1793. DOI: 10.1039/C2NR11910B. URL: <http://dx.doi.org/10.1039/C2NR11910B>.
- [53] Chuancheng Jia, Zhaoyang Lin, Yu Huang, and Xiangfeng Duan. "Nanowire Electronics: From Nanoscale to Macroscale". In: *Chemical Reviews* 119.15 (2019). PMID: 31361471, pp. 9074–9135. DOI: 10.1021/acs.chemrev.9b00164. eprint: <https://doi.org/10.1021/acs.chemrev.9b00164>. URL: <https://doi.org/10.1021/acs.chemrev.9b00164>.
- [54] Jerry Wu, Yin-Lin Shen, Kitt Reinhardt, and Harold Szu. "A NANO enhancement to Moore's law". In: (May 2012), pp. 18–. DOI: 10.1117/12.921203.
- [55] H C Card and E H Rhoderick. "Studies of tunnel MOS diodes I. Interface effects in silicon Schottky diodes". In: *Journal of Physics D: Applied Physics* 4.10 (1971), pp. 1589–1601. DOI: 10.1088/0022-3727/4/10/319. URL: <https://doi.org/10.1088%2F0022-3727%2F4%2F10%2F319>.
- [56] G. Larrieu, Y. Guerfi, X.L. Han, and N. Clément. "Sub-15nm gate-all-around field effect transistors on vertical silicon nanowires". In: *Solid-State Electronics* 130 (2017), pp. 9–14. ISSN: 0038-1101. DOI: <https://doi.org/10.1016/j.sse.2016.12.008>. URL: <http://www.sciencedirect.com/science/article/pii/S0038110116303094>.

- [57] Yichao Wang et al. “Electrochemical Control of Photoluminescence in Two-Dimensional MoS₂ Nanoflakes”. In: *ACS Nano* 7.11 (2013). PMID: 24148149, pp. 10083–10093. DOI: 10.1021/nn4041987. eprint: <https://doi.org/10.1021/nn4041987>. URL: <https://doi.org/10.1021/nn4041987>.
- [58] Sujay B. Desai et al. “MoS₂ transistors with 1-nanometer gate lengths”. In: *Science* 354.6308 (2016), pp. 99–102. ISSN: 0036-8075. DOI: 10.1126/science.aah4698. eprint: <https://science.sciencemag.org/content/354/6308/99.full.pdf>. URL: <https://science.sciencemag.org/content/354/6308/99>.
- [59] Kyung Soo Yi, Krutarth Trivedi, Herman C. Floresca, Hyungsang Yuk, Walter Hu, and Moon J. Kim. “Room-Temperature Quantum Confinement Effects in Transport Properties of Ultrathin Si Nanowire Field-Effect Transistors”. In: *Nano Letters* 11.12 (2011). PMID: 22112200, pp. 5465–5470. DOI: 10.1021/nl203238e. eprint: <https://doi.org/10.1021/nl203238e>. URL: <https://doi.org/10.1021/nl203238e>.
- [60] Stevan Nadj-Perge, S Frolov, Erik Bakkers, and L Kouwenhoven. “Spin-orbit qubit in a semiconductor nanowire”. In: *Nature* 468 (Dec. 2010), pp. 1084–7. DOI: 10.1038/nature09682.
- [61] Carina Fasth, Andreas Fuhrer, Mikael T. Björk, and Lars Samuelson. “Tunable Double Quantum Dots in InAs Nanowires Defined by Local Gate Electrodes”. In: *Nano Letters* 5.7 (2005). PMID: 16178262, pp. 1487–1490. DOI: 10.1021/nl050850i. eprint: <https://doi.org/10.1021/nl050850i>. URL: <https://doi.org/10.1021/nl050850i>.
- [62] V. Mourik, K. Zuo, S. M. Frolov, S. R. Plissard, E. P. A. M. Bakkers, and L. P. Kouwenhoven. “Signatures of Majorana Fermions in Hybrid Superconductor-Semiconductor Nanowire Devices”. In: *Science* 336.6084 (2012), pp. 1003–1007. ISSN: 0036-8075. DOI: 10.1126/science.1222360. eprint: <https://science.sciencemag.org/content/336/6084/1003.full.pdf>. URL: <https://science.sciencemag.org/content/336/6084/1003>.
- [63] Hailong Wang, Luis A. Zepeda-Ruiz, George H. Gilmer, and Moneesh Upmanyu. “Atomistics of vapor-liquid-solid nanowire growth”. In: *Nature Communications* 4 (June 2013). arXiv: 1305.0038. ISSN: 2041-1723. DOI: 10.1038/ncomms2956. URL: <http://arxiv.org/abs/1305.0038>.
- [64] Kimberly A. Dick. “A review of nanowire growth promoted by alloys and non-alloying elements with emphasis on Au-assisted III–V nanowires”. In: *Progress in Crystal Growth and Characterization of Materials* 54.3–4 (Sept. 2008), pp. 138–173. ISSN: 0960-8974. DOI: 10.1016/j.pcrysgrow.2008.09.001. URL: <http://www.sciencedirect.com/science/article/pii/S0960897408000181>.
- [65] E. I. Givargizov. “Fundamental aspects of VLS growth”. In: *Journal of Crystal Growth* 31 (Dec. 1975), pp. 20–30. ISSN: 0022-0248. DOI: 10.1016/0022-0248(75)90105-0. URL: <http://www.sciencedirect.com/science/article/pii/0022024875901050>.

- [66] Frank Glas, Mohammed Reda Ramdani, Gilles Patriarche, and Jean-Christophe Harmand. “Predictive modeling of self-catalyzed III-V nanowire growth”. In: *Physical Review B* 88.19 (Nov. 2013), p. 195304. DOI: 10.1103/PhysRevB.88.195304. URL: <https://link.aps.org/doi/10.1103/PhysRevB.88.195304> (visited on 06/02/2017).
- [67] Frank Glas, Jean-Christophe Harmand, and Gilles Patriarche. “Why Does Wurtzite Form in Nanowires of III-V Zinc Blende Semiconductors?” In: *Physical Review Letters* 99.14 (Oct. 2007), p. 146101. DOI: 10.1103/PhysRevLett.99.146101. URL: <https://link.aps.org/doi/10.1103/PhysRevLett.99.146101>.
- [68] V. G. Dubrovskii, N. V. Sibirev, J. C. Harmand, and F. Glas. “Growth kinetics and crystal structure of semiconductor nanowires”. In: *Physical Review B* 78.23 (Dec. 2008), p. 235301. DOI: 10.1103/PhysRevB.78.235301. URL: <https://link.aps.org/doi/10.1103/PhysRevB.78.235301>.
- [69] K. W. Schwarz and J. Tersoff. “Elementary Processes in Nanowire Growth”. In: *Nano Letters* 11.2 (Feb. 2011), pp. 316–320. ISSN: 1530-6984. DOI: 10.1021/nl1027815. URL: <https://doi.org/10.1021/nl1027815> (visited on 03/28/2018).
- [70] Yi-Chia Chou, Federico Panciera, Mark C. Reuter, Eric A. Stach, and Frances M. Ross. “Nanowire growth kinetics in aberration corrected environmental transmission electron microscopy”. en. In: *Chemical Communications* 52.33 (2016), pp. 5686–5689. ISSN: 1359-7345, 1364-548X. DOI: 10.1039/C6CC00303F. URL: <http://xlink.rsc.org/?DOI=C6CC00303F> (visited on 01/22/2019).
- [71] Volker Schmidt, Joerg V. Wittemann, Stephan Senz, and Ulrich Gösele. “Silicon Nanowires: A Review on Aspects of their Growth and their Electrical Properties”. en. In: *Advanced Materials* 21.25-26 (2009), pp. 2681–2702. ISSN: 1521-4095. DOI: 10.1002/adma.200803754. URL: <https://onlinelibrary.wiley.com/doi/abs/10.1002/adma.200803754> (visited on 01/22/2019).
- [72] Volker Schmidt, Stephan Senz, and Ulrich Gösele. “Diameter-Dependent Growth Direction of Epitaxial Silicon Nanowires”. In: *Nano Letters* 5.5 (2005). PMID: 15884897, pp. 931–935. DOI: 10.1021/nl050462g. eprint: <https://doi.org/10.1021/nl050462g>. URL: <https://doi.org/10.1021/nl050462g>.
- [73] B. J. O’Dowd et al. “Effect of catalyst diameter on vapour-liquid-solid growth of GaAs nanowires”. In: *Journal of Applied Physics* 116.6 (Aug. 2014), p. 063509. ISSN: 0021-8979. DOI: 10.1063/1.4893021. URL: <https://aip.scitation.org/doi/10.1063/1.4893021> (visited on 02/22/2019).
- [74] Valentina Zannier et al. “Catalyst Composition Tuning: The Key for the Growth of Straight Axial Nanowire Heterostructures with Group III Interchange”. In: *Nano Letters* 16.11 (Nov. 2016), pp. 7183–7190. ISSN: 1530-6984. DOI: 10.1021/acs.nanolett.6b03524. URL: <http://dx.doi.org/10.1021/acs.nanolett.6b03524>.

- [75] Jia Wang, Sébastien R. Plissard, Marcel A. Verheijen, Lou-Fé Feiner, Alessandro Cavalli, and Erik P. A. M. Bakkers. “Reversible Switching of InP Nanowire Growth Direction by Catalyst Engineering”. In: *Nano Letters* 13.8 (Aug. 2013), pp. 3802–3806. ISSN: 1530-6984. DOI: 10.1021/nl401767b. URL: <http://dx.doi.org/10.1021/nl401767b>.
- [76] V G Dubrovskii, Zh V Sokolova, M V Rylkova, and A A Zhiglinsky. “COMPOSITION AND CONTACT ANGLE OF Au-III-V DROPLETS ON TOP OF Au-CATALYZED III-V NANOWIRES”. en. In: (), p. 7.
- [77] Carina B. Maliakkal et al. “In situ analysis of catalyst composition during gold catalyzed GaAs nanowire growth”. In: *Nature Communications* 10.1 (Oct. 2019), p. 4577. ISSN: 2041-1723. DOI: 10.1038/s41467-019-12437-6. URL: <https://doi.org/10.1038/s41467-019-12437-6>.
- [78] Michał Horodecki and Jonathan Oppenheim. “Fundamental limitations for quantum and nanoscale thermodynamics”. In: *Nature Communications* 4.1 (June 2013), p. 2059. ISSN: 2041-1723. DOI: 10.1038/ncomms3059. URL: <https://doi.org/10.1038/ncomms3059>.
- [79] Jihan Zhou et al. “Observing crystal nucleation in four dimensions using atomic electron tomography”. In: *Nature* 570.7762 (June 2019), pp. 500–503. ISSN: 1476-4687. DOI: 10.1038/s41586-019-1317-x. URL: <https://doi.org/10.1038/s41586-019-1317-x>.
- [80] Lea Ghisalberti et al. “Questioning liquid droplet stability on nanowire tips: from theory to experiment.” In: *Nanotechnology* (2019). DOI: 10.1088/1361-6528/ab139c.
- [81] Zhi Zhang, Kun Zheng, Zhen-Yu Lu, Ping-Ping Chen, Wei Lu, and Jin Zou. “Catalyst Orientation-Induced Growth of Defect-Free Zinc-Blende Structured $\langle 001 \rangle$ InAs Nanowires”. In: *Nano Letters* 15.2 (Feb. 2015), pp. 876–882. ISSN: 1530-6984. DOI: 10.1021/nl503556a. URL: <http://dx.doi.org/10.1021/nl503556a> (visited on 05/30/2017).
- [82] Chin-Yu Yeh, Z. W. Lu, S. Froyen, and Alex Zunger. “Zinc-blende\char21{}wurtzite polytypism in semiconductors”. In: *Physical Review B* 46.16 (Oct. 1992), pp. 10086–10097. DOI: 10.1103/PhysRevB.46.10086. URL: <https://link.aps.org/doi/10.1103/PhysRevB.46.10086>.
- [83] H. Aruni Fonseka, Philippe Caroff, Jennifer Wong-Leung, Amira S. Ameruddin, Hark Hoe Tan, and Chennupati Jagadish. “Nanowires Grown on InP (100): Growth Directions, Facets, Crystal Structures, and Relative Yield Control”. In: *ACS Nano* 8.7 (July 2014), pp. 6945–6954. ISSN: 1936-0851. DOI: 10.1021/nn5017428. URL: <http://dx.doi.org/10.1021/nn5017428>.
- [84] Jia Wang, Sébastien R. Plissard, Marcel A. Verheijen, Lou-Fé Feiner, Alessandro Cavalli, and Erik P. A. M. Bakkers. “Reversible Switching of InP Nanowire Growth Direction by Catalyst Engineering”. In: *Nano Letters* 13.8 (Aug. 2013), pp. 3802–3806. ISSN: 1530-6984. DOI: 10.1021/nl401767b. URL: <http://dx.doi.org/10.1021/nl401767b>.

- [85] Heidi Potts, Nicholas P. Morgan, Gözde Tütüncüoğlu, Martin Friedl, and Anna Fontcuberta i Morral. “Tuning growth direction of catalyst-free InAs(Sb) nanowires with indium droplets”. en. In: *Nanotechnology* 28.5 (2017), p. 054001. ISSN: 0957-4484. DOI: 10.1088/1361-6528/28/5/054001. URL: <http://stacks.iop.org/0957-4484/28/i=5/a=054001>.
- [86] Soo-Ghang Ihn et al. “Morphology- and Orientation-Controlled Gallium Arsenide Nanowires on Silicon Substrates”. In: *Nano Letters* 7.1 (Jan. 2007), pp. 39–44. ISSN: 1530-6984. DOI: 10.1021/nl0618795. URL: <http://dx.doi.org/10.1021/nl0618795> (visited on 01/03/2018).
- [87] Zhiyuan Sun, David N. Seidman, and Lincoln J. Lauhon. “Nanowire Kinking Modulates Doping Profiles by Reshaping the Liquid–Solid Growth Interface”. In: *Nano Letters* 17.7 (July 2017), pp. 4518–4525. ISSN: 1530-6984. DOI: 10.1021/acs.nanolett.7b02071. URL: <https://doi.org/10.1021/acs.nanolett.7b02071> (visited on 01/22/2019).
- [88] Federico Matteini, Gözde Tütüncüoğlu, Heidi Potts, Fauzia Jabeen, and Anna Fontcuberta i Morral. “Wetting of Ga on SiO_x and Its Impact on GaAs Nanowire Growth”. In: *Crystal Growth & Design* 15.7 (July 2015), pp. 3105–3109. ISSN: 1528-7483. DOI: 10.1021/acs.cgd.5b00374. URL: <http://dx.doi.org/10.1021/acs.cgd.5b00374>.
- [89] Federico Matteini et al. “Impact of the Ga Droplet Wetting, Morphology, and Pinholes on the Orientation of GaAs Nanowires”. In: *Crystal Growth & Design* 16.10 (Oct. 2016), pp. 5781–5786. ISSN: 1528-7483. DOI: 10.1021/acs.cgd.6b00858. URL: <http://dx.doi.org/10.1021/acs.cgd.6b00858>.
- [90] Xiaoming Yuan, Philippe Caroff, Jennifer Wong-Leung, Lan Fu, Hark Hoe Tan, and Chennupati Jagadish. “Tunable Polarity in a III–V Nanowire by Droplet Wetting and Surface Energy Engineering”. In: *Advanced Materials* 27.40 (2015), pp. 6096–6103. ISSN: 1521-4095. DOI: 10.1002/adma.201503540. URL: <https://onlinelibrary.wiley.com/doi/abs/10.1002/adma.201503540> (visited on 02/22/2019).
- [91] V. A. Nebol’sin and A. A. Shchetinin. “Role of Surface Energy in the Vapor–Liquid–Solid Growth of Silicon”. en. In: *Inorganic Materials* 39.9 (Sept. 2003), pp. 899–903. ISSN: 0020-1685, 1608-3172. DOI: 10.1023/A:1025588601262. URL: <https://link.springer.com/article/10.1023/A:1025588601262> (visited on 06/12/2017).
- [92] Timofey Frolov, W. Craig Carter, and Mark Asta. “Capillary Instability in Nanowire Geometries”. In: *Nano Letters* 14.6 (2014). _eprint: <https://doi.org/10.1021/nl501214p>, pp. 3577–3581. DOI: 10.1021/nl501214p. URL: <https://doi.org/10.1021/nl501214p>.
- [93] Su Ji Park, Byung Mook Weon, Ji San Lee, Junho Lee, Jinkyung Kim, and Jung Ho Je. “Visualization of asymmetric wetting ridges on soft solids with X-ray microscopy”. In: *Nature Communications* 5 (July 2014). ISSN: 2041-1723. DOI: 10.1038/ncomms5369. URL: <https://www.ncbi.nlm.nih.gov/pmc/articles/PMC4104447/> (visited on 04/11/2018).

- [94] Wayne D. Kaplan, Dominique Chatain, Paul Wynblatt, and W. Craig Carter. "A review of wetting versus adsorption, complexions, and related phenomena: the rosetta stone of wetting". In: *Journal of Materials Science* 48.17 (Sept. 2013), pp. 5681–5717. ISSN: 1573-4803. DOI: 10.1007/s10853-013-7462-y. URL: <https://doi.org/10.1007/s10853-013-7462-y>.
- [95] Kenneth A. Brakke. "The Surface Evolver". en. In: *Experimental Mathematics* 1.2 (Jan. 1992), pp. 141–165. ISSN: 1058-6458, 1944-950X. DOI: 10.1080/10586458.1992.10504253. URL: <http://www.tandfonline.com/doi/abs/10.1080/10586458.1992.10504253> (visited on 07/04/2018).
- [96] Kenneth A. Brakke. "The Surface Evolver and the Stability of Liquid Surfaces". In: *Philosophical Transactions: Mathematical, Physical and Engineering Sciences* 354.1715 (1996), pp. 2143–2157. ISSN: 1364503X. URL: <http://www.jstor.org/stable/54583>.
- [97] Steven H. Collicott and Mark M. Weislogel. "Computing Existence and Stability of Capillary Surfaces Using Surface Evolver". In: *AIAA Journal* 42.2 (2004), pp. 289–295. ISSN: 0001-1452. DOI: 10.2514/1.9093. URL: <https://doi.org/10.2514/1.9093>.
- [98] Hans Mittelmann. "Symmetric capillary surface in a cube". English (US). In: *Mathematics and Computers in Simulation* 35.2 (Apr. 1993), pp. 139–152. ISSN: 0378-4754. DOI: 10.1016/0378-4754(93)90009-J.
- [99] *Numerical Analysis of the Shapes and Energies of Droplets on Micropatterned Substrates*. URL: <http://pubs.acs.org/doi/pdf/10.1021/la053146q> (visited on 11/29/2017).
- [100] Matthew L. Blow and Julia M. Yeomans. "SURFACE EVOLVER SIMULATIONS OF DROPS ON MICROPOSTS". en. In: *International Journal of Modern Physics C* 23.08 (Aug. 2012), p. 1240013. ISSN: 0129-1831, 1793-6586. DOI: 10.1142/S012918311240013X. URL: <http://www.worldscientific.com/doi/abs/10.1142/S012918311240013X> (visited on 07/04/2018).
- [101] Dominique Chatain, Dan Lewis, Jean-Pierre Baland, and W. Craig Carter. "Numerical Analysis of the Shapes and Energies of Droplets on Micropatterned Substrates". en. In: *Langmuir* 22.9 (Apr. 2006), pp. 4237–4243. ISSN: 0743-7463, 1520-5827. DOI: 10.1021/la053146q. URL: <http://pubs.acs.org/doi/abs/10.1021/la053146q> (visited on 04/11/2018).
- [102] Francesca Stephenson and Dr. Tim Atherton. "Modeling of Multicomponent Lipid Membranes Using Energy Minimization Techniques". In: *Senior Project Committee, Department of Physics, Case Western Reserve University* (2011). URL: http://www.phys.cwru.edu/undergrad/Senior%20Projects/papers/papers2011/Stephenson_Atherton_2011%20S.pdf.
- [103] Douglas A. Reinelt and Andrew M. Kraynik. "Simple shearing flow of dry soap foams with tetrahedrally close-packed structure". In: *Journal of Rheology* 44.3 (2000). _eprint: <https://doi.org/10.1122/1.551096>, pp. 453–471. DOI: 10.1122/1.551096. URL: <https://doi.org/10.1122/1.551096>.

- [104] Jia Wang et al. "Position-controlled [100] InP nanowire arrays". In: *Applied Physics Letters* 100.5 (Jan. 2012), p. 053107. ISSN: 0003-6951. DOI: 10.1063/1.3679136. URL: <http://aip.scitation.org/doi/abs/10.1063/1.3679136> (visited on 06/02/2017).
- [105] Aurélie Pierret et al. "Generic nano-imprint process for fabrication of nanowire arrays". en. In: *Nanotechnology* 21.6 (2010), p. 065305. ISSN: 0957-4484. DOI: 10.1088/0957-4484/21/6/065305. URL: <http://stacks.iop.org/0957-4484/21/i=6/a=065305> (visited on 01/03/2018).
- [106] Eleonora Russo-Averchi et al. "High Yield of GaAs Nanowire Arrays on Si Mediated by the Pinning and Contact Angle of Ga". In: *Nano Letters* 15.5 (May 2015), pp. 2869–2874. ISSN: 1530-6984. DOI: 10.1021/nl504437v. URL: <https://doi.org/10.1021/nl504437v> (visited on 04/24/2019).
- [107] Qian Gao et al. "Simultaneous Selective-Area and Vapor–Liquid–Solid Growth of InP Nanowire Arrays". In: *Nano Letters* 16.7 (2016). PMID: 27253040, pp. 4361–4367. DOI: 10.1021/acs.nanolett.6b01461. eprint: <https://doi.org/10.1021/acs.nanolett.6b01461>. URL: <https://doi.org/10.1021/acs.nanolett.6b01461>.
- [108] V. G. Dubrovskii, N. V. Sibirev, J. C. Harmand, and F. Glas. "Growth kinetics and crystal structure of semiconductor nanowires". In: 78.23, 235301 (Dec. 2008), p. 235301. DOI: 10.1103/PhysRevB.78.235301.
- [109] Daniel Jacobsson et al. "Interface dynamics and crystal phase switching in GaAs nanowires". eng. In: *Nature* 531.7594 (Mar. 2016), pp. 317–322. ISSN: 1476-4687. DOI: 10.1038/nature17148. URL: <https://pubmed.ncbi.nlm.nih.gov/26983538>.
- [110] J. Kammhuber et al. "Conductance through a helical state in an Indium antimonide nanowire". En. In: *Nature Communications* 8.1 (Sept. 2017), p. 478. ISSN: 2041-1723. DOI: 10.1038/s41467-017-00315-y. URL: <https://www.nature.com/articles/s41467-017-00315-y> (visited on 09/08/2017).
- [111] Jason Alicea, Yuval Oreg, Gil Refael, Felix von Oppen, and Matthew P. A. Fisher. "Non-Abelian statistics and topological quantum information processing in 1D wire networks". In: *Nature Physics* 7.5 (May 2011). arXiv: 1006.4395, pp. 412–417. ISSN: 1745-2473, 1745-2481. DOI: 10.1038/nphys1915. URL: <http://arxiv.org/abs/1006.4395> (visited on 12/20/2017).
- [112] J. Vukajlovic-Plestina et al. "Fundamental aspects to localize self-catalyzed III-V nanowires on silicon". en. In: *Nature Communications* 10.1 (Dec. 2019). ISSN: 2041-1723. DOI: 10.1038/s41467-019-08807-9. URL: <http://www.nature.com/articles/s41467-019-08807-9> (visited on 08/05/2019).
- [113] C. Jürgensen et al. "Growth of nanowire arrays from micron-feature templates". en. In: *Nanotechnology* 30.28 (Apr. 2019), p. 285302. ISSN: 0957-4484. DOI: 10.1088/1361-6528/ab1699. URL: <https://doi.org/10.1088%2F1361-6528%2Fab1699> (visited on 08/05/2019).

- [114] Lucas Güniat et al. “III–V Integration on Si(100): Vertical Nanospades”. In: *ACS Nano* 13.5 (2019). PMID: 31038924, pp. 5833–5840. DOI: 10.1021/acsnano.9b01546. eprint: <https://doi.org/10.1021/acsnano.9b01546>. URL: <https://doi.org/10.1021/acsnano.9b01546>.
- [115] Ali Vazinishayan, Shuming Yang, Anchalee Duongthipthewa, and Yiming Wang. “Effects of cross-section on mechanical properties of Au nanowire”. In: *AIP Advances* 6.2 (2016), p. 025006. DOI: 10.1063/1.4941831. eprint: <https://doi.org/10.1063/1.4941831>. URL: <https://doi.org/10.1063/1.4941831>.
- [116] Zi-An Li et al. “Planar-defect characteristics and cross-sections of 001, 111, and 112 InAs nanowires”. In: *Journal of Applied Physics* 109.11 (June 2011), p. 114320. ISSN: 0021-8979. DOI: 10.1063/1.3592186. URL: <http://aip.scitation.org/doi/abs/10.1063/1.3592186> (visited on 06/02/2017).
- [117] Jean-Christophe Harmand et al. “Atomic Step Flow on a Nanofacet”. In: *Phys. Rev. Lett.* 121 (16 2018), p. 166101. DOI: 10.1103/PhysRevLett.121.166101. URL: <https://link.aps.org/doi/10.1103/PhysRevLett.121.166101>.

Lea Ghisalberti

Rue de la Blancherie 9,
1022, Chavannes-Renens,
Switzerland
+41 77 966 09 43
lea.ghisalbert@epfl.ch

589 Putnam Avenue,
02139, Cambridge,
MA, USA
+1 617 341 9262
leaghisa@mit.edu



STRENGTHS

- Very adaptable researcher in the field of materials science and nanotechnology.
- Fast and efficient in learning and expert in data management and data analysis.
- Skilled in giving presentations on technical topics and in the accomplishment of research projects.

EDUCATION

- Present **PhD in Materials Science and Engineering**, Ecole Polytechnique Federale de Lausanne
Thesis Title: "Self-assisted growth of III-As nanowires in the (100) direction" Thesis supervisors: prof. Anna Fontcuberta i Morral and prof. Craig W. Carter
- 11.2016 **Master in Materials Science and Engineering**, University of Milano-Bicocca,
Dissertation/thesis title: "Morphology of vertical GaAs membranes epitaxially deposited on patterned substrates". Thesis supervisor: prof. Miglio Leonida
Final degree mark: 110/110 cum laude
- 10.2014 **Bachelor in Materials Science and Engineering**, University of Milano-Bicocca
Dissertation/thesis title: "Colloidal organic nanocrystals for fluorescent imaging". Thesis supervisor: prof. Luca Beverina
Final degree mark: 110/110
- 08.2011 **Secondary School Diploma in Languages**, Civica Manzoni High-School, Milano.
School-leaving examination mark: 80/100

TRAININGS AND CONFERENCES

- **Wolfram Technology Conference**, Champaign, Illinois (1 week), October 2018
- **Hermes Summer School**, Imperial College London. (1 week), July 2018
- **Nanotechnology meets Quantum Information** – NanoQI, Donostia International Physics Center, Donostia-San Sebastian, Spain (1 week), July 2017
- **NCCR-QSIT Winter School**, National Center of Competence in Research 'Quantum Science and Technology', Waldhotel National, Arosa, Switzerland (1 week), January 2017

EMPLOYMENT HISTORY

- Present **PhD in Materials Science and Engineering**, Ecole Polytechnique Federale de Lausanne
Supervisors: prof. Anna Fontcuberta i Morral and prof. Craig W. Carter
(Expected February 2021)

04.2016 **Internship in the Laboratory of Semiconductor Materials (LMSC) at EPFL**, Switzerland.
Optimization of III-V nanostructures prepared by MBE growth technique. Intense work in the Clean Room facilities and trained in many materials characterization techniques. (7 months)

SUPERVISION OF STUDENTS

05.2019 **Supervisor of visiting master student**
Master student Shin Hyeonjeong, enrolled in Physics M2 Engineering and Innovation Technologies at Kyung-Hee University (Seoul) and École Polytechnique (France).
Project title: "Self-Catalyzed growth of III-As Nanowires on Si (100) substrates"

TEACHING ACTIVITIES

Teaching Assistant in:

- Master Course "Properties of semiconductors and related nanostructures"
Technical support in the use of Mathematica and Nextnano. (2017, 2018, 2019)
- Doctoral Course "Methods of Modelling and Simulation of Materials Science"
Technical support in the use of Mathematica. (2018)
- Master Course "Modelling problem solving, computing and visualisation II"
Technical support in the use of Mathematica. (2017, 2018)

HONOURS & AWARDS

- DocMobility Fellowship Award for performing 9 months research at Massachusetts Institute of Technology (MIT), Boston, 2020
- Poster Quality Award for "Vapor-Liquid-Solid growth: Wetting angle and nanowire geometry and their relation to nanowire growth morphologies" at Nanowire Week 2019, Pisa
- Poster Quality Award for "Engineering the Wetting Behaviour of Metallic Nanodroplets and Correlation with Crystal Growth Orientation" at Materials Research Society (MRS), Fall Meeting & Exhibit 2018, Boston
- Poster Quality Award for "Understanding the wetting behavior of nanodroplets catalyzing the growth of III-V nanowires" - Nanowire Week 2018, Hamilton
- Accepted Talk in Symposium NM03 Progress in Developing and Applications of Functional One-Dimensional Nanostructures: "The Role of Wetting and Contact Angle in the Growth of III-As Nanowires" at Materials Research Society (MRS) Fall Meeting & Exhibit Fall Meeting & Exhibit 2017, Boston
- Accepted Talk in the Session on the characterization of epistuctures: "Morphological Analysis of GaAs Nanoscale Membranes Grown by Selective Area Epitaxy" at the 19th European Workshop on Molecular Beam Epitaxy 2017, St Petersburg
- Award "Miriam Ferrari" Bicocca University, for obtaining the Master Degree in Materials Science with the best timing and evaluation for the academic year 2016.
- INSPIRE Potentials - QSIT Master Internship Award. Awards for excellent female students who will conduct their Master thesis in a laboratory belonging to the NCCR QSIT network. 2016
- Programme Exchange Bicocca University: Mobilità Internazionale Extra-UE. Scholarship for performing the master project outside Europe. 2016

LANGUAGES

Italian (Native), English (Fluent), French (Intermediate), Spanish (Basic), German (Basic)

TECHNICAL SKILLS

Computer & IT:

Mathematica, Surface Evolver, Blender, Inkscape, LaTeX, SEA, ScanAsist, AxioVision, ImageJ, MS office (working knowledge)

LabView, Matlab, Python, Origin, Nextnano, Comsol, Adobe Illustrator (basic knowledge)